Design of Surgical Robotic Systems for Skull Base Interventions

By

Trevor L. Bruns

Dissertation

Submitted to the Faculty of the

Graduate School of Vanderbilt University

in partial fulfillment of the requirements

for the degree of

DOCTOR OF PHILOSOPHY

in

Mechanical Engineering

May 8, 2020

Nashville, Tennessee

Approved:

Robert J. Webster III, Ph.D.

Robert F. Labadie, M.D., Ph.D.

Thomas J. Withrow, Ph.D.

Eric J. Barth, Ph.D.

J. Michael Fitzpatrick, Ph.D.

To Lauren and Aubrey

ACKNOWLEDGMENTS

I must first thank my advisor, Bob Webster, for the initial encouragement to pursue graduate school. Without that impetus, I almost certainly would have never had the confidence to begin this journey. His constant support, trust, and patience has given me the freedom and opportunity to pursue the things that most interested me.

I would also like to thank my dissertation committee: Bob Webster, Rob Labadie, Tom Withrow, Eric Barth, and Mike Fitzpatrick. Rob has been invaluable resource throughout my Ph.D. and is always a pleasure to be around. Despite being a practicing surgeon, talented researcher, and father of four, he is perpetually calm, generous, and optimistic. Tom is always willing to take time out of his day to offer advice, encouragement, and friendly conversation. Eric is one of the best instructors I have ever had; his passion and deep knowledge of the subject matter is conveyed in a way that is clear, concise, and engaging. I have seen Mike's careful and methodical approach carry over into my own work and have always appreciated our deep (and sometimes extraneous) conversations. Thank you all for the many ways have enriched my graduate career.

The work presented in this dissertation was only possible through the combined efforts of my fellow lab members, collaborators, and clinicians. For the transnasal system presented in Chapter 2, I must thank Ray Lathrop, Hunter Gilbert, Phil Swaney, Jessica Burgner-Kahrs, Rich Hendrick, Art Mahoney, Andria Remirez, Max Emerson, Dr. Kyle Weaver, and Dr. Paul Russel. The magnetic steering system in Chapter 3 is the result of a collaboration with Jake Abbott's Telerobotics Lab at the University of Utah. I would like to thank Lou Kratchman, Katy Riojas, Dominick Ropella, James Clark, Andrew Petruska, Lisandro Leon, Matt Cavilla, and Cameron Hendricks. For the impedance sensing work in Chapter 4, I would like to thank Bob Webster for his support and Rob Labadie, Bob Dwyer, and Jack Noble for sharing their input and knowledge.

Finally, I owe an eternal debt of gratitude for my family. I thank my parents for all of

their love and support throughout my life. My wife Lauren has been my constant source of strength and inspiration and our daughter Aubrey has shown me just how deeply we are capable of loving one another. They have kept me grounded and given me perspective. It is to them that I dedicate this work.

TABLE OF CONTENTS

LIST OF TABLES

LIST OF FIGURES

Chapter 1

Introduction

1.1 Flexible Medical Devices: Robots and Implants

Flexible medical devices offer many advantages over their rigid counterparts. In the surgical realm, where applying too much force in the wrong place can have catastrophic consequences, having some amount of intrinsic compliance can be very beneficial. Many procedures requires navigating complex paths around obstacles in order to reach the targeted site. Why then does the most common surgical robot, the da Vinci Surgical System (Intuitive Surgical Inc., Sunnyvale, CA), use rigid tools and joints?

Figure 1.1: The da Vinci Xi surgical robot is operated remotely by a surgeon sitting at a console.

Traditional robots consist of discrete, rigid links connected by articulated joints. This basic structure has been well-studied for decades. Rigid-link robots can be accurately mod-

eled and precisely controlled—critical attributes when a patient's life is on the line. It makes sense then that the introduction of robots into the operating room would begin with this category. In fact, it was a common industrial robot (the PUMA 200) that became the first, when it was used to perform a neurosurgical biopsy in 1985 [1].

However, adapting designs originally intended for industrial assembly line tasks has some limitations. They generally require a large footprint that can be difficult to accommodate in a space-constrained operating room (OR). Their instruments are typically also rigid and straight with an articulated tip that is not usually conducive to miniaturization. As minimally invasive surgery (MIS) has steadily replaced traditional techniques [2], the need for a different class of surgical robots has become apparent.

Fortunately, while conventional rigid-link designs were building the case for the many advantages of robots in the OR, research in the field of continuum robots was making great strides. Their name is derived from the fact that, rather than a few rigid and separately articulated degrees of freedom (DOF), they have an infinite-DOF elastic structure. Many of the early designs were bioinspired, such as Hirose's snake-inspired robots first introduced in the 1970s [3]. It did not take long for medical uses of continuum robots to become apparent. Burgner-Kahrs et al. [4] provide a detailed survey of the broad range of continuum robots developed for a wide variety of surgical applications. They are often used when access to the desired area requires taking an indirect path near vital anatomy.

Sometimes the continuum device is required to remain at the target site and deliver therapy for an extended period of time. Although not usually framed at such, many surgical implants meet the definition of a continuum structure. A common example is nerve stimulators. These devices consist of one or more electrode contacts embedded in silicone. Their soft flexibility is an important characteristic since they must lie next to, or in contact with, the nerve they stimulate. Additionally, access to these nerves typically requires navigating through sensitive anatomy. For example, spinal cord stimulators are threaded into the epidural space, deep brain stimulators are placed directly into the brain, and cochlear

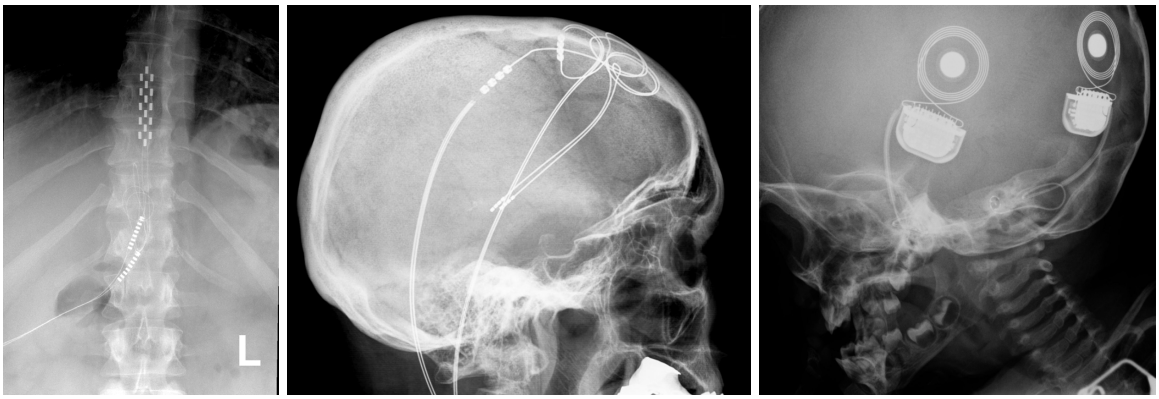

(a) (b) (c)

Figure 1.2: Implantable electrodes designed to send electrical impulses to nerves must often traverse through delicate and vital anatomy to reach their targets. Examples include: (a) spinal cord stimulation (b) deep brain stimulation and (c) cochlear implants.

implants are inserted into the fragile scala tympani (see Fig. 1.2). While clearly necessary, the elasticity of these implants also makes them challenging to manipulate. Surgeons are generally limited to grasping the back end in order to advance, risking buckling. Some procedures (e.g. deep brain stimulation) use a stiffening stylet to prevent this, negating the potential benefits of a compliant device. Ideally, surgeons would be able to have the best of both worlds: something that is both flexible and easily controlled.

This dissertation aims to illustrate this goal is achievable . In particular, two robotic systems for controlling elastic devices are presented for surgical interventions in the skull base. The first demonstrates how continuum robots can enable new, less invasive surgical techniques. The second introduces a system which enhances the maneuverability of cochlear implants to reduce trauma and improve patient outcomes.

1.2 Concentric Tube Robots

1.2.1 Overview

Concentric tube robots are a subclass of continuum robots [5]. They are composed of a series of tubes nested concentrically inside each other. Each precurved flexible tube (typi-

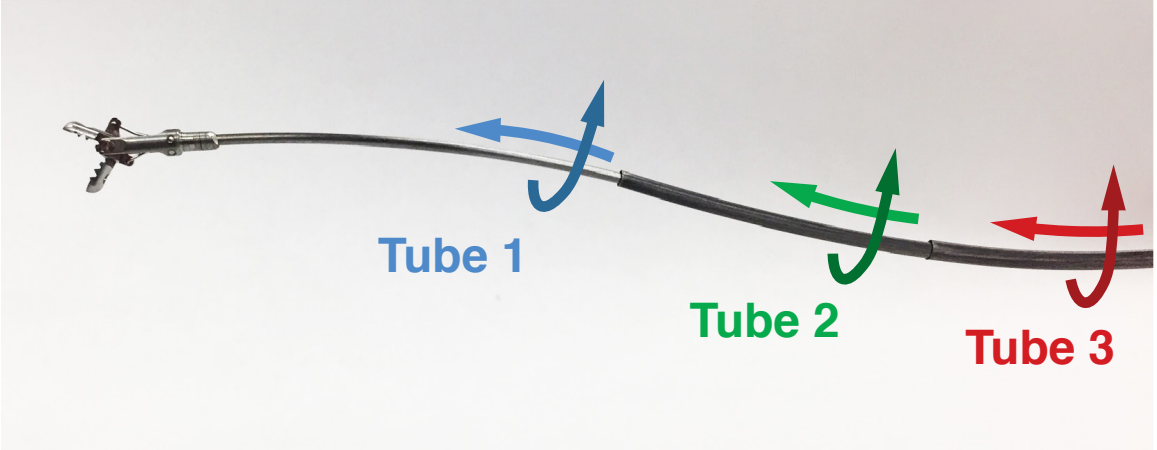

Figure 1.3: Example of a three-tube concentric tube robot. Tentacle-like motion results from the translation and rotation of each tube relative to the others.

cally made of superelastic Nitinol) is actuated by grasping the base and translating/rotating it with respect to the others (see Fig. 1.3). The elastic interactions between the tubes causes them to bend and twist through space in a motion similar to a snake or tentacle. The simple mechanical structure of concentric tube robots enables them to be scaled down to some of the smallest diameters of any continuum robot [4].

It is this combination of flexibility and scalability (see Fig. 1.4) that makes them particularly well-suited for medical applications. The enthusiasm for the wide array of possibilities is perhaps best evidenced by the remarkably rapid progress that has occurred since concentric tube robots were first introduced in the mid-2000s [6, 7, 8]. In the short time since, effective mathematical models have been developed [9, 10] enabling precise control in numerous regions of the body, including the brain [11, 12, 13], liver [14], prostate [15], lungs [16], and heart [17] (see [5] for a more extensive list).

1.2.2 Design for the Operating Room

While concentric tube robots have demonstrated the potential to impact a multitude of surgical procedures since their recent inception, their youth is evidenced by the lack of commercial systems. Transitioning these robots from proof-of-concept prototypes in

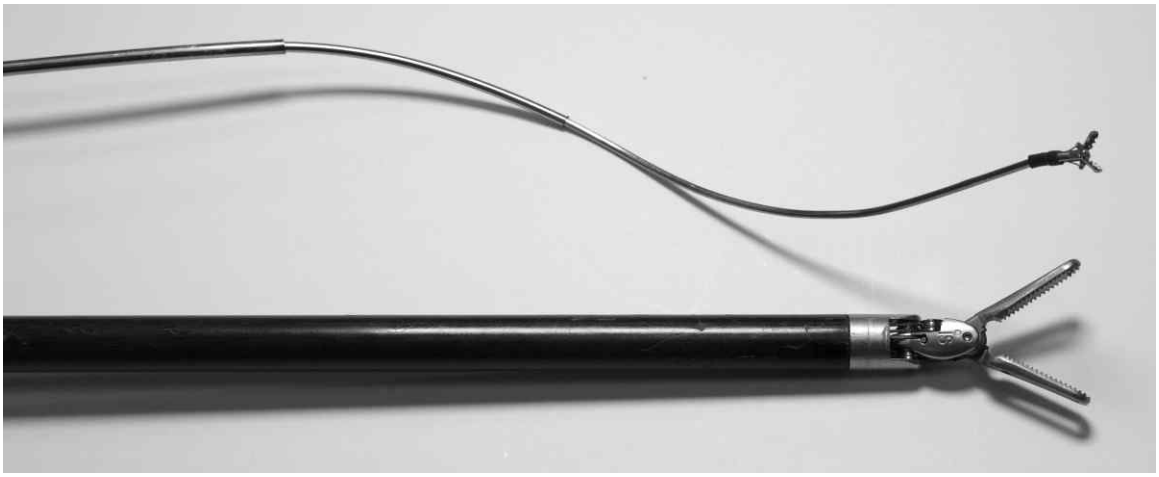

Figure 1.4: Size comparison between a typical concentric tube robot and a standard da Vinci laparascopic tool. (Reproduced from [5] by permission from Springer Nature: Robotics Research, ©2016)

clinically-ready systems requires several additional factors to be considered during the design process.

Arguably, the most critical (and inflexible) constraint for regulatory approval is also one of the most often omitted: sterilization. While perhaps counterintuitive, this is usually a pragmatic decision. Sterilization requirements greatly restrict the design space, and pose unique challenges. Even the da Vinci Surgical System has much room for improvement [18], despite two decades of research and experience. The primary goal for many of the concentric tube robots developed to date has been to evaluate feasibility in a new application. Thus, it can sometimes be wise to relegate complex matters of sterility to future work. Undaunted, a few researchers have designed concentric tube robots which aim to address sterilization.

A key differentiator in the design solutions proposed is the choice of where to define the sterile barrier. The simplest (to understand, not necessarily design) is to have no sterile barrier, i.e., the entire device is sterilizable. This is the case for the majority of surgical instruments as it is generally the easiest and least expensive. There are two ways to utilize this method; ensure all components can be adequately cleaned and sterilized after a

procedure, or throw it away. The difficulty in taking this approach with concentric tube robots can be found in their name—robot. Designing motors and electronics to withstand cleaning and sterilization is challenging, and their expense usually precludes the disposable option. While a fully autoclavable manual concentric tube device has been described [14, 19], no reusable robotic concentric tube systems have been demonstrated. However, at least two attempts have been made at disposability. Graves et al. [20] created a potentially disposable design featuring a plastic screw-spline drive mechanism designed for inexpensive manufacturing and assembly, and Zhu et al. [21] presented a robot with a total cost under $70.

Since the motors and electronics present the largest obstacle to sterilization, another option is to define the sterile barrier between them and the rest of the robot. Burgner et al. [22] were the first to demonstrate this approach in a concentric tube robot. Their design (see Fig. 1.5) featured a sterilizable and biocompatible robot with a detachable (non-sterile) motor pack. The motor pack coupled to the robot through a sterile bag. This same method was later adopted by Yu et al. [23].

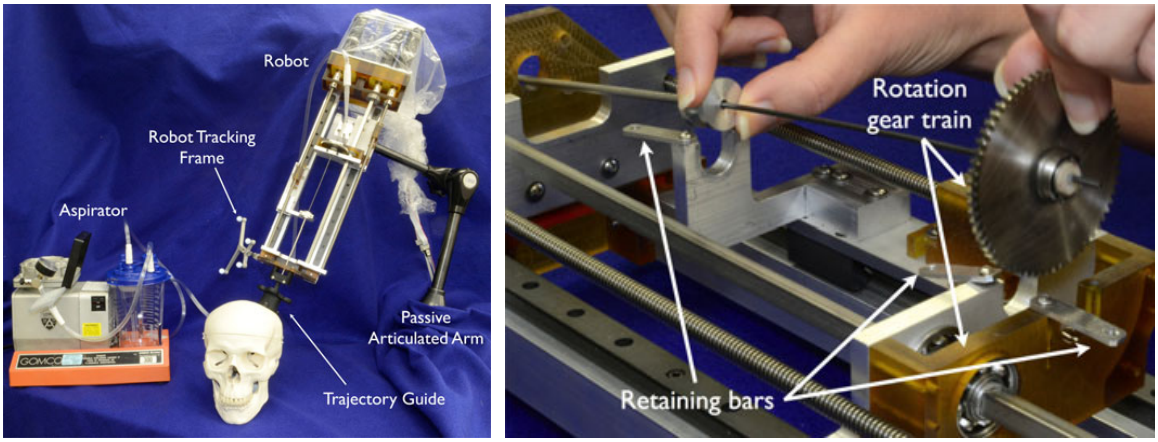

(a) (b)

Figure 1.5: (a) A sterilizable concentric tube robot system for intracerebral hemorrhage evacuation, which featured a detachable motor pack for use with a sterile bagging procedure and (b) a quick-release mechanism to enable changing tubes during a procedure. (Reproduced from [22], ©2013 IEEE)

In addition to sterilization, surgical workflow considerations must be addressed. Each

specific procedure will dictate its own unique requirements, but that does not mean every concentric tube robot must also be unique. The commonalities should be studied in order to find adaptable solutions that can be integrated into future designs. A 2003 review of medical robotics by Taylor and Stoianovici [24] highlights the commercial advantages of a surgical robot that can "be readily adapted to multiple tools or end-effectors ... since so much of the cost of these systems is related to development and regulatory approval costs rather than manufacturing." If only one tool is needed at a time, a single-arm robot with interchangeable tubes might suffice. The sterilizable robot by Burgner et al. [22] took this approach for intracerebral hemorrhage evacuation. Figure 1.5b shows the quick-release mechanism that enables a set of tubes to be replaced during the surgical procedure. If multiple tools must be used in concert, then a multi-arm robot is the only solution. Bimanual (two-arm) systems have been designed for prostate surgery [15], neurosurgery [25], and transnasal approaches for nasopharyngeal carcinoma [23] and pituitary tumors [13]. A quadramanual (four-arm) robot has also been developed for transnasal procedures [26].

1.3 Cochlear Implant Surgery

1.3.1 Overview

Cochlear implants (CIs) are a neuroprosthetic device capable of restoring hearing to those with profound sensorineural hearing loss. A typical CI (shown in Fig 1.6) consists of two main components: the external sound procesor worn behind the ear and the internal receiver/stimulator implanted during a surgical procedure. The processor analyzes incoming sounds picked up by a microphone, converts them into electrical signals, and sends them to the transmitter coil. The transmitter is coupled to the implanted receiver coil, allowing the signals to be wireless transmitted through the skin. These electical pulses then travel to the electrode array inside the cochlea, stimulating the cochlear nerve to create the perception of sound.

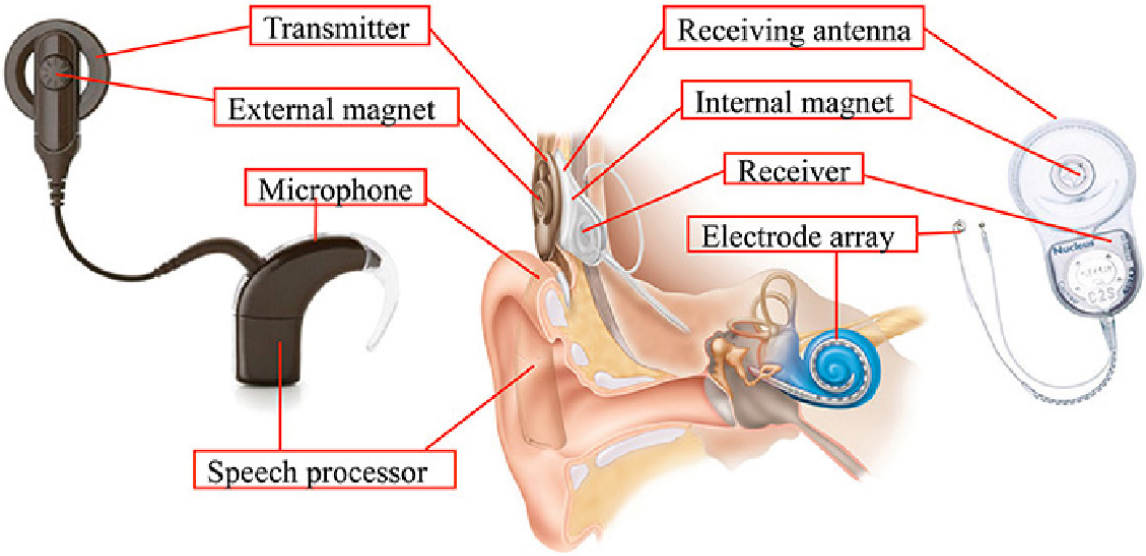

Figure 1.6: The external portion of a cochlear implant uses a microphone and speech processor to transmit signals to the internal portion, which are then converted into electrical pulses sent to the electrode array inside the cochlea.

The origins of modern cochlear implants began in the 1950s, when André Djourno and Charles Eyriès created the first device designed to restore hearing via electrical stimulation. It was implanted in a patient in Paris in 1957 [27]. This early prototype was manually constructed of a single coil (providing one stimulation channel) embedded in epoxy resin and a polyethylene-coated stainless steel wire, which they placed in contact with the auditory nerve. Although primitive in comparison to the multi-channel electrode arrays available today, the patient was able to distinguish between different stimulation frequencies. With practice, the identification of a small set of words was even possible.

News of this eventually reached the United States and began a period of slow but steady progress through the 1960s and early 1970s. A turning point came in 1977, when a report was published evaluating the 13 patients in the U.S. that had currently had cochlear implants [28]. The encouraging conclusions of the report led the National Institutes of Health (NIH) to considerably increase funding of cochlear implant research. As the devices became more sophisticated (e.g. multichannel electrode arrays and continuous interleaved sampling), speech outcomes improved, which in turn increased demand. These compound-

ing effects led to an exponential growth from 3000 patients with CIs in 1988, to 12,000 in 1995, to 120,000 by 2008 [29]. As of 2016, it is estimated there are over 600,000 CI recipients worldwide [30].

Although CIs have had dramatic impact on the lives of many, there is still room for progress. Clinical outcomes of cochlear implant surgery exhibit a wide distribution, with many patients reporting difficulty perceiving speech in noisier environments [31, 32, 33, 34]. One of the key improvement areas identified relates to the insertion of the electrode array. To see why, it is necessary to first understand what makes this procedure challenging.

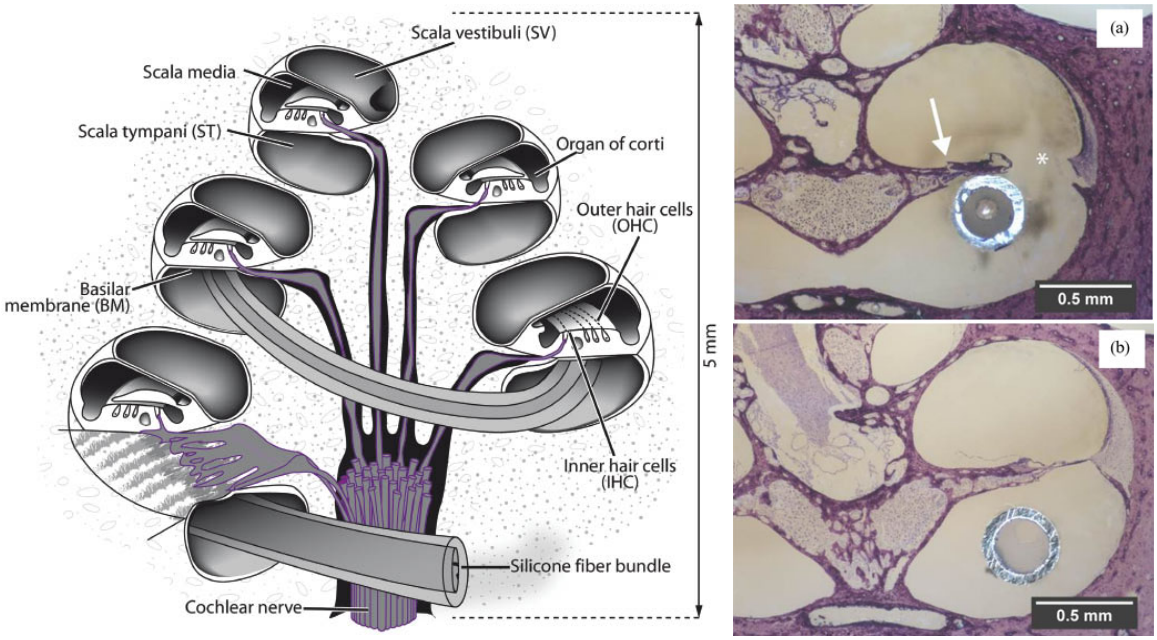

(a) (b)

Figure 1.7: (a) The cochlea consists of three helical channels separated by thin membranes. During insertion into the scala tympani, electrode arrays can rupture the delicate inter-scalar partition and translocate into the scala vestibuli. (b) Histological cross-section images by Wade et al. [35] comparing a tramatic insertion (above) to an atraumatic insertion (below). The location of the electrode array can be identified by the platinum ring of an electrode. ©2014 IEEE

The cochlea (Fig. 1.7a) is a small, intricate, helical structure consisting of three fluid-filled channels separated by thin membranes. The electrode array is typically placed into the channel known as the scala tympani. Due to the spiral shape, the array becomes con-

tinually more difficult to insert as the frictional forces increase. This leads to two potential problems: intracochlear trauma and/or incomplete insertion.

Intracochlear trauma refers to the damage caused by the electrode array scraping or pushing on the sensitive anatomy inside the cochlea. The most common victim is the inter-scalar partition separating the scala tympani and the scala vestubuli (see Fig. 1.7b). The inter-scalar partition consists of the osseous spiral lamina, Reissner's membrance, and the basilar membrane. The basilar membrane serves the vital function of transforming incoming sounds waves into mechanical vibrations that move the hair cells, causing them to create the electrical impulses sent to the auditory nerve. Experiments have shown that forces as low as 42 mN can rupture the inter-scalar partition [36], very near the minimal force perceptible by humans [37]. This means that despite the utmost care by experienced surgeons, translocation of the electrode array occurs in 25-33% of cases, resulting in the loss of any residual hearing [38, 39].

Incomplete insertions occur for the same reason: the friction builds up until it reaches a point where the electrode array cannot overcome it without buckling. Even if trauma is avoided, speech outcomes are still negatively impacted [40]. Reasons for this are twofold. First, incomplete insertions can leave one or more electrodes outside the cochlea. In the best case, these are deactivated by the audiologist, reducing the number of usable channels. However, incidence of extracochlear electrodes is underreported. One study of 262 patients found that 35 (13.4%) had at least one extracochlear electrode, but only 9 were reported by surgeons [41]. The correct number of extracochlear electrodes were identified in only 2 of those 35 cases. If these electrodes are left activated they can cause electrical interference, hindering speech perception. The second problem with incomplete insertions is that it reduces the frequency range accessible. Nerves near the basal end of the cochlea are responsible for the perception of high frequency tones, while lower frequencies waves propagate deeper before stimulating nerves more apical. These lower frequencies are particularly important for discerning speech. Indeed, Chakravorti et al. [42] found that "depth

of insertion was the most significant factor" in predicting audiological outcomes.

These goals—reducing trauma and improving placement of the electrode array—have motivated the introduction of robotics to CI surgery. The following sections will review prior research into the ways in which robotics has pursued enhancing electrode array insertion.

1.3.2 Robotic Insertion Tools

The first reported use of robotics in the context of CI surgery occurred in 2006 when Zhang et al. [43] introduced a robotically-actuated, tendon-driven custom electrode. Pulling on an embedded Kevlar thread caused the electrode to bend with a curvature designed to match the cochlea. They reported a 70% reduction in insertion forces in a 3:1 scale model of the scala tympani. This was the start of further exploration into using robotic insertion tools to better understand and model frictional effects. In experiments with 1:1 scale phantoms and commercially available electrode arrays, Zhang et al. [48] observed that insertion forces are a function of both angular depth and insertion speed. Later, a second-generation robot (Fig. 1.8a) added two additional DOF to control approach angle and axially rotation of the electrode [44]. Pile et al. [45] developed a similar parallel robot (Fig. 1.8b), but with a more near-term clinical focus. They studied cadaveric temporal bones to derive design criteria, and demonstrated reduced forces while inserting standard commercial electrode arrays into a phantom model.

The introduction of minimally-invasive approaches to CI surgery [49, 50] called for specialized insertion tools capable of deploying electrode arrays through a narrow access tunnel. The first of these was developed by Hussong et al. [51] and used two linear actuators to insert electrodes through a guide tube. Schurzig et al. made several enhancements to this design, such as an improved gripping mechanism, a smaller diameter guide tube, and integrated force sensing [46] (Fig. 1.8c).

While a variety of robotic insertion tool designs have been explored thus far, their basic

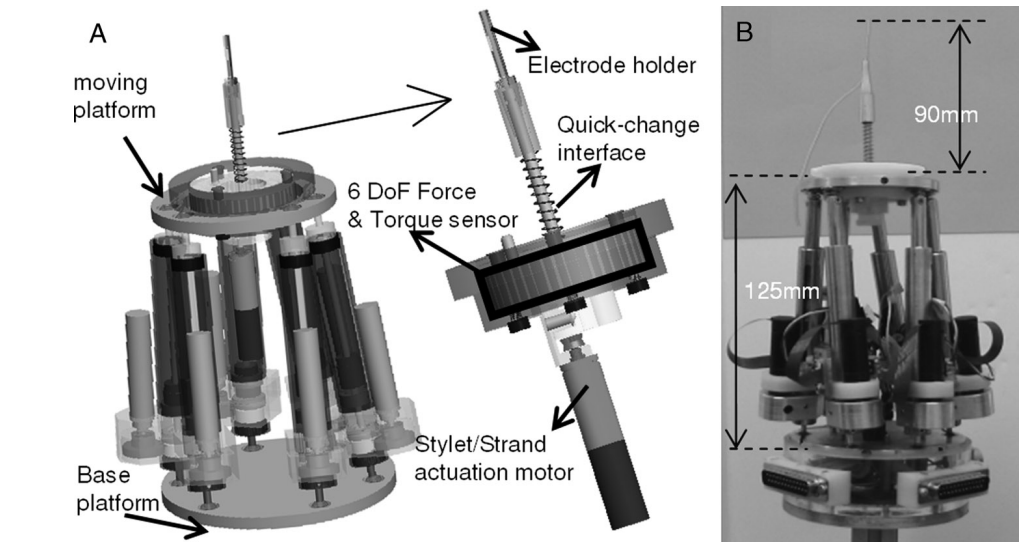

(a)

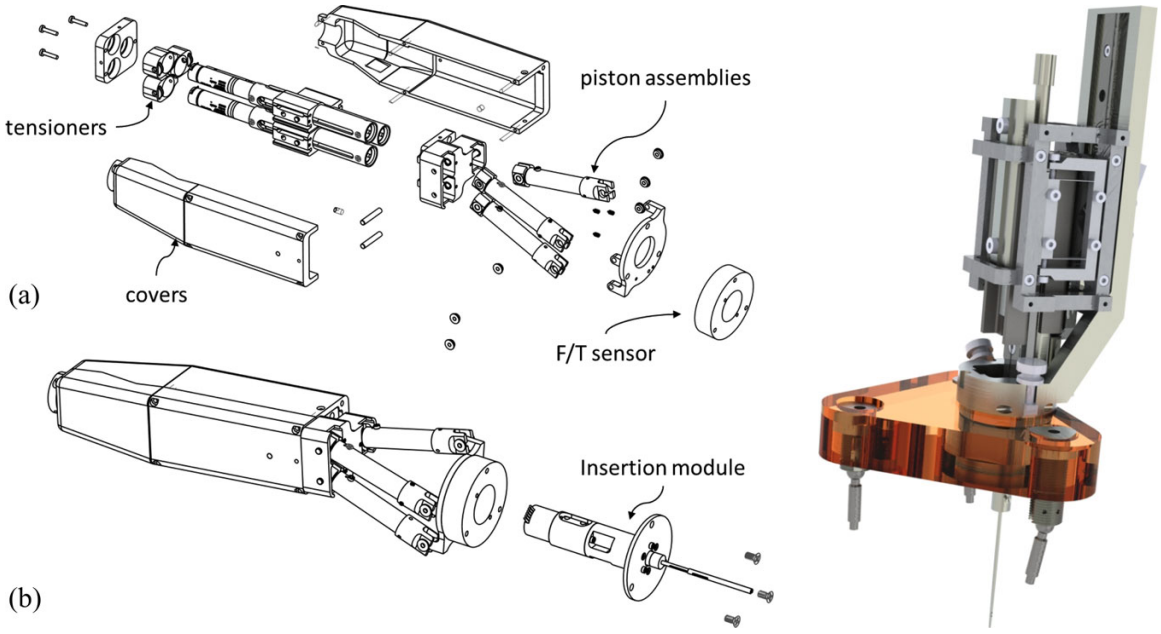

(b) (c)

Figure 1.8: Some of the first robotic insertion tools developed for CI surgery were: (a) A parallel robot design by Zhang et al. [44] using a custom steerable electrode with 4-DOF (reproduced with permission of Wolters Kluwer Health), (b) A similar, but more clinically-focused system by Pile et al. [45] capable of deploying clinical electrode arrays (©2014 IEEE), and (c) a 2-DOF insertion tool by Schurzig et al. [46] designed to mount onto a sterotactic frame for use in a minimally-invasive approach [47] (©2012 IEEE).

goals are the same—atraumatically introduce electrode arrays in a controlled and repeatable manner. In a realm where every millimeter and millinewton matters, robots have proven they are up to the task.

1.3.3 Magnetic Steering

The experimental results of the systems developed by Zhang et al. (in particular [52]) underscored the benefits of using a steerable electrode in addition to just a simple insertion tool. However, the regulatory pathway for a completely new type of electrode array can be time-consuming. What if you could steer an electrode without physically touching it? While this may conjure up images from science fiction, you do not need to look further than your refrigerator for a solution: magnets.

The idea of utilizing magnetic fields to steer continuum medical devices has a longer history than one might presume. Published accounts in the literature can be found as early as 1944, when Mayer [53] discussed clinical results of using an electromagnet to steer a magnet-tipped intestinal tube through the pylorus. A few years later, Devine and Devine [54] used a permanent magnet for the same application. Intriguingly, the authors alluded to unsuccessful prior attempts by others, mentioning an "electromagnet used forty years ago ... reported to be as large as a piano." In 1951, Tillander [55] discussed preliminary experiments conducted on cadavers and live animals in which he magnetically guided a cardiac catheter with an articulated steel tip.

In all of these early explorations, the surgeon manipulated the external magnetic field (generated either by a permanent magnet or an electromagnet) by hand. The challenge of unintuitive control combined with the limitations of magnetic materials at the time (neodymium magnets would not be discovered until the 1980s) led research efforts to focus instead on other methods of steering catheters (e.g. pull wires). It would not be until the rise of surgical robots in the 1990s that magnetic steering would receive renewed interest. This led to the development of the Stereotaxis Niobe Robotic Magnetic Navigation System

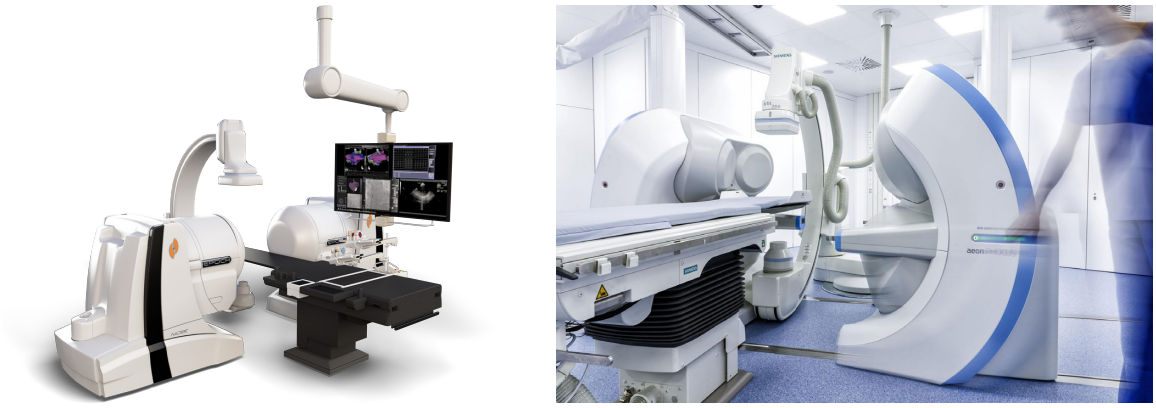

(a) Niobe ES (b) Aeon Phocus

Figure 1.9: Examples of commercial systems that use magnetic fields to steer magnet-tipped cardiac catheters. (a) The Niobe ES (Sterotaxis Inc., St. Louis, MO) robotically controls a pair of large permanent magnets, while (b) the Aeon Phocus (Aeon Scientific Ltd., Zurich, Switzerland) uses solenoid arrays.

(Fig. 1.9a), which became the first commercially available robotic system for magnetic navigation when it received regulatory approval in 2003. The Niobe (and current generation Niobe ES) system actuates two large permanent magnets to steer a magnet-tipped catheter. A similar system, the Aeon Phocus (Fig. 1.9b), uses electromagnets and was approved for clinical use in 2015.

The use of magnetic steering in the context of CIs was initially proposed in a 2006 patent application [57]. However, the first demonstration of magnetically steering an electrode during insertion was published by Clark et al. in 2011 [56]. They designed a benchtop system (Fig. 1.10) consisting of a 1-DOF insertion tool and a 2-DOF permanent magnet. Experiments with a 3:1 scaled electrode and scala tympani produced a 50% reduction of insertion forces. Leon et al. [58] continued investigation by performing insertions with three different magnet-tipped commerical electrode arrays (modified by the manufacturer) into 1:1 scale scala tympani phantoms with either a cochleostomy or a round-window opening. They found that insertion-force reduction was statistically significant for all combinations tested.

These proof-of-concept systems have demonstrated that the benefits shown by custom

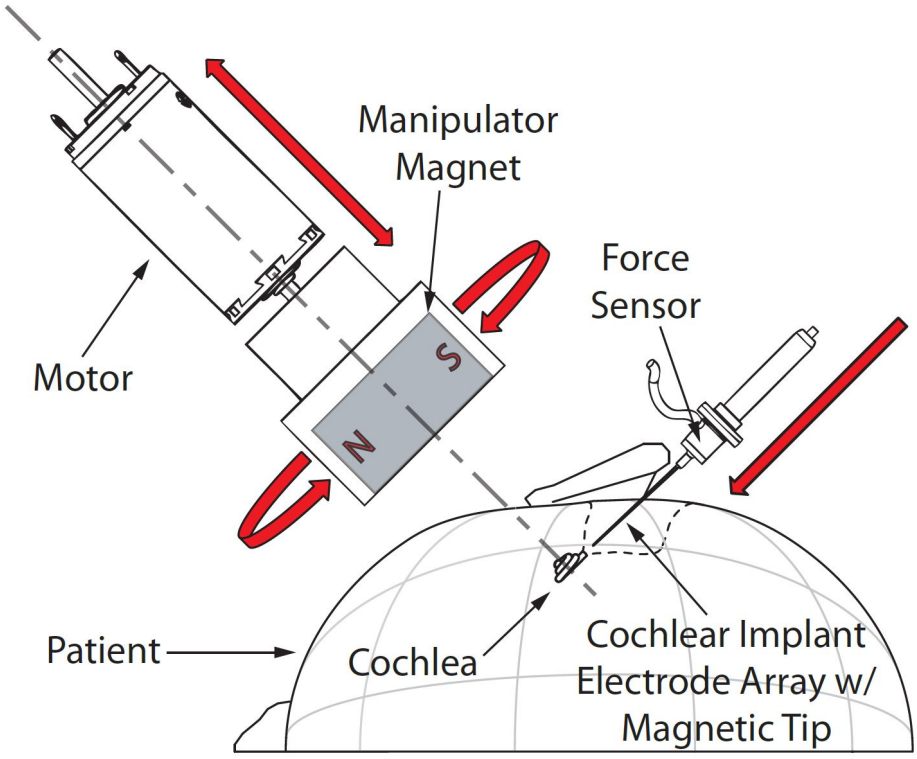

Figure 1.10: Concept for magnetically steered cochlear implant surgery by Clark et al. [56] (©2011 IEEE)

steerable electrode arrays can be achieved using clinically-available arrays with the aid of robotic magnetic steering. However, this is just the first step toward a system ready for use in the operating room. Areas that must be addressed include: patient safety, surgical workflow considerations, patient-specific planning, and insertion tool developments.

1.3.4 Sensing for Closed-loop Control

The majority of robotic approaches for electrode array insertion use open-loop control, meaning they execute a preprogrammed set of instructions. In contrast, closed-loop control uses sensory feedback to make adjustments during operation. For this reason, closed-loop control is generally preferred. The challenge in CI surgery is that most of the common choices for sensory feedback are not possible. The narrow, helical shape of the cochlea cannot be imaged by external (no line-of-sight) or internal (too small) cameras, ruling out

machine vision or optical tracking. Magnetic tracking coils are too large to fit alongside the electrode array. Custom electrode arrays have been designed which incorporate strain gauges [59, 60] or scanning electron microscopy [61] for position sensing, but integrating sensors into existing electrode arrays is not currently feasible. Thus far, only two sensing modalities have been applied to clinical electrodes: force and electrical impedance.

Force sensing has been used since the first robotic insertion tool was introduced [43], and has served as the standard metric for evaluating insertion quality. The forces are often measured by attaching the phantom cochlea or temporal bone to the sensor. This arrangement provides a better measurement of the forces experienced by the anatomy than if it is attached to the insertion tool. While useful for benchtop testing, in a clinical setting the force sensor could only be mounted to the insertion tool. It is more difficult to interpret forces from this frame of reference, which might explain why there is only one published example of using force measurements for closed-loop control during insertion. Pile et al. [62] developed a hybrid position-admittance controller that enabled a robotic insertion tool (Fig. 1.8b) to correct for initial alignment errors and demonstrated a reduction of insertion forces in temporal bones. Pile et al. also [63] characterized frictional forces during insertion into cadaveric temporal bones and developed a classification model to detect electrode tip fold over events. This was later extended to enable the online prediction of tip fold over before it occurs [64].

The inherent drawback to force sensing is that it relies on reaction loads between the electrode array and the cochlea to increase before a correction can be applied. Ideally, an adjustment would be made *prior* to forces developing. Electrical impedance sensing has the potential to do just that. Impedance measurements are a routine component of CI programming. They are used by audiologists to evaluate electrode function and aid in determining appropriate electrical stimulation levels. Tan et al. [65] were the first to explore the utility of impedance measurements for position sensing. They found a detectable change in bipolar (electrode-to-electrode) impedance between insertion techniques maintaining modiolar

wall contact vs lateral wall contact. These findings were later confirmed by Pile et al. [66]. Giardina et al. [67] presented a technique to characterize the electrode-saline interface in an effort to extract the access resistance component of the total impedance, which they found to have the highest correlation with electrode-modiolar distance in plastic phantoms. Though there are no published reports of using electrical impedance as feedback for closed-loop insertions, Pile's dissertation [68] presents experimental data in phantom models that used impedance feedback to guide stylet removal. These promising results provide much motivation for future research.

1.4 Dissertation Overview & Contributions

The overall aim of this dissertation is to advance the design of mechatronic systems to help deliver this new generation of flexible devices into the human body in a manner that is both safe and conscious of the surgical workflow.

1.4.1 Experimental Contributions

- **Orbital Tumor Resection**: Concentric tube robots are small enough to be deployed transnasally and were shown to be capable of removing pituitary tumors [13]. In Chapter 2, a transnasal multi-arm concentric tube robot system is presented and used to conduct the first robotic removal of tumors growing behind the eyes in the orbital apex region. This has not been previously attempted with a surgical robot and demonstrates how this versatile robotic platform may be useful for a variety of transnasal procedures.

- **Magnetically-steered Cochlear Implant Insertion in Cadaver**: Chapter 3 introduces a system for steering magnet-tipped cochlear implant electrode arrays with an electromagnet. Feasibility is demonstrated by performing the first magnetically steered insertion into a cadaveric cochlea. This is an essential step in the progression

from prior proof-of-concept prototypes, which used plastic cochlea phantom models.

- **Real-time Localization of Cochlear Implants in Cadaver**: Several techniques have been proposed which leverage impedance measurements to estimate the electrode-to-modiolus distance of a cochlear implant [66, 67]. However, it has not yet been shown whether accurate and real-time predictions can be made. Chapter 4 proposes the first online method for localizing cochlear implant electrode arrays using bipolar impedance measurements. The accuracy of the method is then experimentally validated.

1.4.2 Workflow-Conscious System Design

The transition from a laboratory proof-of-concept to a system ready for use in the operating room requires design changes that take into consideration how the device will fit into the surgical workflow.

- **Transnasal Concentric Tube Robot System**: It is common (and often necessary) for the surgeon to switch between several different surgical tools during a procedure. Multi-arm concentric tube robot systems have been developed, but quickly changing tools has not been possible [23, 69, 13, 15]. A key contribution of Chapter 2 is the introduction of the first concentric tube robot system with interchangeable tool cartridges. Modular customized motor control electronics were developed along with advancements in the software architecture to enable changing instruments while the system is running. A quick lock mechanism is also included which is designed to be operated while wearing surgical gloves and requires no tools. These advancements can all be incorporated into future clinically-focused designs.

- **Magnetic Steering System for Cochlear Implants**: In prior research, benchtop systems have demonstrated that magnetically steering cochlear implants during insertion can reduce intracochlear forces [70, 58]. Chapter 3 builds upon this work by taking

important steps toward a clinically-viable system for magnetically steering cochlear implant electrode arrays. Inserting the electrode array in the presence of very large magnetic fields required developing the first non-magnetic robotic insertion tool for cochlear implants. Preoperative imaging is analyzed to determine the optimal trajectory, and image guidance is integrated to ensure proper tool alignment. The utility of these developments is not contingent on magnetic steering and should prove useful for other approaches. Additionally, the flexibility of the custom electronics presented in Chapter 2 is further exemplified by using them to control the electromagnet.

1.4.3 Patient Personalization

Healthcare is in the midst of a pivotal shift from standardized treatments to 'personalized medicine' (also referred to as 'precision medicine'). This dissertation makes several contributions towards this goal.

- **Optimal Cochlear Implant Trajectory**: The magnetic steering system presented in Chapter 3 for improving cochlear implant surgery relies on patient personalization. This is a necessary step in order to bring prior benchtop systems [70, 58] into the operating room. A computed tomography (CT) scan of the patient's head is segmented and analyzed to determine the optimal angle to insert the electrode array. This method, developed by Noble et al. [71, 72], has never before been applied to magnetic steering applications. The 3D model of the patient's cochlea is used to compute the magnetic field vectors necessary to steer the electrode array along a safe trajectory. An optical tracking system is combined with custom image guidance software to ensure the robotic insertion tool and the electromagnet are precisely aligned according to the prescribed plan. None of these techniques have been previously applied in the context of magnetic steering.

- **Real-time Localization Method for Monitoring Cochlear Implant Insertions**: To

enable closed-loop control of electrode arrays along a patient-specific trajectory, a means of sensing electrode position relative to anatomy is needed. Toward this goal, we contribute a method for localizing electrode arrays based on electrical impedance measurements. Prior research [73, 66] has demonstrated that a detectable relationship exists between electrode impedance and distance from the modiolar wall. However, in these studies the distance was measured post-insertion in order to fit a model. A primary contribution of Chapter 4 is a method for estimating electrode-modiolar distance in real-time as the the electrode array is deployed. This will facilitate future efforts in ensuring that the electrode array safely follows the prescribed patient-specific path during insertion.

Chapter 2

Concentric Tube Robot System for Transnasal Surgery

2.1 Chapter Overview

In the development of telemanipulated surgical robots, a class of continuum robots known as concentric tube robots has drawn particular interest for clinical applications in which space is a major limitation. One such application is transnasal surgery, which is used to access surgical sites in the sinuses and at the skull base. Current techniques for performing these procedures require surgeons to maneuver multiple rigid tools through the narrow confines of the nasal passages, leaving them with limited dexterity at the surgical site. This chapter presents a complete robotic system for transnasal surgery featuring concentric tube manipulators. It illustrates a bagging concept for sterility, and intraoperatively interchangeable instruments that work in conjunction with it, which were developed with OR workflow compatibility in mind. The system also includes a new modular, portable surgeon console, a variable view-angle endoscope to facilitate surgical field visualization, and custom motor control electronics. Furthermore, we demonstrate elastic instability avoidance for the first time on a physical prototype in a geometrically accurate surgical scenario, which facilitates use of higher curvature tubes than could otherwise be used safely in this application. From a surgical application perspective, this chapter presents the first robotic approach to removing tumors growing behind the eyes in the orbital apex region, which has not previously been attempted with a surgical robot. The manuscript of the chapter has been submitted to *The International Journal of Robotics Research*.

2.2 Introduction

The transnasal approach enables minimally invasive access to a wide variety of surgical sites in the head, but is not more widely used because of the challenges of operating in

small, highly constrained workspaces. Manipulating multiple hand-held tools (including an endoscope) with rigid shafts simultaneously through the nasal passages is challenging for the physician. Anatomical constraints and tool collisions both impose formidable obstacles to working dexterously at the surgical site, and some targets are simply out of reach with current manual tools.

These factors have motivated the development of robotic systems to assist in transnasal surgical approaches. Some systems have focused on accurate image-guided drilling of bone to access the surgical site [74, 75], and others have robotically manipulated the endoscope to assist the surgeon [76, 77]. While these systems address access to the surgical site and visualization, robots with distal dexterity are useful for performing complex maneuvers at the surgical site.

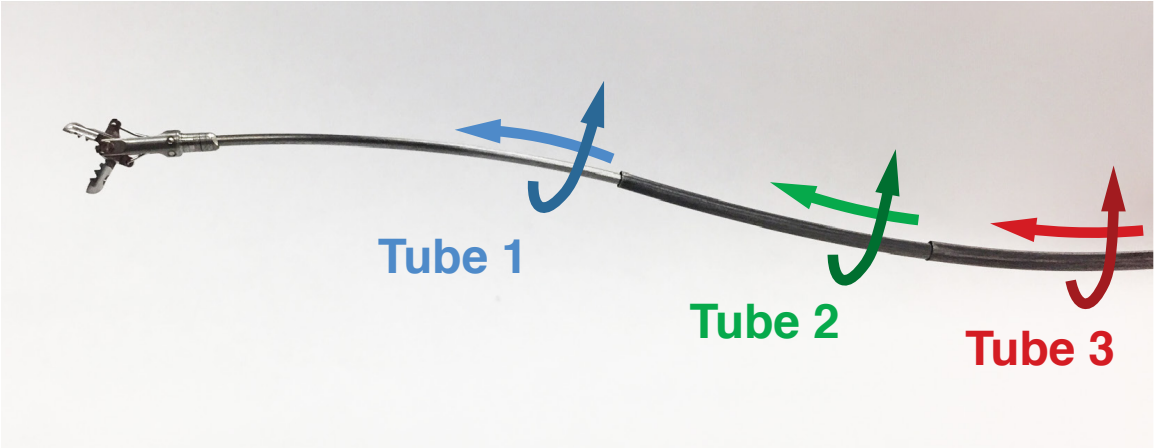

Figure 2.1: Three-tube concentric tube robot. Each tube can be translated and rotated relative to the others to produce elastically-balanced motion of the overall structure.

Continuum robots [4], which possess flexible bodies, are an ideal solution to the anatomical constraints imposed in transnasal procedures. These robots have been proposed for other delicate procedures in constrained workspaces, including, for example, intravascular procedures [78] and neurosurgical procedures [79]. Robotic continuum endoscopes have been designed to provide visualization within the sinuses [80] and nasopharynx [81], and transnasal robots have also been proposed for micro-surgery of the throat [82] and surgery within the maxillary sinus [83]. The flexibility of continuum robots enables them to nav-

igate around anatomical obstacles and reduces the risk of accidental injury to the patient. Perhaps most importantly, continuum robots are inherently scalable, with submillimetric diameters achievable for some robot designs [4].

Among continuum robots, the concentric tube robot (shown in Figure 2.1) can perhaps be scaled to the smallest overall diameters [4, 5]. These robots consist of several nested, flexible tubes (often composed of superelastic Nitinol), each of which can be shape-set into a desired curved shape at its distal end. Once the tubes are assembled concentrically, they are translated and rotated relative to one another by an actuation unit which grasps each tube at its proximal end. This results in elastic interactions between the tubes, causing the overall structure to bend and twist. Concentric tube robots have been applied to a variety of other surgical applications, including intracerebral hemorrhage evacuation [12], transoral peripheral lung biopsy [84], transurethral prostate surgery [15], neuroendoscopy [11], and cardiac interventions [85].

The unique advantages of concentric tube robots have led researchers to propose them for transnasal surgeries [13, 26, 86, 23, 87]. Much of this work has focused on pituitary tumor removal and biopsy. These systems provided the foundational work for the system described in this chapter. This prior work has focused on proof of concept, and left to future work many developments needed to create a complete surgical system for delivery of concentric tube robots in the context of endonasal surgery.

This chapter presents a complete transnasal surgical system featuring concentric tube manipulators. Important advancements include (1) an OR workflow-compatible method for draping non-sterile components, (2) the first intraoperatively interchangeable concentric tube instruments which can be readily exchanged as single units, complete with end effectors, and motor control electronics developed specifically for this high-degree of freedom (DOF) surgical robot (the system in this chapter has 21 DOF), (3) the first modular, portable surgeon console designed for use with a concentric tube robot system, (4) a new visualization approach for surgical robots involving integration of a variable view-angle

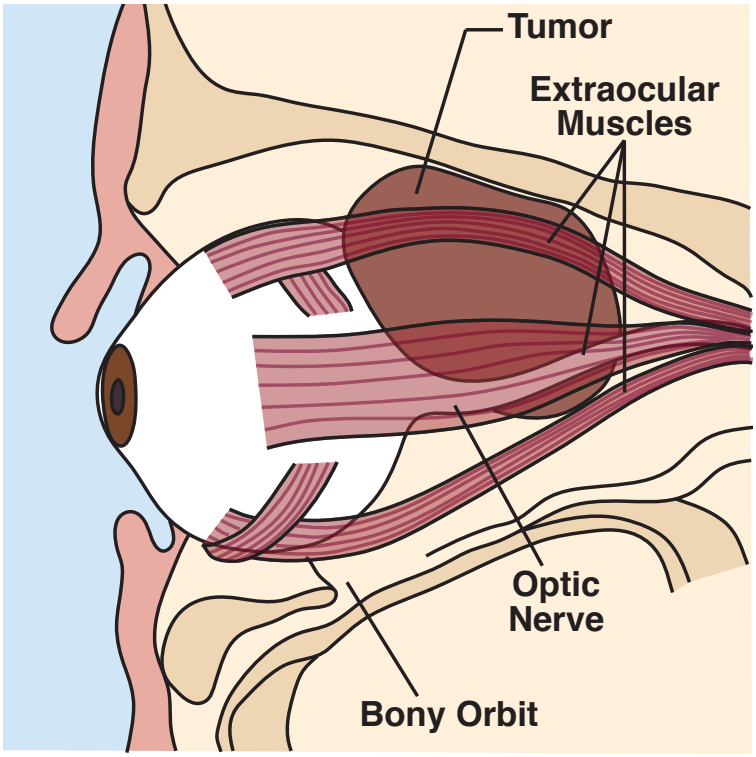

Figure 2.2: Anatomy of the orbit with a tumor behind the eye, which can produce pressure on the eye, optic nerve, and extraocular muscles.

endoscope, (5) the use of elastic instability avoidance for the first time on a physical prototype in a geometrically accurate surgical scenario, which facilitates use of higher curvature tubes than could otherwise be used safely, and (6) the first robotic approach to removing tumors growing behind the eyes in the orbital apex region, which has not previously been approached with a surgical robot.

2.3 Medical Motivation: Orbital Tumors

A variety of benign and malignant lesions can occur in the eye orbit that require surgical removal. The orbit is the socket in which the eye resides (see Figure 2.2), which contains a complex collection of structures. These include the optic nerve and the extraocular muscles that control eye motion, which are surrounded by fat and connective tissue. Traditionally, tumors in this area are removed via open surgical procedures [88]. Recently,

toward reducing invasiveness and facilitating better access to and visualization of the tumor, otolaryngologists and opthalmologists have teamed up to remove these tumors collaboratively, aided by a transnasal approach [89, 90, 91]. The opthalmologist approaches the tumor through a small incision near the eye, while the otolaryngologist assists using a transnasal approach. On the transnasal side, the otolargyngologist uses a rigid endoscope and rigid tools to approach the target. After performing a septoplasty to increase range of motion within the nose, a small opening in the bone between the nasal passage and the orbit is created with a surgical drill to enable transnasal access to targets behind the eye.

Despite the promise of these emerging techniques, there remain many challenges associated with them. For example, the constraints of the nasal passages make dexterous tool motion at the surgical site challenging. In addition, the tumor can be hidden behind muscles and other tissues, requiring the surgeons to carefully retract them to access it. Coordinating motions between two surgeons with two different approaches and viewpoints adds another level of difficulty to this task. Surgeons performing the procedure have noted that it is so difficult that "it is paramount to have specialized [future] instruments" developed specifically for this procedure [89]. Providing such a specialized tool is the purpose of this chapter. The above factors make the dexterity and small diameter afforded by concentric tube robots highly desirable for removing tumors in the orbit. Furthermore, an instrument that enhances maneuverability and range of motion could one day enable a purely transnasal approach, further reducing invasiveness.

A variety of tumors grow in the orbit. The experiments in this chapter consider cavernous hemangioma [92], the most common tumor occurring in the orbit in adults [93]. These tumors are encapsulated, typically round or ellipsoidal masses that must be surgically removed to avoid compressive damage to the optic nerve and associated vision loss, as well as potential corneal damage [94]. In Section 2.6 we construct a geometrically accurate phantom model of the orbit containing these tumors, and resect them using the robot described in this chapter.

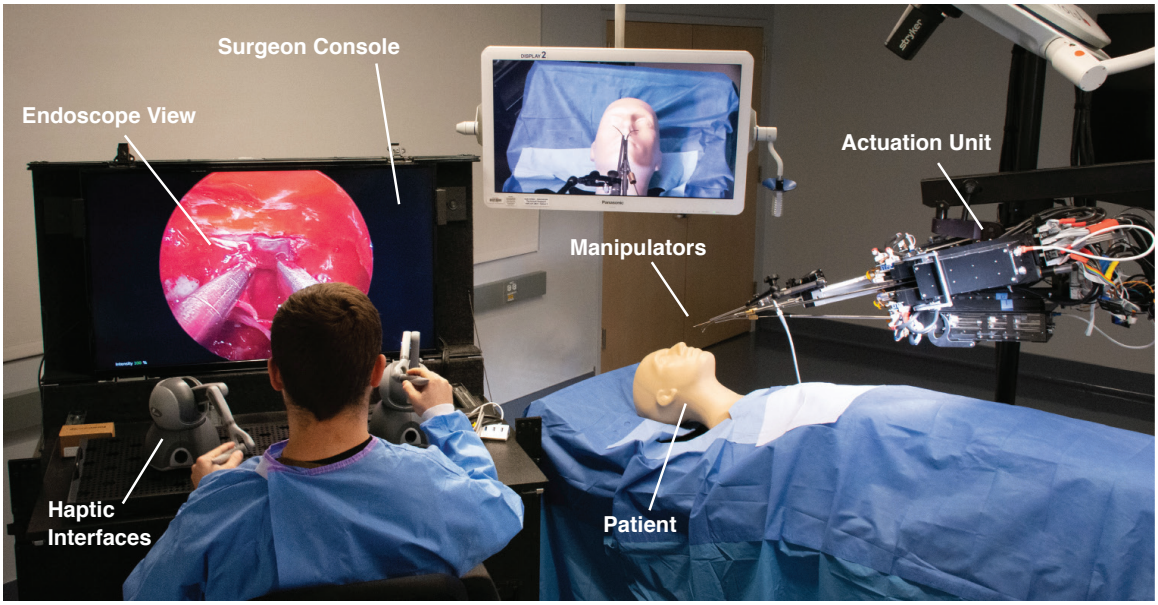

Figure 2.3: The complete system in an operating room setting, with the robot mounted over the patient and the operator seated at the surgeon console.

2.4 System Design

The complete system, including the patient-side robotic platform and surgeon control console, is shown in a mock operating room setting in Figure 2.3. A diagram of the major components of the system, and how they are connected is presented in Figure 2.4. The surgeon teleoperates the robot via two haptics-capable input devices and three foot pedal clutches (one for toggling each tool module). A high-definition display provides information to the surgeon in the form of endoscopic video and robot status information, within a graphical user interface (GUI). Custom motor controllers are responsible for the closed-loop control of the motors in the actuation units, which drive the concentric tube tool modules. These subsystems communicate over TCP/IP with a high-level controller using the Robot Operating System (ROS) [95]. The design of the individual components is described in the following subsections.

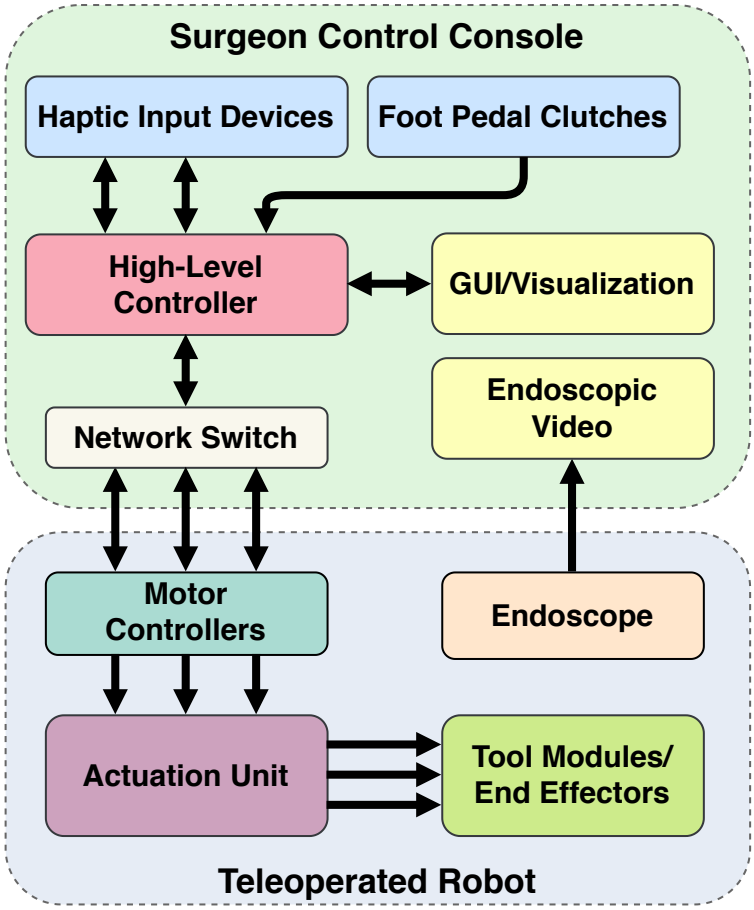

Figure 2.4: The surgical system is physically divided into two primary components. The surgeon sits at the control console and uses the surgeon input devices and foot pedals to teleoperate the robot, which is positioned over the patient.

2.4.1 Actuation Unit and Tool Modules

One of the key features of this robotic system in comparison with prior transnasal concentric tube robot systems is its implementation of interchangeable tools. Similar surgical systems have approached this in a variety of ways, such as manually operated instruments passed through robotic overtubes [96], exchangeable end effectors mounted onto permanent robotic arms [97], or concentric tube robots with removable tubes [12, 23]. Our system is the first multi-arm concentric tube robot where the tubes, end effectors and their respective driving mechanisms are integrated into modular, interchangeable tool cartridges. It consists of a single base actuation unit and individual tool cartridges (see Figure 2.5) that

attach to the base. The actuation unit has the capacity to drive up to three three-tube concentric tube manipulators simultaneously. The motivation for this modular design is twofold. First, from a clinical workflow perspective, it is valuable to be able to quickly remove tools and install new ones, enabling tool changes during a procedure as needed. Incorporating the transmission elements (linear rails, lead screws, gears, etc.) and tubes into a single instrument cartridge simplifies this process in comparison to our earlier systems, which required removing small screws on a retaining bar to release the tubes [12]. Figure 2.6 demonstrates how a quick lock mechanism and alignment pins on the base facilitate cartridge installation. This new design can be easily operated while wearing surgical gloves and requires no additional tools. A single user can complete the entire tool change process in less than a minute.

Second, the modular, cartridge-based design enables motors, encoders and other electronics, to remain non-sterile, and be isolated from the patient behind a sterile drape, as shown in Figure 2.7. Since the cartridges themselves consist primarily of passive transmission elements, they can be manufactured as either disposable or reusable instruments.

The sterility concept is inspired by the da Vinci system from Intuitive Surgical, Inc. [98], the most widely used telemanipulated surgical robot, and was first applied to concentric tube robots by Burgner et al. [12]. This system builds upon that earlier design with a focus on improving usage in the OR. In particular, requirements for tools and precise alignment during setup has been eliminated. The tool modules couple into the actuation unit through a set of spring-loaded shaft couplers (shown in Figure 2.5), which mate the transmission elements in each cartridge to the motor shafts on the actuation unit. In a commercial version of this system, the drapes would be manufactured with plastic adaptors fused into them to create a sterile seal around the transmission coupling. The six brushless DC motors that mate through the drape (Maxon Motors, EC-13) control the rotations of all three tubes, the translation of the two innermost tubes within the cartridge (via leadscrews), and the motion of an end effector. A seventh brushless DC motor (Maxon Motors, EC-16)

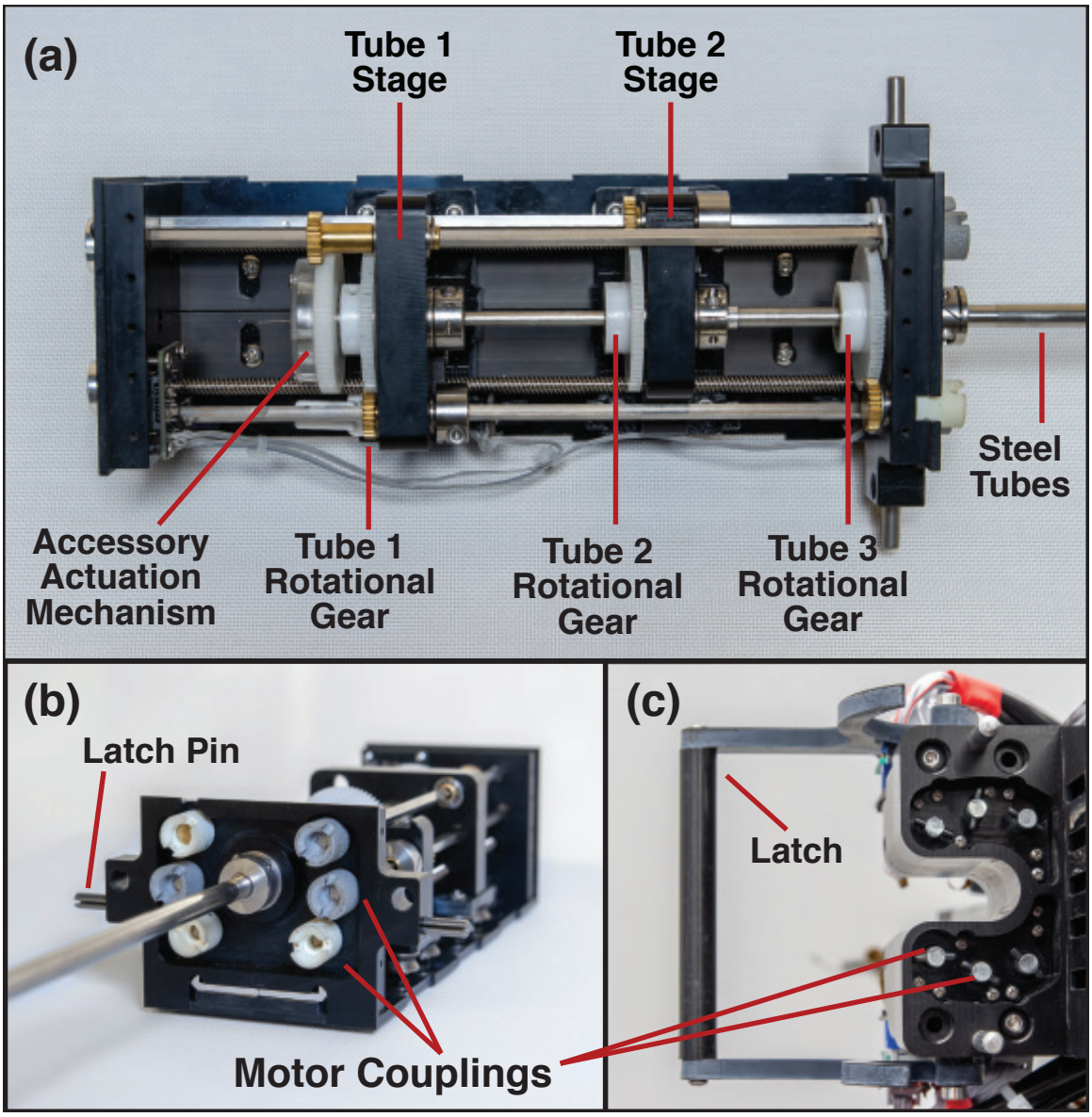

Figure 2.5: The tool cartridge design. (a) The internal components of the tool cartridge which translate and rotate the tubes, (b) The end of the tool cartridge with coupling elements that mate to the robot actuation unit, and (c) The portion of the actuation unit which mates to the tool cartridges via spring-loaded couplings.

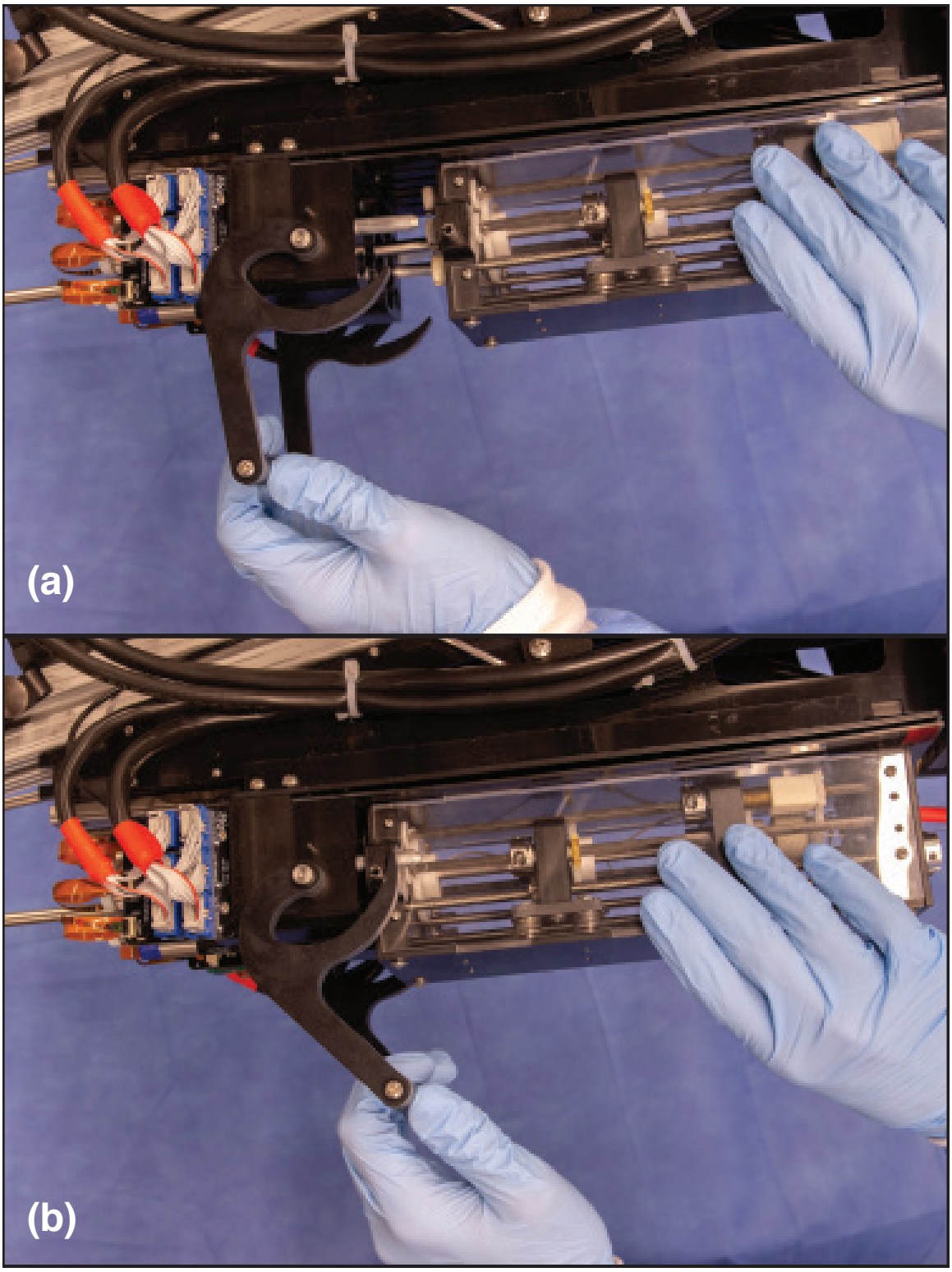

Figure 2.6: The lever-based locking feature allows for tools to be easily exchanged. (a) The user inserts the tool module, feeding it onto the alignment pins, and (b) The user brings the latch feature down, locking the tool module in place and coupling it into the motors.

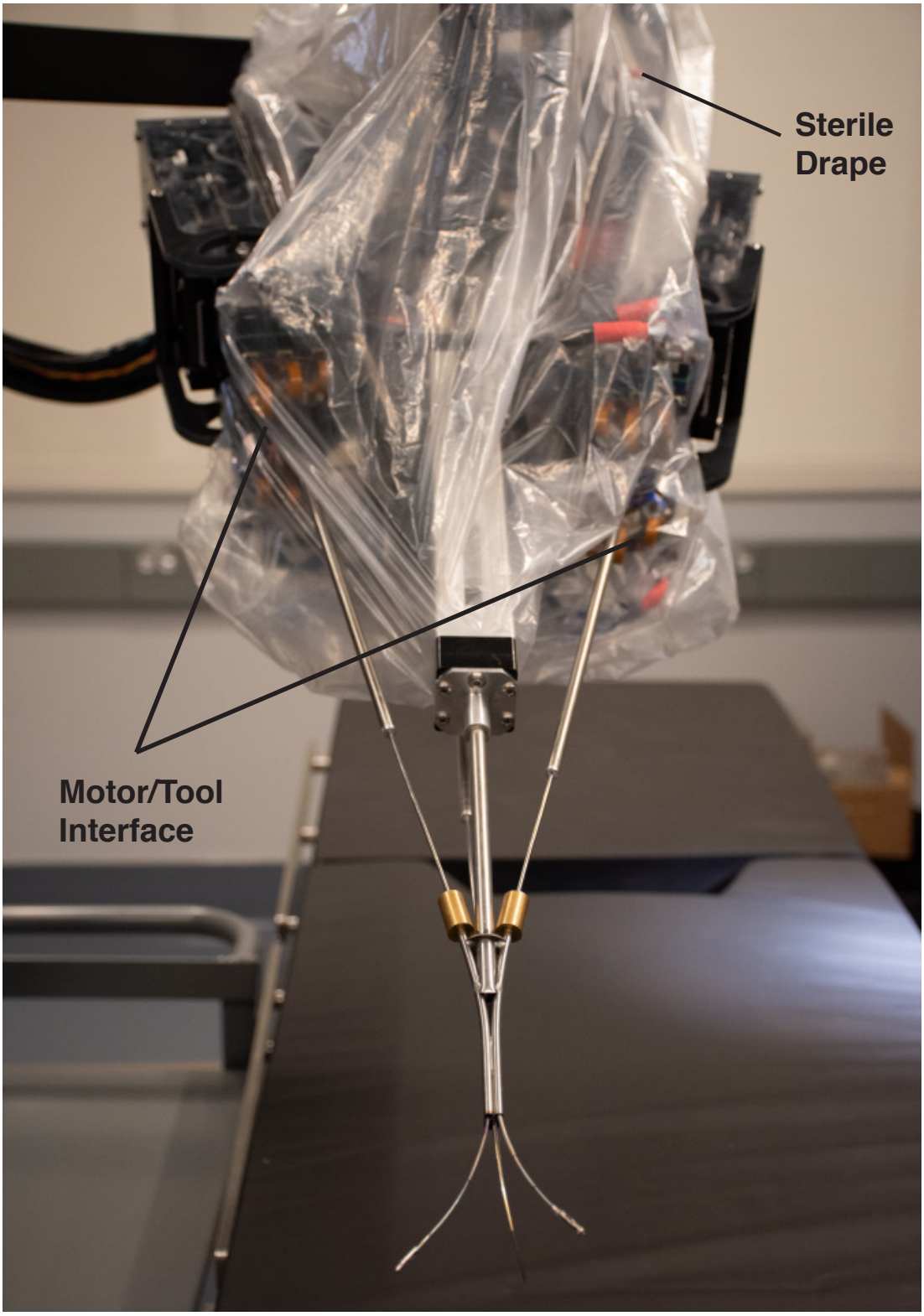

Figure 2.7: Sterility concept, with motors and encoders isolated from the patient behind a sterile drape. The concept is for sterile tool cartridges to mate to the motors through adapters built into the drape.

translates the entire cartridge along a track on the actuation unit via a leadscrew.

Another important aspect of this actuation unit design is its ability to deploy all of the manipulators into the patient in close proximity to one another; the narrowest portion of the workspace is the nostril opening, which is approximately 16 mm by 35 mm [26]. The track for each cartridge is angled inward toward a tube collimator, shown in Figure 2.8. This enables the tubes to be actuated off-axis, enabling easy loading of the cartridges onto the robot. To reduce the build-up of torsional strain energy in the nitinol tubes as they

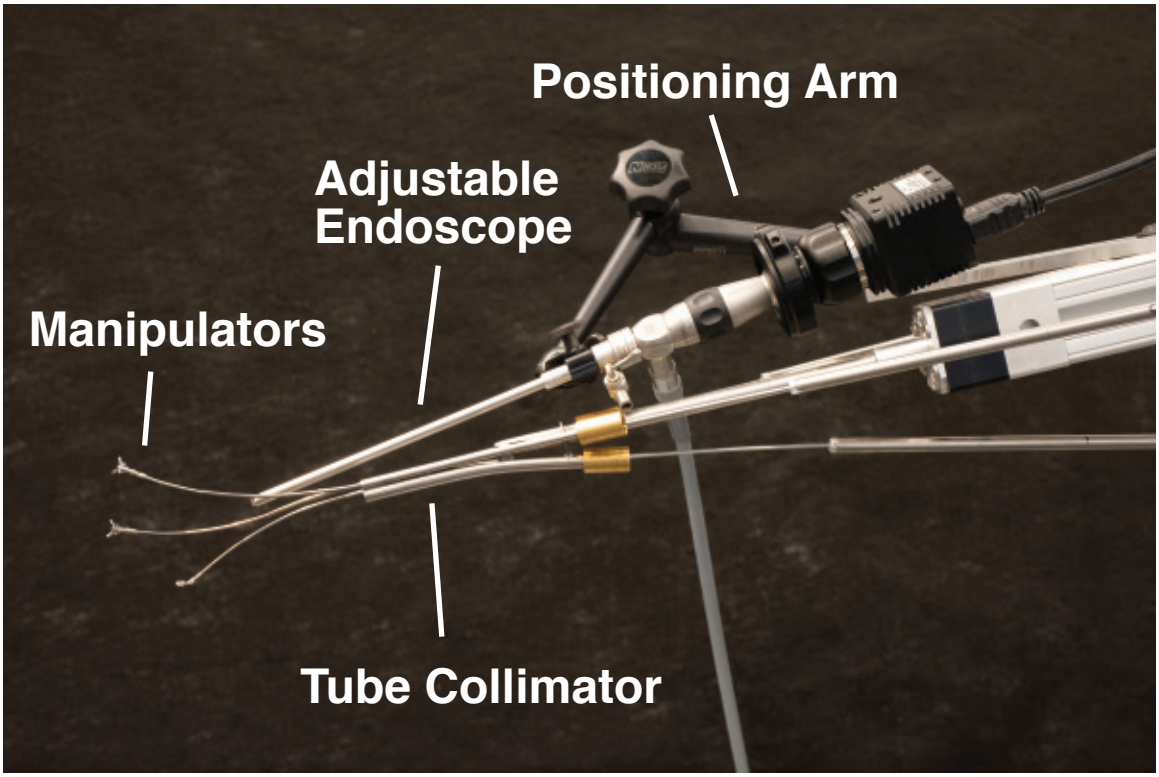

Figure 2.8: Front end of the robot, with tube collimator collecting the three concentric tube manipulators. The adjustable endoscope is mounted on a lockable positioning arm. Concentric tube arms are shown in a state of maximum extension from the collimator.

are actuated, stiffer, stainless steel tubes are used to span much of the length between the cartridges and the tube collimator, transmitting translations and rotations to each nitinol tube. This design feature, previously proposed in [99, 100], reduces the tendency for the tubes to undergo elastic instabilities in the robot's workspace [101, 102] (we also address this from a control perspective in Section 2.5). Each nitinol tube is attached to its own

stainless steel tube via a machined aluminum adapter and cyanoacrylate adhesive (Loctite). Each stainless steel tube is then affixed to its corresponding stage via a set screw in the rotational gear, and a shaft collar, which clamps it to its translational stage.

2.4.2 Robotic End Effectors and Endoscope

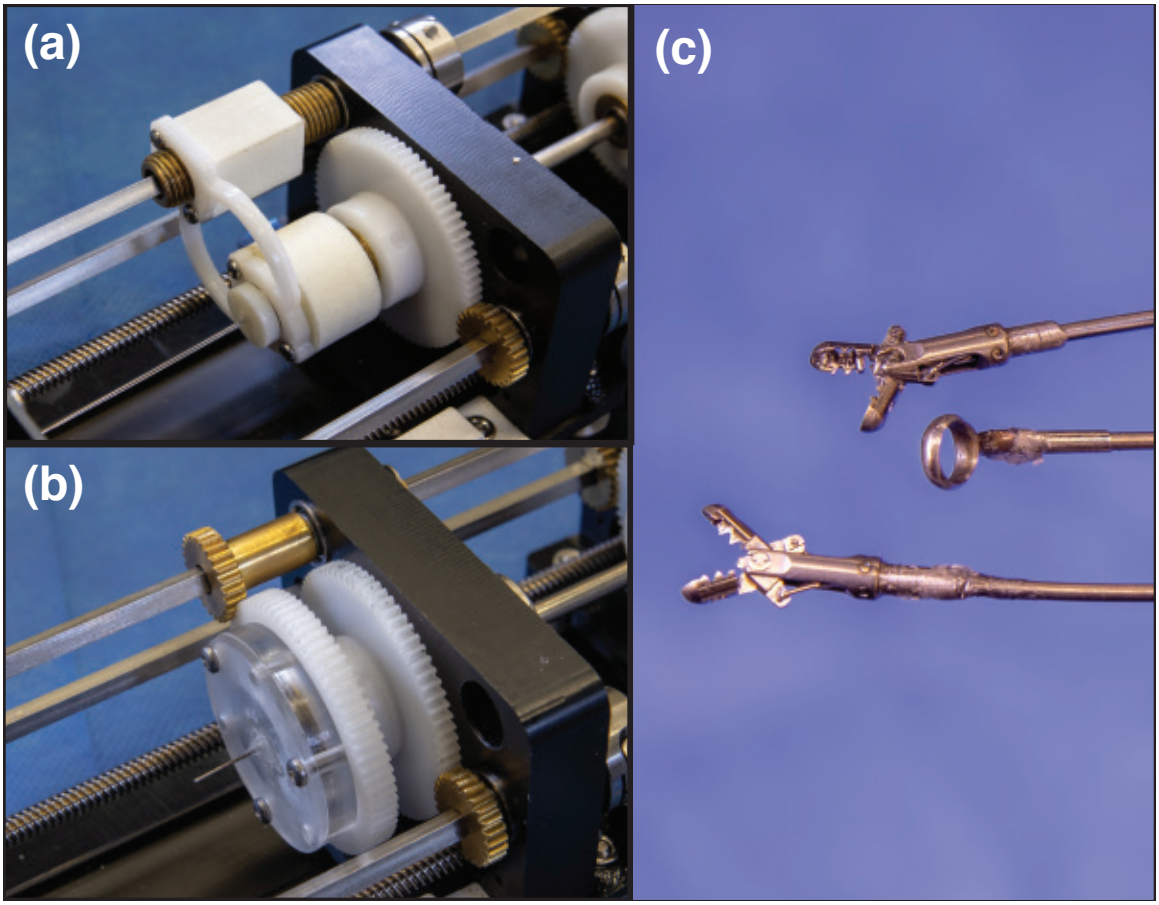

Figure 2.9: Example end effectors and corresponding actuation mechanisms, each of which is mounted to the back of the inner tube's translational stage. (a) Translational actuation mechanism used to open and close the gripper via a small lead screw. The tendon is attached on the inner ring of a bearing, enabling the tendon to rotate freely to prevent the accumulation of torsion. (b) Rotational actuation mechanism used to turn the curette via a set of gears. (c) Curette and gripper end effectors.

A variety of end effectors can be used with concentric tube robots: accessory actuation mechanisms within the cartridge have been designed for translation (Figure 2.9a) and rotation (Figure 2.9b) of tools passing through the lumen of the innermost tube.

The translation mechanism works by rotating a lead screw on a square shaft, and similarly the rotation mechanism turns a gear on a square shaft. For the set of experiments described in Section 2.6, one cartridge is equipped with a tendon-actuated gripper, one is equipped with a rotatable curette, and the other provides an auxiliary tool option, if needed.

For visualization of the surgical field, an adjustable view-angle rigid endoscope is mounted to the robot on a lockable positioning arm (Figure 2.3). The endoscope, the EndoCAMeleon (Karl Storz SE & Co. KG), is a 4 mm diameter endoscope with a view angle that is adjustable between 15 degrees and 90 degrees. This angular range, combined with the freedom to arbitrarily pose the endoscope, enables visualization of a large volume of the sinuses, skull base and orbit. The presence of three concentric tube arms also leaves open the option of equipping one of the arms with a chip-on-tip endoscope camera for future experiments (as in Yu et al. [23], e.g.); this could prove especially useful as we seek to approach even more difficult-to-reach targets in the future.

2.4.3 Electrical Hardware

We created custom printed circuit boards (PCBs) for motor control for this system. Our modular solution distributes the computational load among multiple units, each responsible for the real-time, synchronous, closed-loop position control of six motors (see 103 for a similarly modular motor driver design for surgical robots). This enables the use of microcontrollers rather than a traditional computer, reducing both cost and size. More importantly, this approach is safer in the event of a disconnection from the high-level control computer. The microcontrollers will ensure the motors simply remain fixed at their last commanded position.

A single motor control module, as shown in Figure 2.10, consists of a motherboard PCB with six sockets for daughterboard PCBs. On the motherboard is an ARM Cortex-M4 microcontroller (Teensy 3.2, PJRC.COM, LLC) that communicates with the high-level controller over TCP/IP using a WIZ850io Ethernet module (WIZnet Co., Ltd.). Each mother-

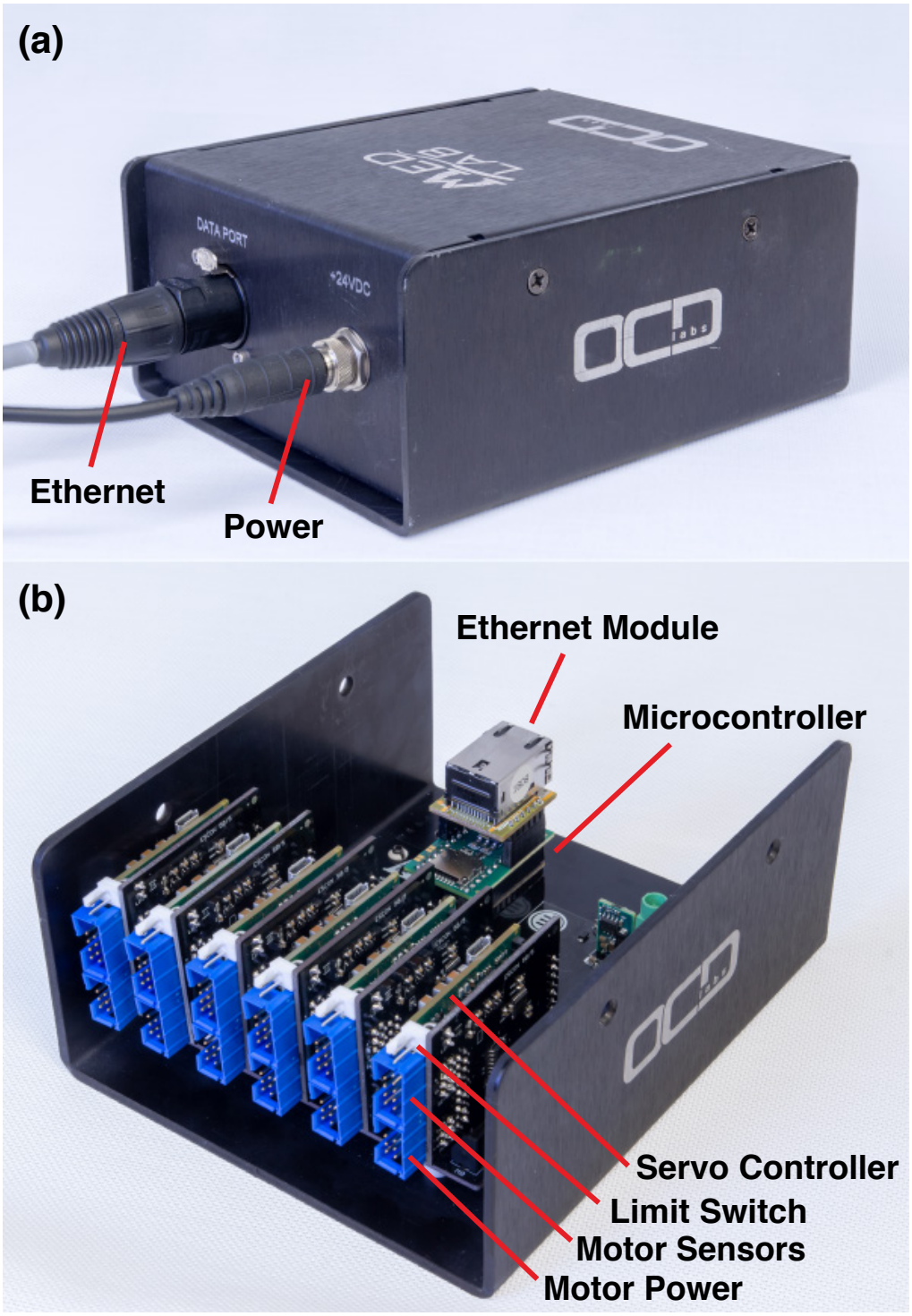

Figure 2.10: The custom designed motor control PCBs assembled into their modular enclosure. (a) Ethernet and power are the only incoming connections necessary for operation. (b) A microcontroller on each motherboard provides closed-loop control of up to six motors while communicating with the high-level controller via an Ethernet connection. Each daughterboard contains its own servo controller, as well as standardized connectors that support a wide variety of motor types.

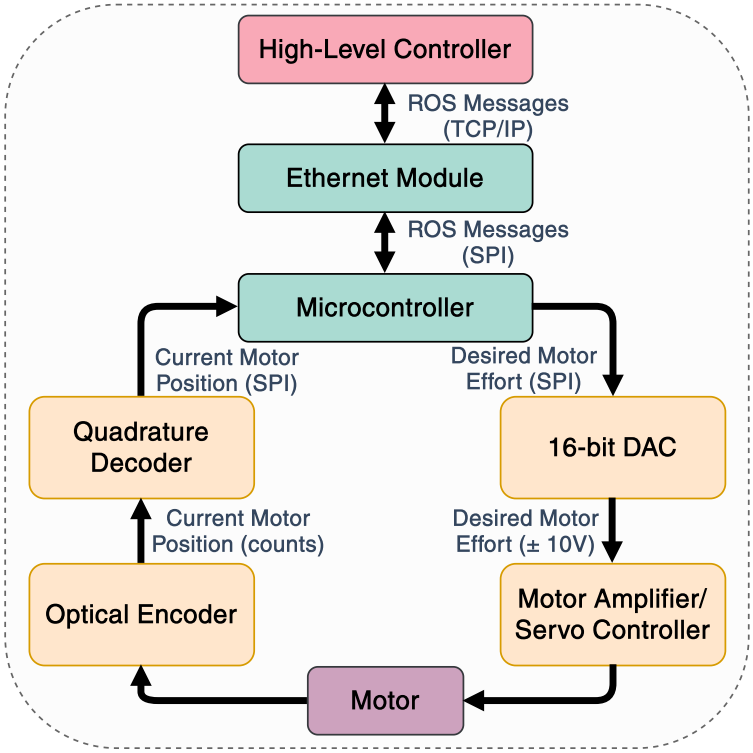

Figure 2.11: The high-level controller sends motor commands as ROS messages over TCP/IP to the Ethernet modules on the custom motor control PCBs. A microcontroller on each motherboard retrieves the messages over an SPI bus. PID controllers compute the desired motor efforts, which are sent to the DACs on each daughterboard. The servo controllers output a current to the motors proportional to analog voltage commands. Optical encoders on each motor produce pulses, which are counted by quadrature decoders to track position.

board is connected through a managed switch (Cisco SG-300). Thus, the computer running the high-level control requires only a single Ethernet connection to drive all 21 motors.

A diagram of the low-level control loop is shown in Figure 2.11. Each daughterboard contains a servo controller (Maxon Motors, ESCON Module 50/5) which drives a single motor in current control mode. Motor current is set via an analog input by a 16-bit digital-to-analog converter (Analog Devices, AD5761R). A quadrature converter (LSI Computer Systems, LS7366R) monitors motor position via an optical encoder (ELESTA, E OI R007). The daughterboards also provide an input for a limit switch, which is utilized for both emergency stopping and joint homing.

The microcontroller firmware is written using a state machine (event-driven) architecture. Separate proportional-integral-derivative (PID) controllers enable independent position control of its six motors at a rate of 1 kHz. High-level configuration and relevant data input/output (e.g. position commands) is provided over ROS topics. Creating this layer of abstraction means the motor boards become agnostic to the specific type of high-level controller used, making them much more flexible. For example, our system comprises multiple types of limit switches (optical/mechanical), encoders (optical/magnetic), and motors; however, all components of the same type appear identical to the high-level controller. Additionally, each daughterboard PCB uses the same design so they can be swapped between motherboards without requiring changes to the firmware. Since all identifying information (i.e. IP/MAC address and ROS namespace) is configured and stored to non-volatile EEPROM in the microcontroller, any power/Ethernet cable can be used with any motor control module; it is not possible to connect the modules incorrectly. It is the combination of all of these features that enabled us to create a modular, yet robust and safe, surgical robotic system.

2.4.4 Surgeon Interface Console

The custom surgeon console, shown in Figure 2.12, is a mobile cart, which houses the high-level control computer and human-machine interfaces (PHANTOM Omni haptic devices, 3DSystems, Inc.). Each pen-like device accepts 6-DOF input poses from the surgeon and is capable of providing force feedback. The surgeon console and robot actuation unit are connected via Ethernet.

A 42-inch high-definition monitor (NEC Corp.) is mounted to the surgeon console on a hinge and can be folded down for transport. The monitor displays endoscope video footage and a GUI that provides the surgeon information on the robot's status, as well as the ability to change various teleoperation settings during a procedure (e.g. level of motion scaling, which user input controls which tool, etc.).

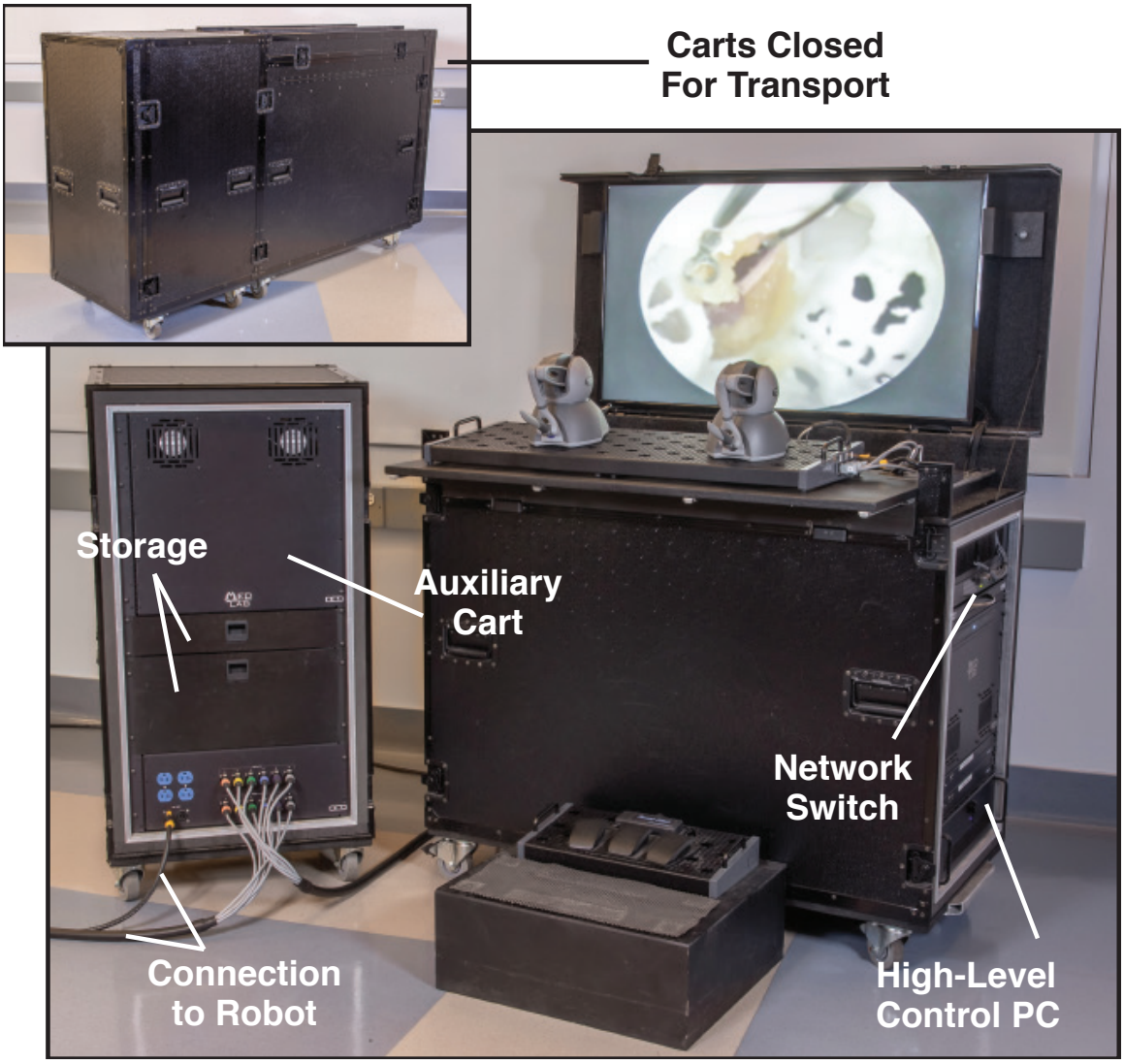

Figure 2.12: Custom surgeon interface console which houses the high-level control computer and user interfaces. The auxiliary cart is designed to house the low-level motor control boards and any robot-specific accessories that need to be stored, and connects to the robot via ethernet. It can be latched onto the main surgeon console cart for easy transport.

2.4.5 Tube Parameters

Each of the tube sets used for the experiments in Section 2.6 had an overall outer diameter (OD) of 1.9 mm with an inner lumen diameter (ID) of 0.77 mm, and was capable of extending from the tube collimator by approximately 110 mm. The precurved sections ranged in length (L_{curved}) from 180.0 mm to 308.0 mm, with curvatures (κ) from 6.7 mm^{-1} to 10.6 mm^{-1}. The full set of tube parameters for each tool is summarized in Table 2.1.

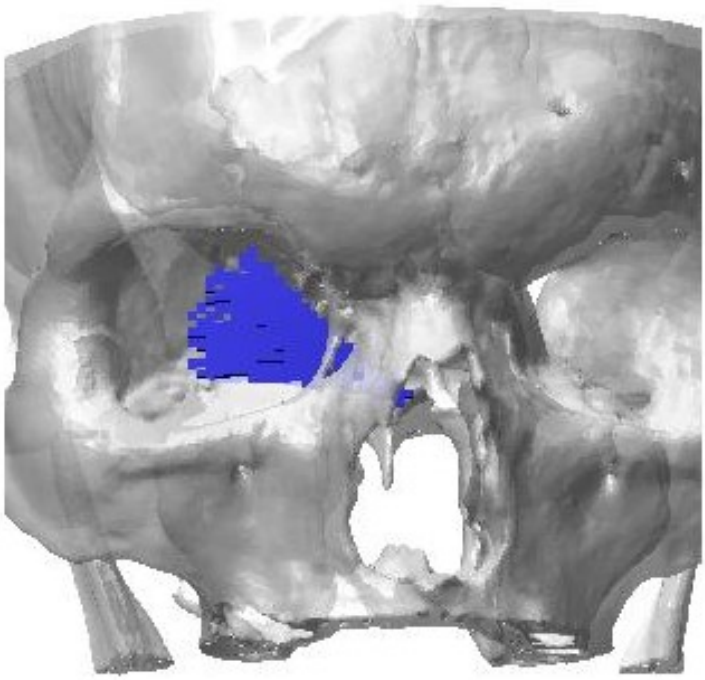

Figure 2.13: The achievable workspace (without collisions with the anatomy) of the gripper arm used in the experiments using one clinically feasible approach angle.

These parameters were heuristically selected to provide a stable workspace of the desired size with qualitatively good dexterity.

Figure 2.13 shows the achievable workspace of the gripper arm within the orbit (not including configurations which would interact with the bony anatomy) for one approach angle selected as clinically reasonable by an otolaryngologist. This volume was generated by sampling the joint space in simulation. The workspace shown in the figure represents a conservative estimate for the overall achievable working volume, since some amount of interaction with the bony anatomy is acceptable in practice, and the approach angle can be readily adjusted by the surgeon as needed. Optimization of the tubes is also possible, and has been demonstrated with a variety of objectives, such as reaching anatomical targets [85], covering volumes [104], and preventing elastic instability [105, 106]. Tube optimizations may be used to provide even better dexterity and workspace characteristics for this system, but these optimizations are outside the scope of this chapter and are left to

Table 2.1: Summary of the tube design parameters used in experiments.

	OD mm	ID mm	$L_{straight}$ mm	L_{curved} mm	κ mm^{-1}
Gripper					
Tube 1	1.01	0.77	66.7	287.0	6.7
Tube 2	1.52	1.29	50.7	245.0	8.3
Tube 3	1.90	1.70	30.0	180.0	9.1
Curette					
Tube 1	1.01	0.77	49.3	308.0	7.4
Tube 2	1.52	1.29	55.4	242.0	8.2
Tube 3	1.90	1.70	29.0	182.0	10.6

future work. It is worth noting that selecting tubes which are capable of 'snapping' (due to elastic instabilities) within the intended joint space is only practical when a snap-avoiding controller, such as the one described in Section 2.5 is employed.

2.5 Teleoperation Approach

The kinematic model used in this system is the widely used mechanics-based model for concentric tube robots based on Cosserat rod theory, described in Rucker et al. [9] and Dupont et al. [10]. This model is computed by integrating constitutive equations for the collection of tubes over arc length, given certain known boundary conditions. Evaluation of this model provides a full pose of the robot for any location along its arclength ($g(s)$), along with the Jacobian relating tip velocities to joint velocities (J). For teleoperation, we use the damped least squares resolved-rates approach [107], as applied to concentric tube robots by Burgner et al. [13] and Hendrick et al. [15]. In this approach, the manipulator Jacobian is computed at each servo cycle, and used to map the surgeon's desired velocity to the joint velocities that create a corresponding robot tip velocity. The joint velocities are determined by minimizing a weighted cost function (see 108, for a description of the use of weighted cost functions) that balances tracking the surgeon's desired tip velocity with secondary objectives such as avoiding robot joint limits.

In the experiments that follow, we also incorporate elastic instability avoidance as a term in the cost function using the method proposed in Hendrick [109] and demonstrated in Anderson et al. [110]. This relies on computing the stability metric, $\mathbb{S}$, as defined in Gilbert et al. [101], which decreases to zero as an unstable configuration is approached. The full cost function used is:

$$H = \frac{1}{2}\big((J\dot{q} - \dot{x}_{\text{des}})^T W_{\text{tracking}}(J\dot{q} - \dot{x}_{\text{des}}) + \dot{q}^T W_{\text{damping}}\dot{q} + \dot{q}^T W_{\text{joint limits}}\dot{q} + (\dot{q} - v_{\mathbb{S}})^T W_{\text{stability}}(\dot{q} - v_{\mathbb{S}})\big) \quad (2.1)$$

In this expression, the W matrices represent weighting functions for the objectives of task space tracking, joint velocity damping, joint limit avoidance, and instability avoidance, respectively. The joint velocity vector is represented by $\dot{q}$, and $v_{\mathbb{S}}$ represents a joint space velocity ascending the gradient of the stability metric ($v_{\mathbb{S}} = \alpha\frac{\partial \mathbb{S}}{\partial q}$, where α is a positive scalar). Appropriate definition of these weighting functions enables intuitive teleoperation while avoiding joint limits and unstable configurations as they are approached. Note that alternative approaches to redundancy resolution and elastic instability avoidance within a resolved rates framework have also been proposed and studied in simulation by Leibrandt et al. [111].

The addition of instability avoidance into the control law enables the use of more highly curved tubes that result in the manipulator having elastic instabilities in its workspace, which would have been ruled out a priori by some prior design algorithms [e.g. 106]. The set of tubes used for the experiments in Section 2.6 have curvatures high enough that elastic instabilities exist in the manipulator's workspace. These could not be safely used in our application without this elastic instability avoidance approach due to the risk of tissue damage.

Lastly, note that the above approach is facilitated by selecting variables with compu-

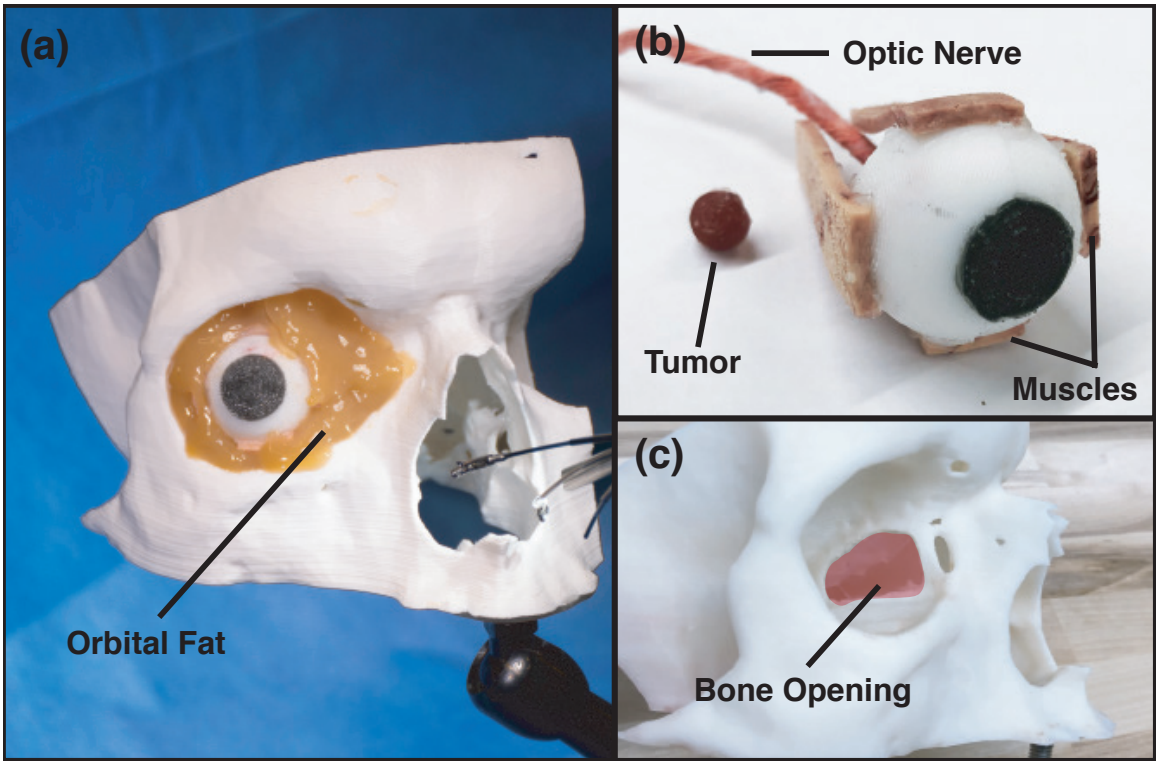

Figure 2.14: Phantom model used for orbital tumor resection experiments

tational efficiency in mind. It has been shown that it is possible to convert the forward kinematics problem for concentric tube robots from a boundary value problem (as it was traditionally formulated) to an initial value problem which was first mentioned by Bergeles and Dupont [112] and is described in detail by Gilbert [113]. The increased computational efficiency from this perspective shift is a key to enabling advanced control algorithms, such as real-time instability avoidance, within a resolved rates framework.

2.6 Orbital Tumor Resection Experiments

We began by creating a phantom model for cavernous hemangioma orbital tumors (see Figure 2.14). This consisted of a portion of the skull 3D-printed in plastic, an eyeball with attached extraocular muscles, and a 2.5 mm thick string to simulate the optic nerve, with an ellipsoidal tumor. The eyeball, muscles, and tumor were made from silicone. Ballistics gel was cast to surround the eyeball, tumor, nerve, and muscles to simulate orbital fat and

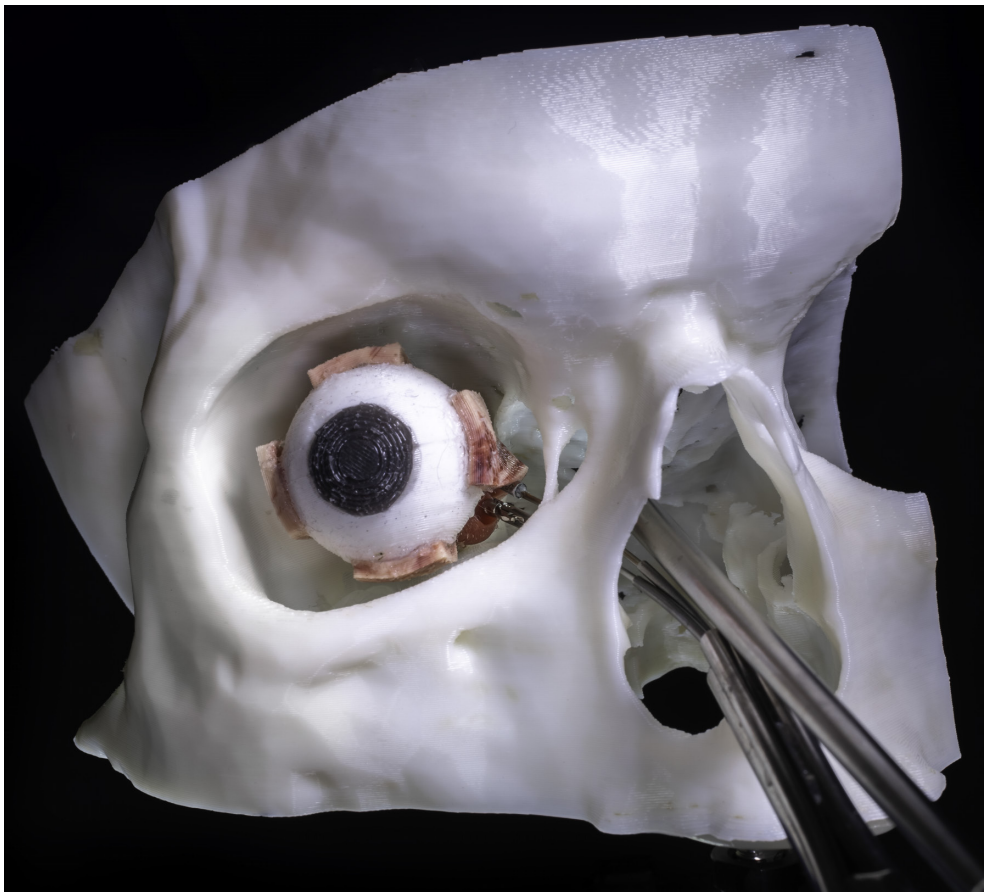

Figure 2.15: Experimental setup (with fat omitted for visualization). The tube collimator and endoscope are positioned transnasally, and the two surgical instruments (gripper/curette) perform the orbital tumor resection.

connective tissues.

To create the 3D printed eye socket and skull, a cranial CT scan was segmented in 3D Slicer [114]. The resulting volume was then smoothed and downsampled in Meshlab [115] and cropped to the eye socket and surrounding anatomy using Autodesk MeshMixer. The skull model was then 3D printed in ABS plastic using a Stratasys F170 FDM 3D printer. An area of the simulated bone was recommended for removal by an experienced rhinologist, to match what is typically removed to access the surgical site during this type of surgery.

Silicone eyeballs were molded using DragonSkin 10 Fast Platinum-Cure Silicone (SmoothOn, Inc.) in 3D-printed molds. The eyeball is represented by a one-inch diameter sphere, consistent with anatomical size ranges [116]. A string was embedded into the eyeball before

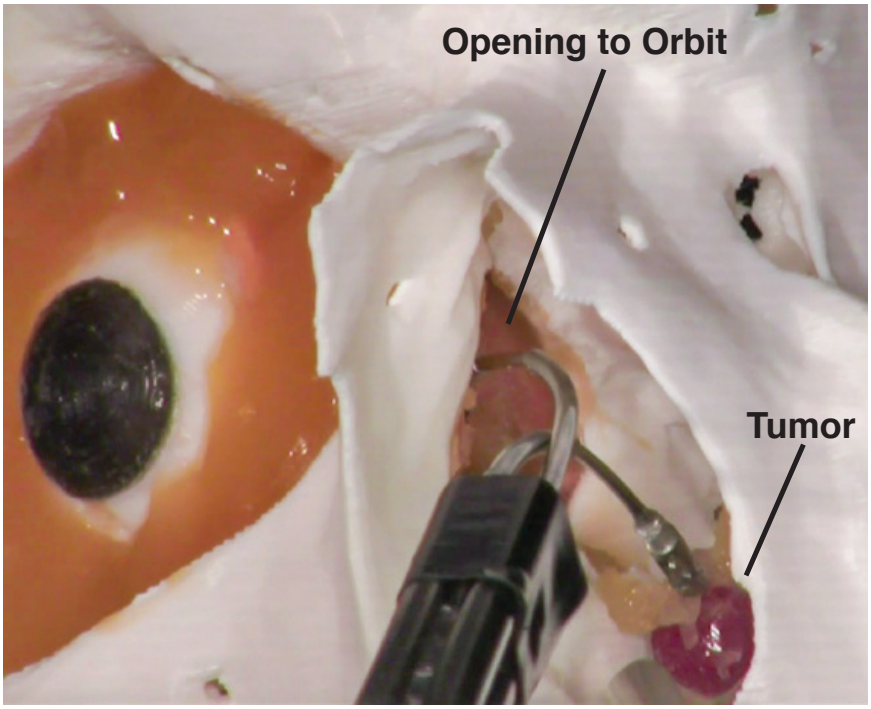

Figure 2.16: Image captured on the operating room camera near the end of a resection experiment, just after the tumor has been pulled from the orbit.

curing, protruding from the back of the eye to represent the optic nerve. The same type of silicone was then used to create the extraocular muscles and a 7 mm spherical tumor, each of which was molded separately. All of these components were placed into the orbit of the skull model, with the tumor situated between the optic nerve and medial rectus extraocular muscle (i.e. the muscle closest to the nasal passage, see Figure 2.18 for a CT scan of the phantom after construction). Finally, a ballistics test medium (SIM-TEST, Corbin Manufacturing & Supply, Inc.) was heated and mixed at a 30% concentration by weight with water, to achieve mechanical properties similar to fat. The SIM-TEST mixture was then injected into the skull around the eye structures to fill the space of the orbit and allowed to set. Each component (eyeball structure, tumor, and skull) was weighed separately during assembly to facilitate measurement of the amount of fat removed during the experiments.

Figure 2.15 shows the experimental setup. A total of ten orbital tumor resections were performed with the robot, with two otolaryngologists performing five resections each. In

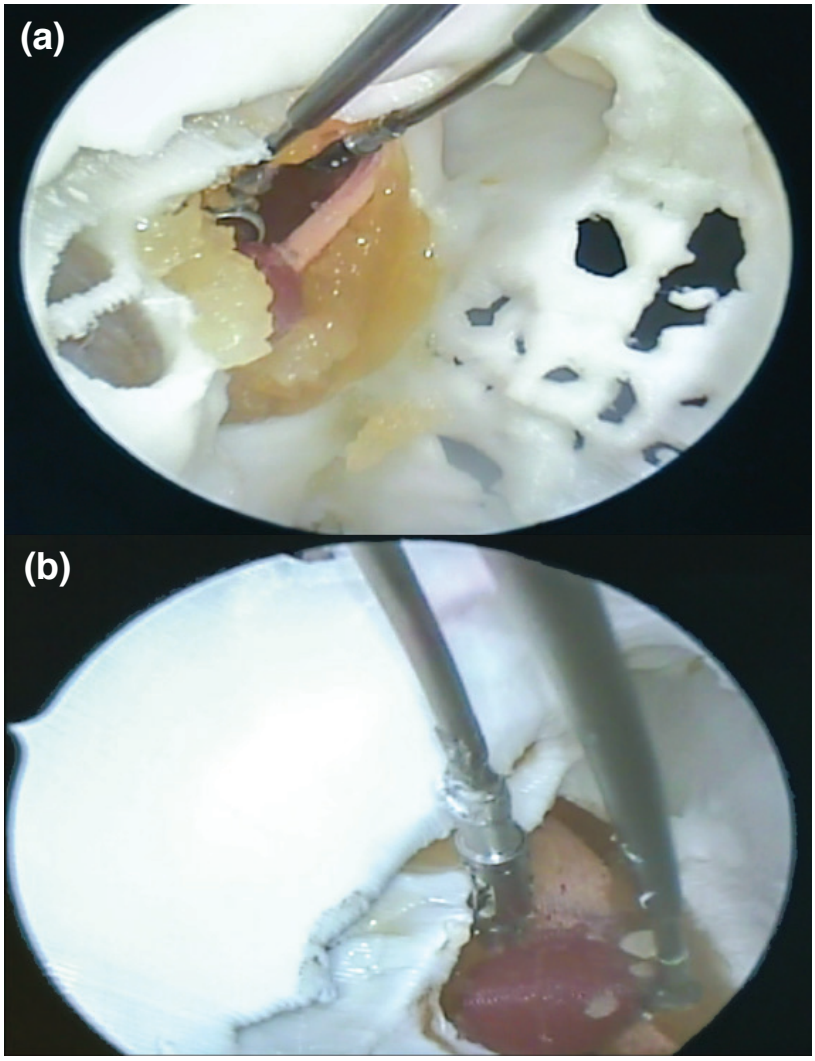

Figure 2.17: Endoscope images captured during resection experiments. (a) The surgeon uses the gripper arm to lift and retract the extraocular muscles and the curette to target the tumor. (b) The surgeon uses both hands cooperatively to manipulate the tumor.

each case, the percentage of fat removed from the phantom during the trial was recorded and measured by weight. Surgeons seek to minimize unnecessary fat removal, as the orbital fat helps to hold the eye in its proper place and provides better cosmetic results. Resection was then carried out with two tools (one gripper and one curette) controlled by two haptic devices, using the foot pedals to clutch in and out of each tool as desired.

All ten resection trials resulted in the successful removal of the tumor without damage to the muscles or optic nerve. The average amount of orbital fat removed by mass was

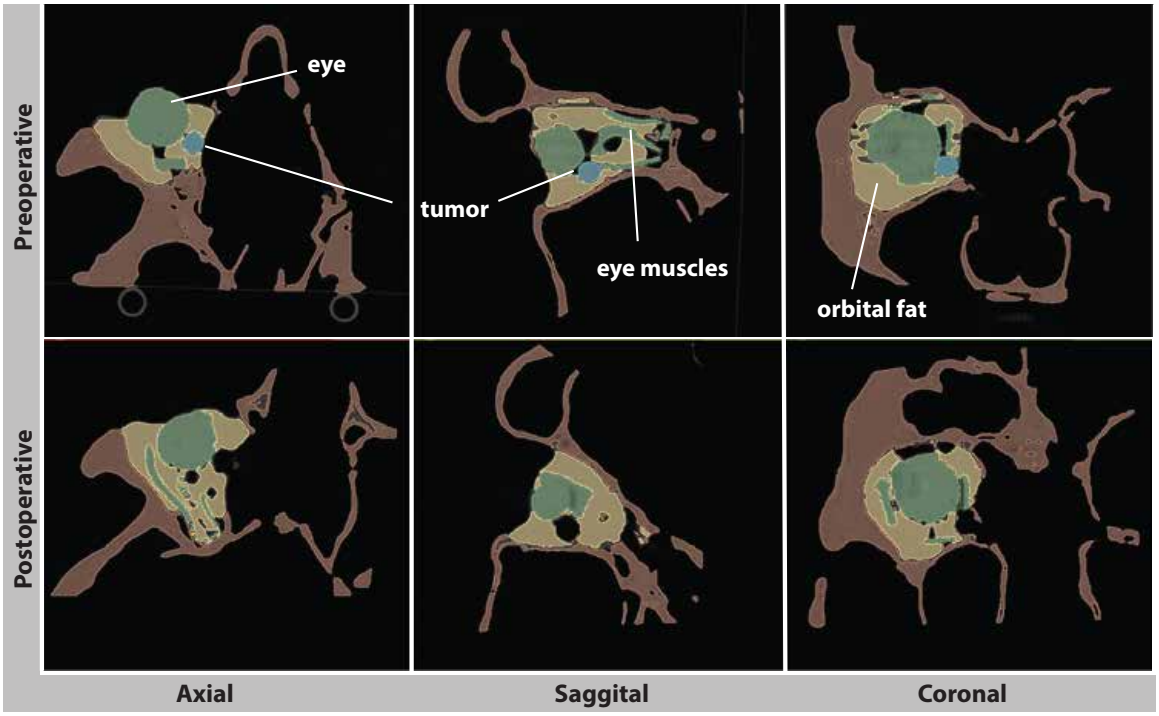

Figure 2.18: Segmented CT scans of preoperative (top row) and postoperative (bottom row) phantom anatomy. The scans illustrate that the tumor was successfully removed without substantial disturbance to the surrounding tissues.

3.9% $\pm$ 2.1% (0.8 g $\pm$ 0.5 g). In each individual case, the level of fat removal was judged to be clinically reasonable for good expected patient outcomes by the participating surgeon. Still images from the endoscope are shown in Figure 2.16 and Figure 2.17. Slices from CT scans of a representative phantom before and after resection are shown in Figure 2.18.

2.7 Discussion

The system described in this chapter and the experimental studies in the preceding section represent promising steps toward enabling transnasal resection of orbital tumors using concentric tube robots. We have demonstrated the ability of the robotic arms, under the control of an expert surgeon, to perform the required manipulation tasks within the geometric constraints of the anatomy. While this is a promising first demonstration of the procedure, there remains much more work to be done. In particular, cadaver studies will

be useful for simulating many of the aspects of this surgery which are difficult to recreate in phantom models, such as the cartilaginous features of the nose and septum. It will also be useful to perform future experiments comparing performance of the procedure with our robot versus with manual hand tools. We suspect our robot will make the procedure easier to perform, but the experiments in this chapter assessed feasibility only, not ease of use.

Along similar lines, the tube precurvatures used in our experiments demonstrate feasibility, but are by no means optimal. Thus, it will be useful in the future to computationally optimize tube shapes for optimal reachability and dexterity. For an example of how computational design optimization can be carried out for a specific clinical procedure see [104].

In addition, incorporating image guidance software that is currently used in the operating room is a useful potential direction for further improving the system. Such navigation software typically involves tracking the tool tips relative to the patient's anatomy using electromagnetic or optical tracking systems along with registration to preoperative imaging. Incorporating electromagnetic sensors into the tips of concentric tube manipulators is one simple way to achieve tracking, and can facilitate integration of existing image guidance methods into our system.

2.8 Conclusion

This chapter presented a new concentric tube robotic system for transnasal surgical procedures. The primary goals with this new system were to take several specific steps from initial proof-of-concept lab systems that have been described in the literature previously, toward a future complete, clinically practical system.

Toward this goal, we integrated a sterile draping concept for non-sterile components, and a complementary cartridge-based tool change approach that facilitates intraoperative instrument swaps. We also designed a new mobile surgeon interface console that is portable and durable, enabling the system to be easily transported between operating rooms. We integrated a variable view-angle endoscope for more adaptable views of the surgical field, and

described custom modular motor control electronics developed for this system. Another system-level advancement was the integration of elastic instability avoidance algorithms for the first time in a physical prototype in a practical application. This facilitated the use of a higher curvature tube set with elastically unstable configurations in its workspace, which would not otherwise have been possible to use safely.

Lastly, we also introduced a new application that has not previously been approached with any surgical robot—the removal of orbital tumors via a transnasal approach. We designed a phantom for orbital cavernous hemangiomas, and demonstrated the ability to remove these phantom tumors using our concentric tube robot system. While there remains much work left, the advancements in this chapter represent several important steps toward bringing concentric tube robots from the academic lab to real-world operating rooms.

Chapter 3

Magnetically Steered Robotic Insertion of Cochlear-Implant Electrode Arrays

3.1 Chapter Overview

Cochlear-implant electrode arrays (EAs) must be inserted accurately and precisely to avoid damaging the delicate anatomical structures of the inner ear. It has previously been shown on the benchtop that using magnetic fields to steer magnet-tipped EAs during insertion reduces insertion forces, which correlate with insertion errors and damage to internal cochlear structures. This chapter presents several advancements toward the goal of deploying magnetic steering of cochlear-implant EAs in the operating room. In particular, we integrate image guidance with patient-specific insertion vectors, we incorporate a new nonmagnetic insertion tool, and we use an electromagnetic source, which provides programmable control over the generated field. The electromagnet is safer than prior permanent-magnet approaches in two ways: it eliminates motion of the field source relative to the patient's head and creates a field-free source in the power-off state. Using this system, we demonstrate system feasibility by magnetically steering EAs into a cadaver cochlea for the first time. We show that magnetic steering decreases average insertion forces, in comparison to manual insertions and to image-guided robotic insertions alone. The manuscript of this chapter was published in the *IEEE Robotics and Automation Letters* [117].

3.2 Introduction

Cochlear implants are among the most successful neuroprosthetic devices, restoring hearing to over 600,000 deaf or partially deaf people worldwide [30, 29]. Traditionally, the cochlear-implant electrode arrays (EAs) are inserted manually into the scala-tympani (ST) chamber of the cochlea [63], with insertion technique varying between surgeons (e.g.,

forces, speeds, angle of approach) [118]. Intracochlear trauma occurs frequently, which impairs residual hearing, increases the stimulation currents required, and results in more crosstalk between electrodes and nerves, reducing implant performance [119, 120].

Reducing trauma has been shown to help preserve residual low-frequency hearing capability and can lead to improved speech perception [121]. Preserving residual hearing is also increasingly important for electroacoustic stimulation strategies, which combine a cochlear implant with an acoustic hearing aid [122, 123]. Trauma reduction can also simplify cochlear revision procedures by reducing the amount of intracochlear ossification and fibrosis [124, 125].

Robotic approaches to EA insertion have been an area of focus for some time, since they offer greater precision in insertion technique, which may lead to less traumatic insertions [126]. Zhang *et al.* developed a direct kinematics calibration method using mechanics-based models [48], and showed that variability can be decreased using robot-assisted insertion and optimized path planning, and that robots enable insertion speed and other desired parameter values to be more easily reproduced [52]. Pile *et al.* developed a parallel robot with three degrees of freedom (DOF) to insert precurved arrays using the advance-off-stylet technique [45]. They showed that the robot could maintain insertion forces below 80 mN in a cochlea phantom throughout the insertion and confirmed many of the aforementioned benefits of a robotic insertion approach. Pile *et al.* also provided workspace and parameter requirements for robotic insertion. Image guidance approaches have been shown to decrease the invasiveness of the surgical procedure and provide an optimal insertion vector for array placement [47, 127]. In particular, Caversaccio *et al.* clinically demonstrated a safe and effective robotic approach for drilling a direct access tunnel to the cochlea [127]. These works demonstrate the benefits of automation in cochlear implant surgery and motivate developing an automated tool that enables the surgeon to automatically insert the EA along the optimally planned trajectory, in a clinical setting.

Prior EA insertion tools have used a variety of innovative mechanisms of gripping and

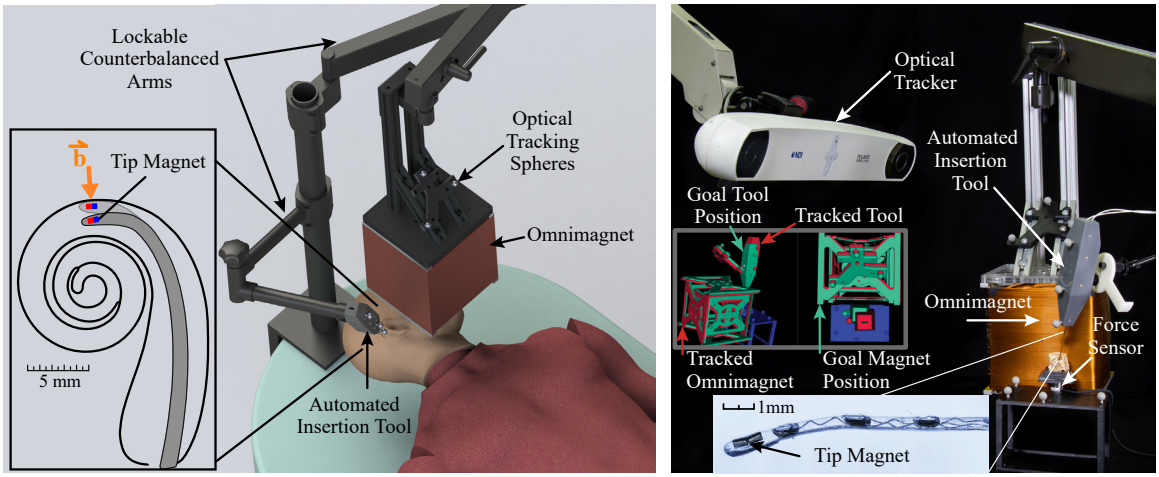

(a) System Concept (b) Experimental Setup

Figure 3.1: System for magnetically steered robotic insertion of cochlear-implant EAs. The automated insertion tool and Omnimagnet are both optically tracked and secured on counterbalanced positioning arms. The surgeon loads the EA into the tool and uses image guidance to align the tool and Omnimagnet with the preoperatively planned poses, at which point the arms are locked in place and the planned magnetically steered insertion trajectory is accomplished.

carrying EAs along the desired path. These methods include: utilizing a blunt pin and linear motion through a slotted tube [128, 129], using two titanium tube halves and manually inserting the array [127], using a gripper with two arms rotating around a pivot point to grasp the array [51, 46, 130], and utilizing a collet-style gripper and a parallel robot to guide array insertion [45].

Going beyond robotic insertion, steering (i.e., bending of the EA tip) has the potential to further reduce intracochlear trauma by reducing forces between the EA and the ST walls and avoiding tip impingement. Steering may also enable deeper insertions, which may enable the patient to perceive lower-frequency sounds than would otherwise be possible [131]. An EA steering method, developed by our group, utilizes a magnetic field source adjacent to the patient's head to steer a magnet-tipped EA inside of the ST and reduce insertion forces. This concept was first introduced in [70], where a benchtop system used a permanent magnet—which could be rotated with one DOF to change the applied-field direction, and translated with one DOF to change the applied-field strength—to steer a 3:1

scaled EA-like device in a 3:1 scaled ST phantom. A similar system was later evaluated using commercially available EAs with a magnet embedded in the tip [58], inserted into improved 1:1 scale ST phantoms [132], where a significant decrease in insertion forces was reported compared to robotic insertion without magnetic steering.

This chapter presents a complete system (see Fig. 3.1) that represents the culmination of prior work by our group on subsystems and algorithms [70, 133, 132, 58, 134, 71, 72, 135] for magnetically steered robotic insertion of EAs. The goal of the current system is to bridge the gap between the benchtop and practical animal and cadaver experiments. Specific new contributions in this chapter include: 1) introducing the first fully nonmagnetic automated insertion tool, with a novel slotted-tube approach to controllably release tapered flexible EAs after insertion, 2) incorporating silhouette-based image guidance for practical, accurate insertion-tool and magnet alignment to a preoperative plan in the operating room, which has never before been described in an archival publication, 3) replacing the moving permanent-magnet field source with a safer, stationary Omnimagnet [136] electromagnetic source, 4) introducing a stronger, cubic-core Omnimagnet, and 5) the first demonstration of magnetically steering an EA in a cadaveric specimen, verifying that force reductions shown previously in phantom models translate to the cadaver setting.

3.3 System Hardware and Workflow

An overview of the robotic system is shown in Fig. 3.1. A basic overview of the workflow with the proposed system is as follows. We first generate a patient-specific plan using the patient's preoperative computed-tomography (CT) scan. This preoperative plan includes 1) generating an optimal insertion vector and corresponding insertion-tool pose (position and orientation), 2) calculating the Omnimagnet pose that corresponds to the plan, and 3) registering the planned magnetic field vectors to the individual's ST (and the corresponding Omnimagnet coil currents to produce these vectors). Using this preoperatively generated plan, the surgeon will manually align the counterbalanced automated insertion

tool and the counterbalanced Omnimagnet, and lock them in place. Both devices are optically tracked, enabling users to precisely align them using a custom image-guidance extension in 3D Slicer [114, 137]. The surgeon will then simply hold a button to run the prescribed trajectory that synchronously coordinates insertion depth and magnetic field to produce a smooth, atraumatic insertion. When insertion is complete, the Omnimagnet is powered off and the insertion tool is removed. The Omnimagnet, insertion tool, and force sensor interface with one another using custom Robot Operating System (ROS) nodes [95]. In the following sections, we describe the system components including the Omnimagnet and the new automated insertion tool for EA advancement and deployment.

3.3.1 Omnimagnet

Magnetically steering the EA through the spiral-shaped cochlea requires strong, controllable magnetic fields. Our prior work has exclusively considered a permanent magnet as the field source [70, 58]. However, as noted in [134], it may be desirable to use an electromagnetic source for three reasons: First, an electromagnet has a controllable magnetic dipole, meaning that it does not need to be physically moved during EA insertion to vary the field strength at the cochlea, eliminating any potential risk of collision with the patient or other objects. Second, an electromagnet can be turned off and is inert when not in use, making handling, storage, and use of ferrous surgical equipment safer. Third, the relatively short duration of a surgical EA insertion (less than 30 seconds) would allow high levels of current to be sourced through the coils without reaching unsafe temperatures.

In the system presented in this chapter, we have replaced the permanent-magnet source with an Omnimagnet electromagnetic source [136]. An Omnimagnet comprises three nested orthogonal coils and a ferromagnetic core. Three control inputs (the current in each coil) provide control of the magnetic dipole of this magnetic field source, which can be used to generate a desired magnetic field vector $\boldsymbol{B}$ at an arbitrary location in space. In the original conception of the Omnimagnet [136], and all prior embodiments, the fer-

romagnetic core was spherical. In this chapter, we re-optimized the Omnimagnet for a cubic core, which has the effect of increasing the achievable dipole strength by approximately 35% for a given overall package size and current density. Our prototype cubic-core Omnimagnet has overall cubic dimension of approximately 200 mm, with a ferromagnetic cubic core of dimension 102 mm, with the dimensions of the individual coils (and their electrical resistances) provided in Table 3.1. The Omnimagnet uses 16 AWG square-cross-section copper magnet wire (MWS Precision Wire Industries, Westlake Village, CA). Our final prototype is 22 kg, which is passively supported by a lockable counterbalanced arm (Dectron, Wilsonville, OR).

As described in [136], the control equation for an Omnimagnet, assuming a basic dipole model, is

$$\boldsymbol{I} = \frac{2\pi}{\mu_0} \|\boldsymbol{p}\|^3 \mathbb{M}^{-1} (3\hat{\boldsymbol{p}}\hat{\boldsymbol{p}}^T - 2\mathbb{I}) \boldsymbol{B}. \tag{3.1}$$

where $\boldsymbol{I}$ (units A) is the 3×1 array of coil currents, $\boldsymbol{p}$ (units m) is the vector from the center of the Omnimagnet to the desired point in space at which a desired magnetic field vector $\boldsymbol{B}$ (units T) is to be generated, $\mathbb{M}$ is a linear transformation that maps the current array $\boldsymbol{I}$ to the Omnimagnet's dipole moment $\boldsymbol{m}$ (units $\mathrm{A \cdot m^2}$), $\hat{\boldsymbol{p}} \equiv \boldsymbol{p}/\|\boldsymbol{p}\|$, $\mu_0 = 4\pi \times 10^{-7}\ \mathrm{T \cdot m \cdot A^{-1}}$ is the permeability of free space, and $\mathbb{I}$ is the 3×3 identity matrix.

To utilize the Omnimagnet, a high-voltage DC supply powers three servo drive amplifiers (ADVANCED Motion Controls, Camarillo, CA), which regulate the current through each coil of the Omnimagnet. The amount of current is set via analog inputs (± 10 V). Custom control boards receive commands over Ethernet from our custom ROS nodes and generate the required analog voltage signals for each servo drive. To determine the current scaling for each coil, a certified calibrated 3-axis magnetic field sensor (3MTS, Senis, Zug, Switzerland) was used to experimentally measure the magnetic field and compare to (3.1).

As an additional layer of safety, we have implemented a dedicated microcontroller to monitor thermocouples embedded throughout the Omnimagnet, which shuts off the amplifiers if predefined temperature thresholds are exceeded. This microcontroller also monitors

Table 3.1: Properties of the Omnimagnet coils, including axial length (L), inner width (W), thickness (T), and resistance (R)

	L (mm)	W (mm)	T (mm)	R (Ω)
Inner Coil	117	105	11.2	3.5
Middle Coil	140	128	8.4	3.8
Outer Coil	154	152	6.9	4.0

the temperature between insertion trials, which enables us to verify that the Omnimagnet has sufficiently cooled down before running another experiment.

It is important to address the safety of placing the Omnimagnet (or any strong magnetic source) near the patient's head. Strong magnetic fields are commonly used in medical diagnosis and treatment, such as Magnetic Resonance Imaging (MRI) and Transcranial Magnetic Stimulation (TMS), and a wide variety of magnetically driven medical devices have been developed [138, 139]. Safety limits for magnetic fields are based on the nature of the magnetic field, which is typically classified as: static fields, time-varying gradient fields (100 to 1000 Hz), and radiofrequency (RF) fields (10 to 100 MHz) [140, 141, 142]. According to the FDA's Criteria for Significant Risk Investigations of Magnetic Resonance Diagnostic Devices (2014), a static field producing less than 8 T is considered a nonsignificant risk in adults and children over the age of one month. Other sources specify that static field exposure to the head should be limited to 2 T to ensure patient comfort [140, 141]. Our research in magnetic steering of EAs currently utilizes quasistatic fields of less than 100 mT, which is well below the safety limits imposed by the FDA, or recommended by other researchers. Therefore, it does not seem that the magnitude or rate of change of the magnetic fields used in magnetic steering of EAs poses any significant risk to a patient.

3.3.2 A New Insertion Tool Compatible with Magnetic Steering

Deploying an EA in the presence of strong magnetic fields presents unique constraints not encountered by previous designs of clinically-viable automated insertion tools: the

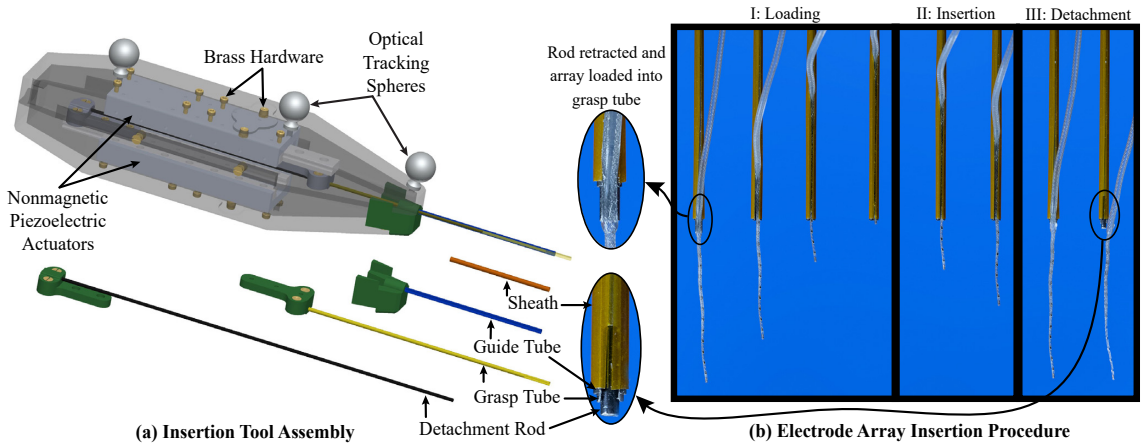

Figure 3.2: (a) Insertion tool assembly. The inner detachment rod and middle grasp tube are each attached to an actuator. The outer guide tube is connected to a detachable tip piece so that if an EA of a different diameter is to be used, it can simply be replaced with a tube of a different diameter. (b) Diagram showing tube operation for EA deployment. Step I: Loading- Load EA into the grasp tube slot and retract until the tip of the EA reaches the guide tube opening. Step II: Insertion- Insert EA by advancing the grasp tube and detachment rod simultaneously. The polyimide sheath constrains the tapered end of the EA during deployment. Step III: Detachment- Retract the grasp tube over the stationary detachment rod, which gently releases the EA from the grasp tube.

insertion tool must not contain ferromagnetic components, and to be used clinically the insertion tool has to hold, push, and release the implant gently and controllably. To achieve both of these specifications, we designed a new insertion tool and a new grasping mechanism to interface with the EA (Fig. 3.2). The tool is constructed from a 3D printed plastic housing (Formlabs, Somerville, Massachusetts), two piezoelectric linear actuators (SLC-1770-L-E-NM, SmarAct, Oldenburg, Germany), Nitinol tubes/rods, and brass fasteners. Three spherical, retroreflective markers are attached to the body of the tool to create a rigid body for optical tracking.

Details of the insertion tool assembly can be viewed in Fig. 3.2(a). Tube parameters were chosen to accommodate the dimensions of the FLEX28 EA (MED-EL, Innsbruck, Austria), but can be easily adapted for use with other EAs. The distal end of the tool consists of three nested Nitinol tubes and rods, and an outer polyimide sheath. The innermost Nitinol rod assists with EA detachment and is attached to a linear actuator. The middle

Nitinol tube has an approximately 10-mm-long slot for grasping the EA, and is attached to another linear actuator. The outer Nitinol tube has a slot spanning the length of the tube and serves as a guide for the EA during deployment. Finally, a polyimide sheath with a lengthwise slit surrounds the outermost Nitinol tube to constrain the thinner, tapered region of the FLEX28 (which tapers to a tip diameter that is less than half that of the proximal end) and to keep the much thinner tip of the flexible EA concentric with the proximal end. The absolute insertion depth limit of the tool is 46 mm, enabling insertion of the longest EAs currently available (the FLEXSOFT and Standard EAs by MED-EL are 31.5 mm long [143]). EA insertion proceeds as described in Fig. 3.2(b).

3.4 Image Guidance and Patient-Specific Paths

In this section, we describe the preoperative steps for generating a magnetically steered insertion plan. We incorporate the state-of-the-art insertion trajectory algorithm to generate the planned patient-specific insertion vector, and then develop a methodology to automatically generate a full magnetic steering plan given only the patient-specific anatomy and insertion vector. Outputs of this automated planning are the aligned Omnimagnet and insertion tool position and orientation (patient-specific), as well as the magnetic field vectors along the ST (using an average cochlea model registered to the patient's ST).

3.4.1 Patient-Specific Insertion Planning

Our image-guided workflow begins by acquiring a preoperative CT scan. We then segment the inner-ear anatomy using the atlas-based approach of [71] and compute the optimal insertion vector as described in [72] (see Fig. 3.3). This angle and position defines the alignment of the automated insertion tool. This atlas-based segmentation has been used to segment in-vivo clinical CT scans with a mean surface error of 0.21 mm [144].

Our steering method works by creating a magnetic field vector that is orthogonal to the insertion path at the current location of the magnetic tip of the EA, as depicted in the inset

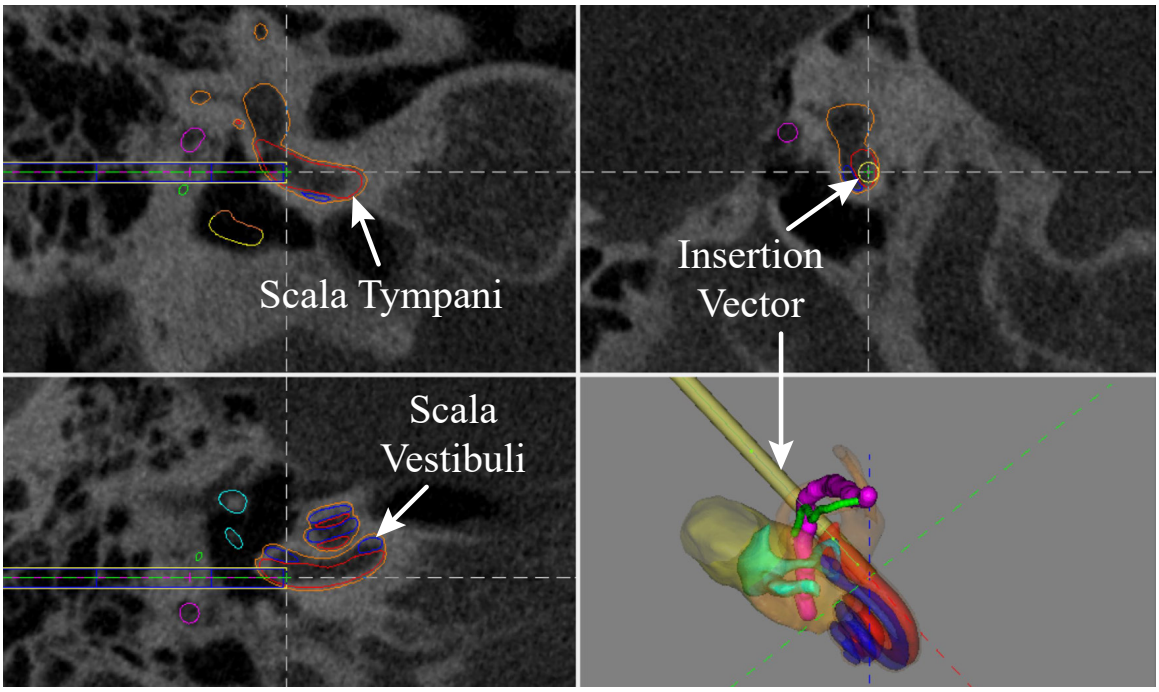

Figure 3.3: Patient-specific segmentation of cochlear anatomy and automatically generated insertion vector (yellow) [144, 71, 145]

.

of Fig. 3.1(a). This is done in order to create a torque on the embedded magnet, to cause bending in the continuum body of the EA, and thus reduce the normal force on the ST wall. Depending on the orientation of the magnet, some force will also be applied. However, even the worst-case orientation (i.e., tip magnet aligned with magnetic field gradient) results in a magnetic force of less than 100 µN. We generate this path using the equations in [132] that describe an average ST model based on anatomical data. We then register our magnetic field path to the medial axis segmented from the patient's ST.

Finally, using the shape of the experimentally determined field magnitudes in [58], we prescribe the magnetic field magnitudes to increase in a ramp-like manner (see Fig. 3.4). The field is zero during the initial linear portion of insertion, when there is no need for bending. Upon reaching the basal turn of the cochlea, the magnetic field turns on. As the EA is inserted deeper, and the ST curvature increases, the field ramps up to apply a larger moment to the tip of the EA. The field eventually saturates at the maximum power output

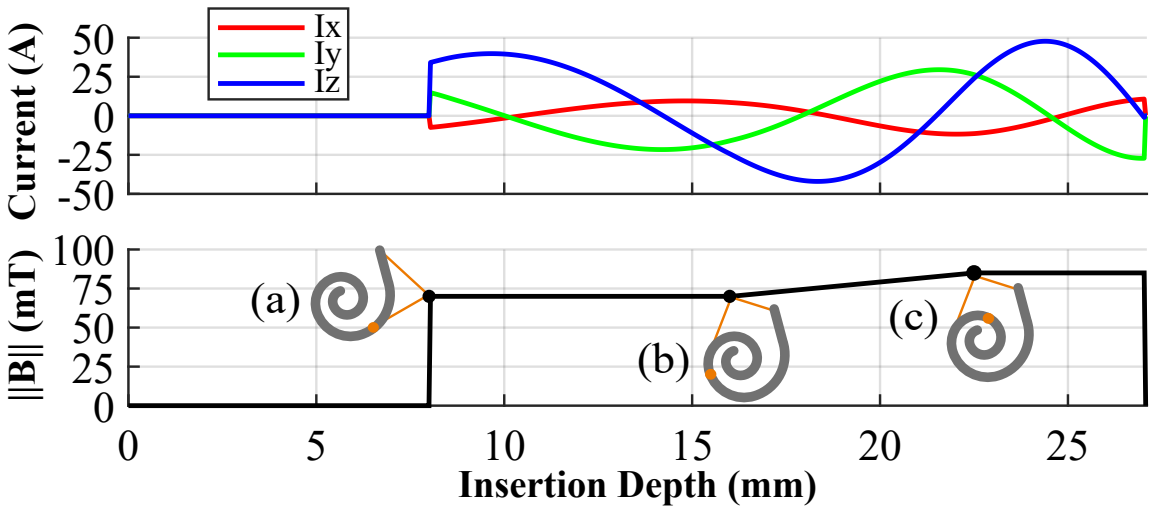

Figure 3.4: Preoperative plans for magnetic steering specify (top) the Omnimagnet coil currents required to generate (bottom) the prescribed magnetic field magnitudes based on (a) turning on the field after the initial straight insertion, then (b) ramping up the magnetic field magnitude as the ST curvature increases, until (c) saturating at the maximum power.

of the electrical system.

3.4.2 Image Guidance

Using 3D Slicer, OpenIGTLink, and the Plus Server App [114, 137], we developed a custom GUI extension (see screenshot in Fig. 3.1(b)) that connects to the NDI Polaris Spectra optical tracker (Northern Digital Instruments, Ontario, Canada), which tracks and displays the movement of the insertion tool, Omnimagnet, and cochlea fixture in real time. This software functions using the same methodology in [135] but with different hardware and software implementation. The program guides the user to the correctly aligned tool pose determined in Sec. 3.4.1 by displaying the real-time position of the object (shown in red in the screenshot on Fig. 3.1(b)) to the desired pose (shown in a green in the screenshot of Fig. 3.1(b)). The user then manually manipulates each device until the tracked pose and desired pose are aligned, at which point the user locks the device in place.

Table 3.2: Experimental Conditions

Method	Robotic Insertion	Image-Guided Alignment	Magnetic Steering
Manual	No	No	No
Robotic	Yes	Yes	No
Robotic & Magnetic Steering	Yes	Yes	Yes

3.5 Experimental Methods

3.5.1 Phantom Experiments

We conducted proof-of-concept experiments in the phantom model developed in [132], which is useful because it is transparent and enables one to view the motion of the EA during insertion. Four insertions were performed using our robotic system and proposed workflow. To ensure that magnetic steering provided unique benefits in terms of reaction forces beyond those derived from robotic insertion alone, we performed experiments as follows: 1) unaided manual insertions by an experienced surgeon, 2) robotic insertions using the new insertion tool described in Section 3.3.2, with image-guided pre-insertion alignment but no magnetic steering, and 3) robotic insertions with image guidance and magnetic steering. Table 3.2 shows a summary of these cases.

A 3D-printed ST phantom with a 1.2 mm cochleostomy opening (Fig. 3.5, see [132] for details) was secured into a fixture with cyanoacrylate. This fixture was then mounted to a Nano17 Titanium force/torque transducer (ATI Industrial Automation, Apex, NC) attached to a frame with optical fiducial markers. A CT scan of this assembly was then acquired. As described in Sec. 3.4, the preoperative scan was used to generate the insertion plan.

We filled the phantom with 0.9% saline solution before each insertion as in [58]. For manual insertions, a surgeon performed four unaided insertions with a new, unmodified FLEX28 EA, using the standard forceps that are used clinically for inserting EAs (see Fig. 3.6). In cases of robotic insertion, both with and without magnetic steering, a magnet-

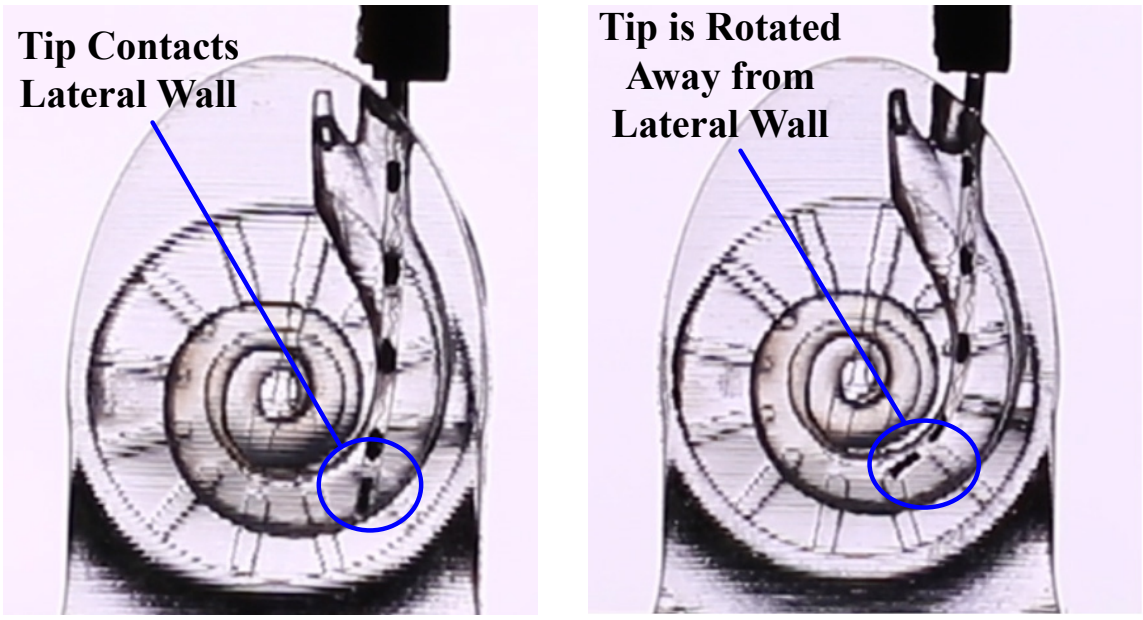

Figure 3.5: Robotic insertion into a phantom (a) without and (b) with magnetic steering. The tip of the EA is torqued away from the lateral wall in the magnetically steered case, lowering the contact force of the EA with the wall.

tipped FLEX28 EA was used. All magnet-tipped EAs were fabricated by MED-EL and include two cylindrical axially magnetized magnets (each 0.25 mm in diameter by 0.41 mm in length) embedded in silicone at the tip of the array (see inset of Fig. 3.1(b)). The EA was loaded into the insertion tool, and the Omnimagnet and insertion tool were aligned using image guidance according to the prescribed preoperative plan, with a maximum angular alignment error of less than 1°. The support arms were locked in place and the final poses of the tool and magnet were recorded. The insertion tool then deployed the EA at a constant velocity of 1.25 mm/s (this velocity was selected in view of a 0.5–3 mm/s range in the literature [63]).

The final insertion method followed the same procedure as robotic insertion described above, but also used magnetic steering during insertion. The magnetic field of the Omnimagnet was updated at a rate of 80 Hz. Four insertions with a robotic approach and four insertions with a robotic approach and magnetic steering were completed using the same

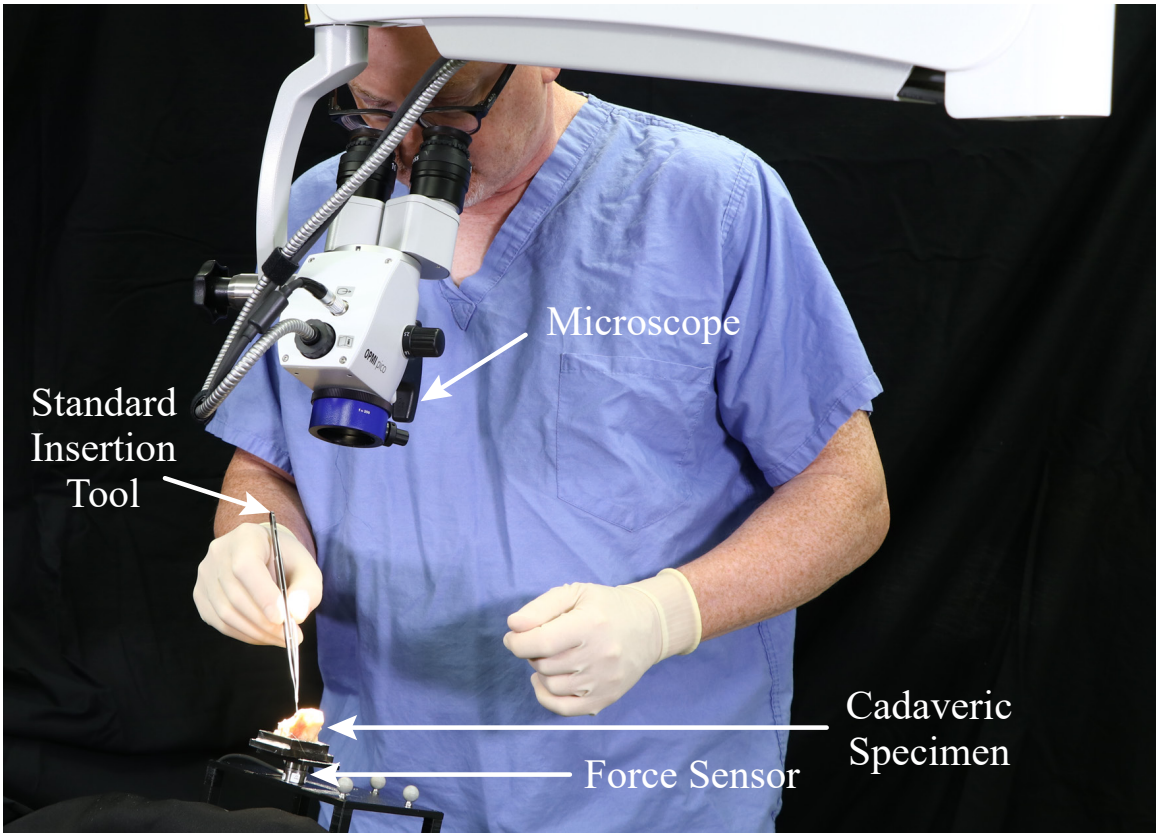

Figure 3.6: A surgeon performing a traditional EA insertion, shown here with the cadaveric cochlea.

magnet-tipped EA, alternating between using magnetic steering and robotic insertion alone. For all insertions, force measurements were acquired at a rate of 50 Hz. Since the EA tip could be visualized through the transparent phantom in these experiments, forces could be mapped to angular insertion depths using video collected during insertion at 60 fps.

3.5.2 Cadaver Experiments

The same three experimental methods used in the phantom experiments (see Table 3.2) were also conducted with a formalin-fixed cadaver cochlea. The cochlea was secured in a fixture using paraffin wax and hot-melt adhesive. A patient-specific insertion plan was generated in the same manner previously described. Unaided manual insertions were performed by an experienced surgeon with a new, unmodified FLEX28 EA (see Fig. 3.6). For

image-guided robotic insertions, the automated insertion tool was aligned with a maximum angular alignment error of less than 2°. A second magnet-tipped FLEX28 EA was used to perform robotic insertion experiments, alternating between robotic insertion alone and robotic insertion combined with magnetic steering (a first-of-its-kind experiment). Workflow proceeded identically to the phantom experiments, with three insertions performed using each method. A force threshold of 125 mN was enforced during robotic insertions (i.e. Omnimagnet and insertion tool disabled if threshold was exceeded). After insertion, the EA was released from the insertion tool as described in Sec. 3.3.2 and a postoperative CT scan was acquired.

3.6 Results

A comparison of the first contact point with the lateral wall of the ST with and without magnetic steering is shown in Fig. 3.5; this result is qualitatively consistent with the results of [58]. Mean insertion force magnitudes, $\|F\| = \sqrt{F_x^2 + F_y^2 + F_z^2}$, and the difference, $\Delta\|F\|$, in insertion forces for both phantom and cadaver experiments are shown in Fig. 3.7, where the shaded region around each curve indicates one standard deviation from the mean. In each case, force samples were grouped into bins and then samples within each bin were averaged. A bin of 3° was used for phantom experiments and a bin of 0.125 mm was used for cadaver experiments (since there was no direct visualization of angular depths during insertion). Diamonds mark the final depths of each individual insertion. For robotic methods this was defined as when the force increased 35 mN or more over 1 mm of actuator travel (indicative of EA buckling); for manual insertions it was at the surgeon's discretion. A one-tailed *t*-test analysis (as detailed in [58]) was performed, and the depths where the null hypothesis can be rejected with 95% confidence (i.e., statistically significant force reduction) are indicated with rings. All force reductions observed after the magnetic field was turned on (approximately 140° for phantom insertions, 8.0 mm for cadaver insertions) were statistically significant. Compared to robotic insertion alone, magnetic steering re-

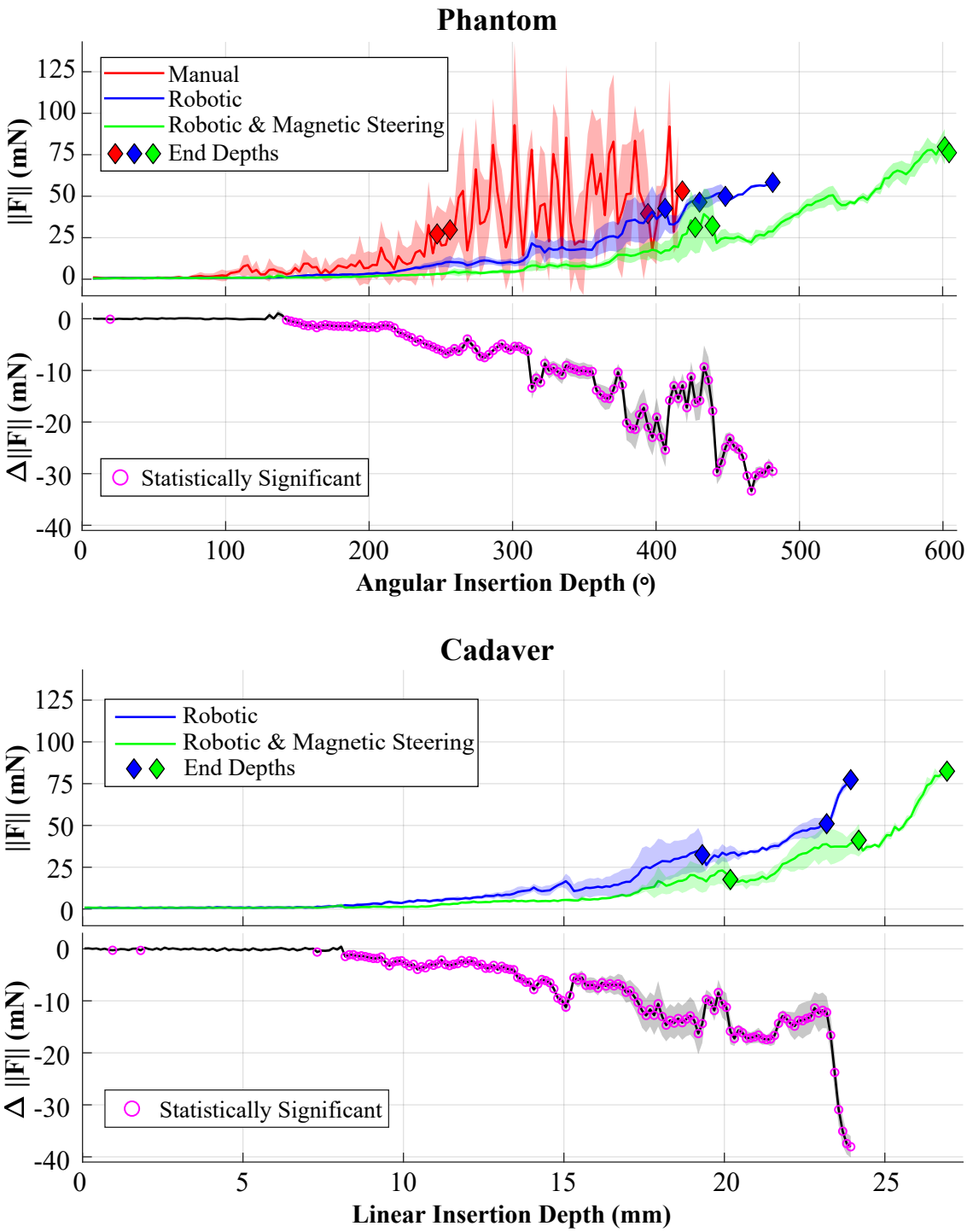

Figure 3.7: (Top) Mean insertion forces with respect to angular insertion depth for phantom experiments and linear insertion depth for cadaver experiments, illustrating that magnetic steering achieves forces that are typically lower than for robotic insertion alone. Shaded regions indicates ± 1 standard deviation from the mean. Diamonds mark the final depth of each individual insertion. (Bottom) Difference in force, ΔF, between robotic insertion and magnetically steered robotic insertion. Magenta rings indicate a statistically significant decrease in force between the two methods.

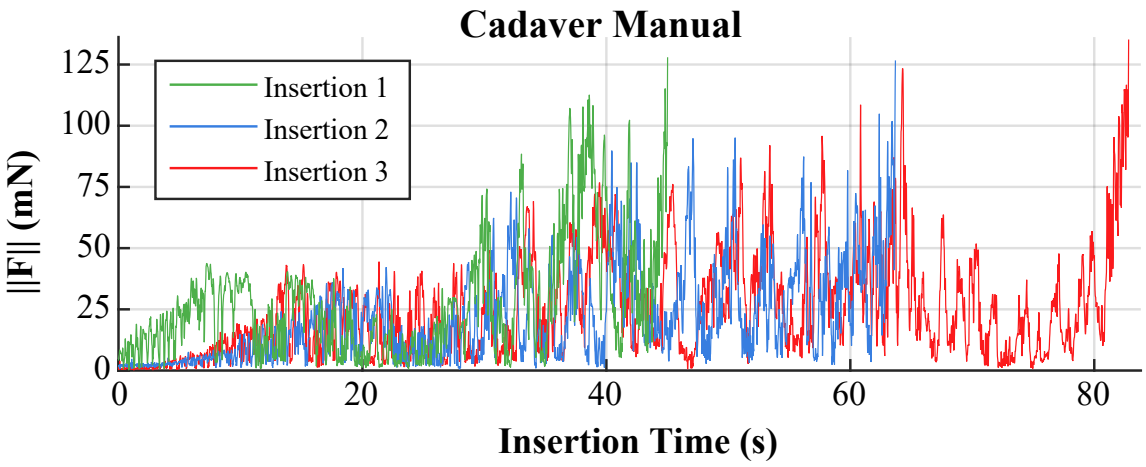

Figure 3.8: Forces observed during manual cadaver insertions exhibited more variability and larger, more frequent spikes compared to robotic methods.

duced forces by an average of 53.8% during phantom insertions and 48.8% during cadaver insertions.

The forces recorded during manual insertions in cadaver are shown in Fig. 3.8. Note that the force data for the manual cadaver insertions is plotted vs. time since the surgeon is inserting into opaque bone, and there are no actuators to give position information in real-time.

Fig. 3.9 shows the average final angular insertion depths for each type of phantom and cadaver insertion. For phantom experiments, we see that the inclusion of magnetic steering resulted in deeper insertions on average compared to robotic-only or manual insertions. The average angular insertion depth for the manual insertions in cadavers was slightly higher than that of the other methods. Note that a force threshold cutoff was not enforced in these manual insertions.

The maximum temperature rise observed for the inner, middle, and outer Omnimagnet coils was 1.6°C, 10°C, and 34°C, respectively. These values are all within the Omnimagnet's operating range. It is also important to note that the Omnimagnet is never in direct contact with the patient, and is moved away after EA insertion is complete.

In summary, in both phantom and cadaver experiments, robotic insertions were smoother

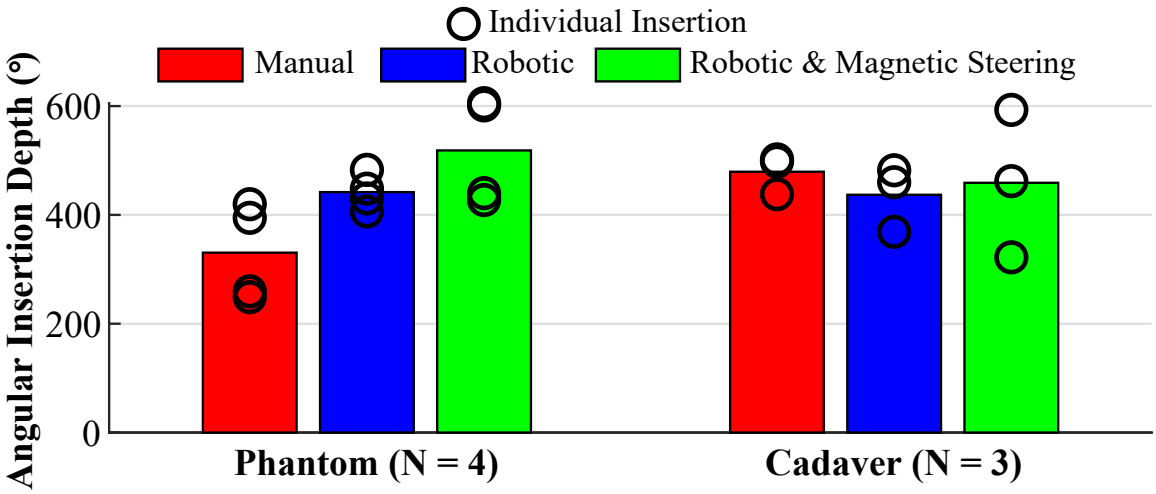

Figure 3.9: Comparison of the average final angular insertion depths for each insertion method. Depths of individual insertions are shown as black rings.

(with fewer force spikes) than the manual insertions, and magnetic steering significantly reduced forces with respect to robotic insertion alone.

3.7 Toward Clinical Deployment

The system described in the chapter was designed to be used in experiments with live guinea pigs, and will have to be scaled up (approximately 30%) to be used as a clinical system with living humans. This is due to the increased distance between the cochlea and the applied dipole. In [134], we found the optimal placement and size of a spherical NdFeB permanent magnet (i.e., an ideal dipole-field source), based upon the magnetic field values suggested in [58] for the same embedded EA tip magnets used here. We can use this result to design an equivalent-strength (measured at the location of the cochlea) Omnimagnet. Alternatively or in addition, since the Omnimagnet can be oriented such that only two coils are required, simply removing the outermost coil and enlarging the other two would enable an increase in strength that is independent of any increase in overall size.

Note also that the magnetic torque that can be generated on the magnet-tipped EA is a product of the applied field magnitude and the strength of the permanent-magnet em-

bedded in the tip of the EA (which is proportional to its volume). When we consider that volume scales cubically with length, we conclude that substantial increases in torque can be achieved with even modest increases in the size of the embedded magnet, which are possible, since the magnets used in this chapter took up less than 40% of the cross-sectional area of the EA's tip. Such an increase may preclude the need for any size increase of the Omnimagnet.

We performed a conservative sensitivity analysis to registration errors of the dipole-field source (i.e., the Omnimagnet) with respect to the cochlea. We expect a worst-case 3.2% error in field magnitude and 1.7° error in field direction due to a 1 mm error in Omnimagnet position. We expect a worst-case 1.3% error in field magnitude and 2.0° error in field direction due to a 1° error in the Omnimagnet dipole $\boldsymbol{m}$. These values should be insensitive to changes in the size of the field source.

However, we also found that the dipole model used in (3.1) has non-negligible error in the region of interest. In the future, a calibrated model that includes the first three terms of the magnetic-field expansion (the dipole term being the first) could be used to reduce the modeling error to less than 1%[146]. Measuring the electrode position in real-time is challenging because many of the traditional sensing methods used in robotics (e.g., EM/optical tracking) either require line of sight, lack the necessary accuracy, or are too large to integrate. Future work could incorporate novel sensing methods to enable closed-loop control.

3.8 Conclusion

We have presented a new robotic system to improve cochlear implant EA insertion. The primary goal of this system was to build upon prior benchtop proof-of-concept magnetic steering systems and transition toward a more clinically-focused design. We developed a workflow for utilizing preoperative imaging to compute patient-specific insertion vectors and a magnetic guidance plan. Patient safety was improved by replacing an actuated

permanent magnet with a static electromagnet. We also introduced the first nonmagnetic automated insertion tool, which is capable of deploying and releasing clinical EAs with a new set of tubes that accommodates tapered arrays and gently releases the implant after deployment. Accurate pre-insertion alignment of the insertion tool was achieved by incorporating image-guidance software paired with an optical tracking system. We experimentally validated the system by performing magnetically steered robotic insertions in a ST phantom and a first-of-its-kind magnetically steered robotic insertion into a cadaveric cochlea, demonstrating in both cases that magnetic steering lowers forces by approximately 50% compared to robotic insertion alone.

Chapter 4

Impedance Sensing Method for Real-time Localization of Cochlear-Implant Electrode Arrays

4.1 Overview

Beneficial hearing outcomes resulting from cochlear implant surgery are contingent on the careful and precise placement of the electrode array. Unfortunately, surgeons are essentially blind while inserting the array, relying on experience and the detection of barely perceptible forces. The small, helical shape of the cochlea precludes the use of most sensing modalities. However, recent investigations into using electrical impedance measurements for position sensing have shown potential. In this chapter, we extend this prior work and introduce a method for producing direct, real-time estimates of electrode array location from bipolar impedance measurements and perform validation experiments in a scala tympani phantom. We also present the first ex vivo studies demonstrating how impedance measurements can improve electrode array placement.

4.2 Introduction

Thirty years ago, less than 10,000 people had received a cochlear implant (CI); today, there are more than 600,000 recipients worldwide [29, 30]. We have witnessed tremendous progress in those three decades. In 2008, there was a call for more difficult tests of sentence intelligibility due to 28% of patients achieving a perfect score on one standard test [147]. As CI programming strategies continue to become more sophisticated, a simultaneous focus has been placed on reducing trauma caused during insertion of the electrode array.

The most common trauma is damage to the thin, delicate basilar membrane separating the scala tympani from the scala vestibuli. Translocation of the electrode array into

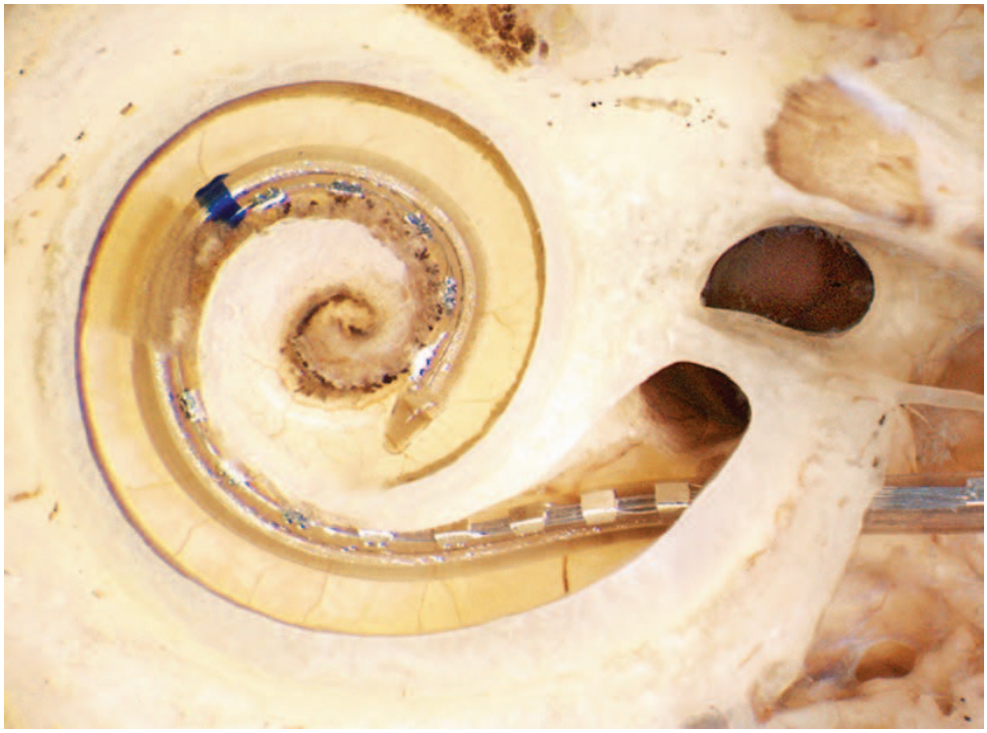

Figure 4.1: Example of an optimal insertion of a perimodiolar electrode array. The electrodes lie along the modiolus where they are closest to the spiral ganglion neurons. (Reproduced from [150] by permission from Springer Nature: Cochlear Anatomy via Microdissection with Clinical Implications, ©2018)

the scala vestibuli occurs in 25-33% of cases, resulting in the patient losing any residual hearing [38, 39]. Even if trauma is minimized and the electrode array is placed in an undamaged scala tympani, CI performance is still highly variable [40]. The interface between the electrodes and auditory nerve endings they stimulate is crucial to optimal cochlea function and pitch perception [148]. This optimal configuration consists of placing the electrode array such that each electrode pad is in contact with the neural endings it stimulates [149], i.e. coiled along the modiolus with the electrode pads pointing inward toward the dense network of spiral ganglion neurons [42, 67] (see Fig. 4.1). Any distance between these electrodes and the neural endings they stimulate results in a higher current threshold for stimulation, increased electrode interaction (cross-talk), and less focal stimulation of spiral ganglion cells [120]. Unfortunately, it is not straightforward how to determine this electrode-modiolar distance intraoperatively to enable surgeons to make adjustments

during insertion.

The narrow, helical shape of the cochlea cannot be imaged via external (no line-of-sight) or internal (too small) cameras. Magnetic tracking coils are too large to fit alongside the electrode array. Custom electrode arrays have been designed which incorporated strain gauges [59, 60] or scanning electron microscopy [61] for position sensing, but integrating sensors into existing electrode arrays is not currently feasible. Atlas-based segmentation of computed tomography (CT) scans can provide the resolution necessary for localization [145], but takes several minutes for a single measurement and can only be performed a limited number of times due to radiation limits. Thus far, only electrical impedance has shown promise of having the potential to estimate electrode-modiolar distances intraoperatively.

Impedance measurements are a routine component of CI programming. They are used by audiologists to evaluate electrode function and aid in determining appropriate electrical stimulation levels. Tan et al. [65] were the first to explore the utility of impedance measurements for sensing electrode array location. They found a detectable change in bipolar (electrode-to-electrode) impedance between insertion techniques maintaining modiolar wall contact vs lateral wall contact. These findings were later confirmed by Pile et al. [66]. Giardina et al. [67] presented a technique using monopolar stimulation (electrode to extracochlear ground) to characterize the electrode-saline interface in an effort to study the effects of the individual variables. They determined that the resistive component related to the fluid inside the cochlea (i.e. the access resistance) had the highest correlation with electrode-modiolar distance in plastic phantoms. Through further refinement of a linear regression model, they discovered that an electrode within 1 mm of the modiolus could be correctly identified 78% of the time.

These findings have shown that impedance measurements might one day provide surgeons with the intraoperative information necessary to reduce incidence of trauma and improve placement of electrode arrays. It is a compelling solution to explore further since it requires no modification to existing CIs and poses no radiation risk to patients. In this

chapter, we investigate a hybrid impedance sensing approach that extends the electrical model characterization techniques to bipolar stimulation. We demonstrate that this method greatly improves localization accuracy. In addition, we introduce the first online algorithm for estimating the EA-modiolar proximity in real-time during insertion and perform validation experiments in a to-scale cochlea phantom.

4.3 Modeling

The following sections detail the model used to estimate electrode-modiolar distances from bipolar impedance measurements. In bipolar stimulation, one electrode contact serves as the source and another electrode contact as the sink. In contrast, monopolar stimulation uses an external ground as the sink (e.g. a separate electrode placed in the temporalis muscle). We begin with an equivalent circuit model of the electrode-electrolyte interface, which is then used to predict the electrical response to the standard type of electrical pulses used clinically. We then describe how this response can be related to modiolar proximity.

4.3.1 Equivalent Circuit

A Randles circuit (also called a Randles cell) is one of the simplest and most common equivalent electrical circuit models of an electrode-electrolyte interface [151]. For bipolar stimulation, we actually have two Randles circuits in series since there are two electrode-electrolyte interfaces. This configuration is shown in Fig. 4.2a. The Warburg impedance, Z_w, is a frequency-dependent term that models the diffusion process. The charge transfer resistance, R_{ct}, describes the electrical resistance experienced as electrons on the polarized electrode surface are transferred into charged ions in the electrolytic solution (perilymph in this case). In parallel is the double layer capacitance, C_{dl}. This capacitance is created by the thin insulating space between the charged electrode surface and the nearby ions. Taken together, these terms model the total impedance of the electrode-electrolyte interface. The remaining circuit element is the solution resistance, R_s, which is also called the access

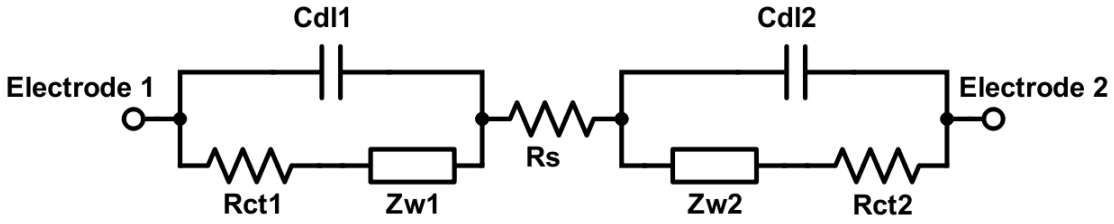

(a)

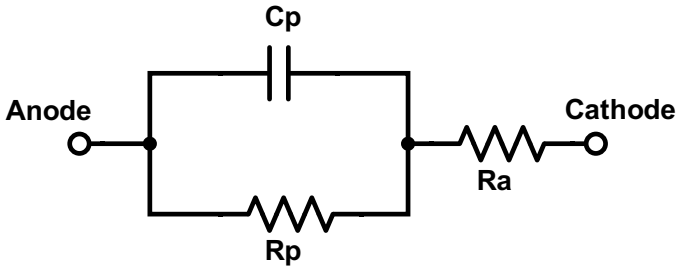

(b)

Figure 4.2: (a) Modifed version of a Randles electrochemical cell equivalent circuit [151] used to model bipolar stimulation of an electrode array. R_{ct} is the charge transfer resistance, C_{dl} is the double layer capacitance, Z_w is the Warburg impedance, and R_s is the electrolytic solution resistance. This circuit can be simplified to yield (b) a reduced equivalent circuit model. The parallel capacitance and resistance, C_p and R_p, can be estimated from experimental calibration. The more common term for the solution resistance is the access resistance, R_a.

resistance, R_a. This is the resistance of the perilymph between the bipolar electrodes, which was shown to be correlated with the electrode-modiolar distance [66, 67].

4.3.2 Electrical Impedance Measurement

Electrical impedance is the ratio of voltage to current in a circuit. Thus, an impedance measurement requires applying either a known voltage or current and measuring the response of the other. In the case of CIs, a controlled current pulse is emitted and the voltage response is recorded. However, a pulse with a significant DC component would create an ionic imbalance and alter the pH of the perilymph. Animal studies have found that DC currents as low as 0.4 µA can cause tissue damage [152]. Thus, a charge-balanced biphasic pulse is used where the total amount of positive charge delivered is balanced with an equal

amount of negative charge. A typical example of such a pulse is shown in Fig. 4.3. At the

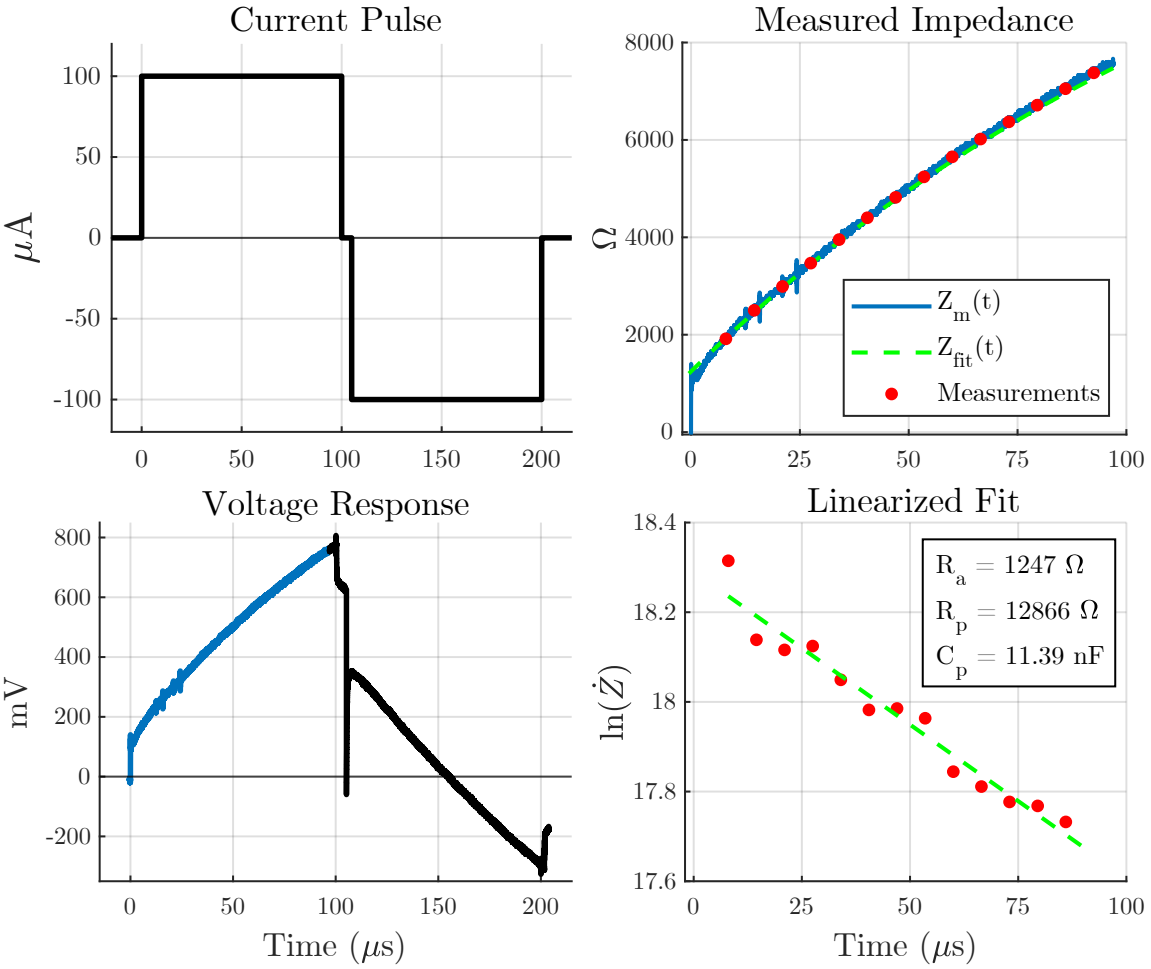

Figure 4.3: A biphasic constant current pulse (top-left) creates a voltage response (bottom-left), which can be analyzed (right) to extract the access resistance, R_a, and the parallel components, R_p and C_p.

high frequencies of CI stimulation, the Warburg impedance is small. It can be neglected or assumed to be a part of the charge transfer resistance, R_{ct}. This yields the Simplified Randles cell, consisting of just a capacitor and resistor in parallel (see Fig. 4.2b). The measured voltage response (see Fig. 4.3 begins with a sharp rise due to the double layer capacitances initially behaving as short circuits. This means that the only impedance component seen at that first instance is the access resistance of the perilymph. Thus, it can be computed as

$$R_a = I/V_a \tag{4.1}$$

where I is the current, and V_a is the voltage measured immediately after applying current. Since the access resistance and current are constants, V_a is constant as well and simply biases any additional voltage created by other circuit elements.

As the current continues until the end of positive phase, the charge across the capacitive components increases, causing the voltage to increase as well. This can be seen in the bottom plot of Fig. 4.3. The parallel resistance/capacitance cause the measured voltage, V_m, to follow a standard first-order response (shown in blue) which can be modeled in order to solve for R_p and C_p. We begin by converting our voltage measurements into impedance values. Then we fit a first-order response by computing the least-squares solution (with form: $y = mx + b$) of the linearized model (see bottom-right of Fig. 4.3).

$$V_m(t) = I \cdot Z_m(t) \implies Z_m(t) = V_m(t)/I \tag{4.2}$$

$$Z_m(t) = R_a + R_p\left[1 - \exp\left(\frac{-t}{R_pC_p}\right)\right] \tag{4.3}$$

$$\dot{Z_o}(t) = \frac{1}{C_p}\exp\left(\frac{-t}{R_pC_p}\right) \tag{4.4}$$

$$\ln\dot{Z_o}(t) = \frac{-1}{R_pC_p}\cdot t + -\ln C_p \tag{4.5}$$

The slope, m, and intercept, b, of the best-fit line to (4.5) yield our desired parameter estimates:

$$b = -\ln C_p \implies C_p = \mathrm{e}^{-b} \tag{4.6}$$

$$m = \frac{-1}{R_pC_p} \implies R_p = \frac{-1}{mC_p} \tag{4.7}$$

Since R_p and C_p are related to the electrode pad geometry (i.e. exposed surface area) and electrode/electrolyte material properties, they can be assumed to remain constant for a given pair of electrodes. Thus, the calibration procedure need only be performed once.

4.3.3 Modiolar Proximity

Pile et al. [66] were the first to experimentally show that there exists an inverse relationship (best approximated by a power law) between the bipolar impedance and the volume of fluid between the stimulated electrodes and the modiolus. They approximated this volume by assuming a projected planar trapezoid, with a vertex at each electrode surface and the nearest point along the modiolar wall. An example is shown in Fig. 4.4, where the red region represents the area corresponding to the bipolar impedance between electrodes 4–5. The key advantage of bipolar measurements is that biological influences on the current pulse are limited to this small area. In contrast, the current in a monopolar configuration must travel out of the the cochlea through the surrounding bone and tissue before reaching the sink electrode. We will use this insight as the starting point to create a model for directly estimating modiolar proximity from impedance measurements.

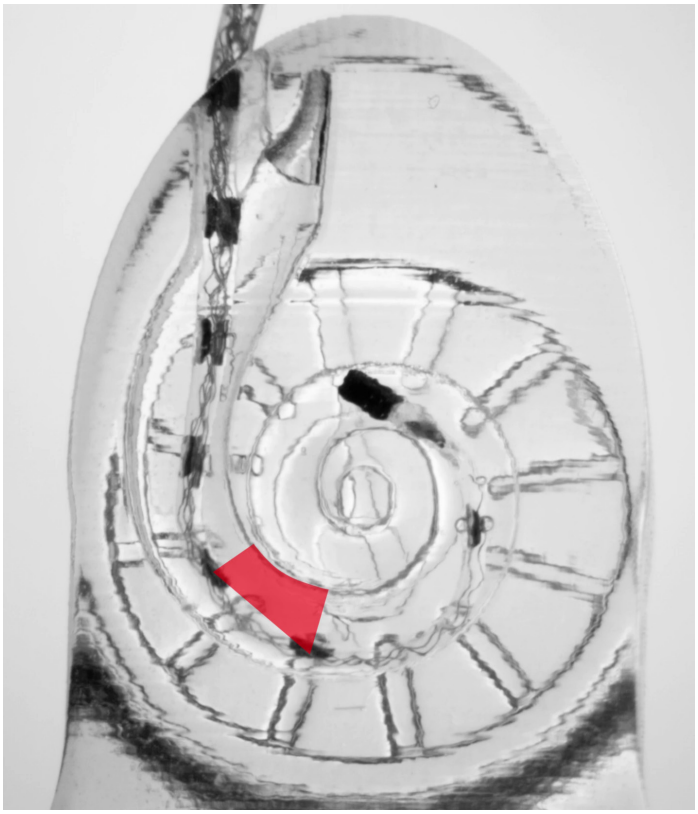

Figure 4.4: The measured bipolar impedance between a pair of electrodes is related to the volume of conductive fluid enclosed between them and the modiolar wall.

We begin with a power function of the form

$$R_a(A) = c_1 A^{c_2} + c_3, \tag{4.8}$$

where R_a is the access resistance (i.e. resistance of the trapped volume of perilymph), c_{1-3} are the coefficients for model fitting, and A is the area.

Since we know R_a and A have an inverse relationship, the exponent c_2 must be negative. This means c_3 represents the horizontal asymptote of the function, which corresponds to the access resistance in an open channel, i.e.

$$c_3 = \lim_{A \to \infty} R_a(A) \tag{4.9}$$

Next, we will linearize (4.8) by taking the natural logarithm of each side and rearranging:

$$\ln\left(R_a(A) - c_3\right) = c_2 \ln A + \ln c_1 \tag{4.10}$$

The least squares linear regression of (4.10) can be computed to determine c_1 and c_2:

$$y = \ln\left(R_a(A) - c_3\right) \tag{4.11}$$

$$x = \ln(A) \tag{4.12}$$

$$c_1 = b \tag{4.13}$$

$$c_2 = m \tag{4.14}$$

Now that we have our power function coefficients, we can rearrange (4.8) in terms of A to obtain our final model for estimating area as a function of the access resistance between a pair of electrodes:

$$A = \left(\frac{R_a - c_3}{c_1}\right)^{-c_2} \tag{4.15}$$

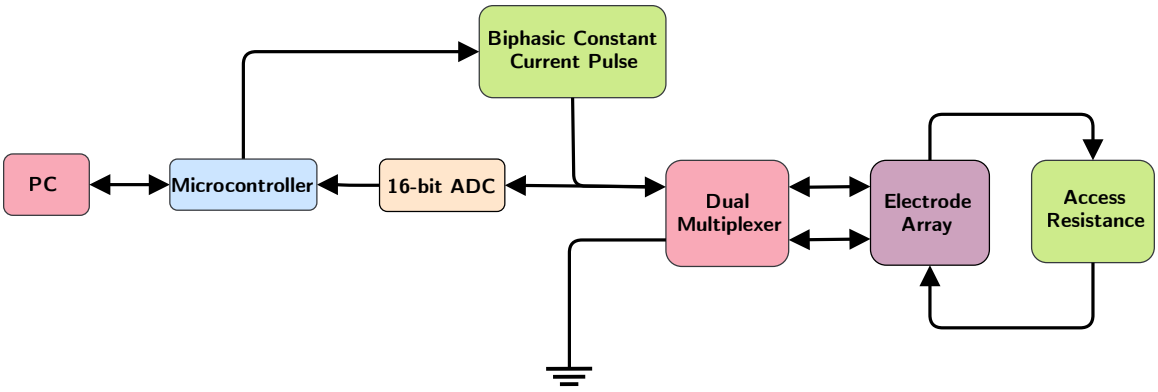

Figure 4.5: Block diagram of circuit designed to measure the bipolar impedance between electrode array contacts. A microcontroller selects a pair of electrode via a dual multiplexer and manages the pulse generation circuitry. Its integrated analog-to-digital converter (ADC) records the voltage during the positive portion of each current pulse, computes the access resistance, and transmits the results to a computer via a USB connection.

4.4 Experimental Methods

4.4.1 Hardware

To experimentally validate this method, we first designed a circuit capable of generating biphasic constant current pulses similar to those used clinically (see Fig. 4.3). The nominal specifications were 100 µs pulses at a constant current of 100 µA. Constant current regulation is managed by a high-accuracy, microcurrent source (REF200, Texas Instruments). Biphasic pulse generation and selection of each electrode pair is achieved via a dual 16-channel analog multiplexer (ADG726, Analog Devices) and a microcontroller (Teensy 3.2, PJRC.COM, LLC). The voltage across the electrode array is buffered through an op amp configured as a voltage follower to limit current leakage. One of the microcontroller's 16-bit analog-to-digital converters (ADC) is used to measure the buffered voltage.

This circuit was implemented on a custom PCB (see Fig. 4.6). It is powered by a battery rather than over USB to provide a clean power source and reduce electrical noise. The microcontroller firmware was written to measure a voltage measurement every 8.5 µs during the positive half of the biphasic pulse. To improve effective resolution, readings

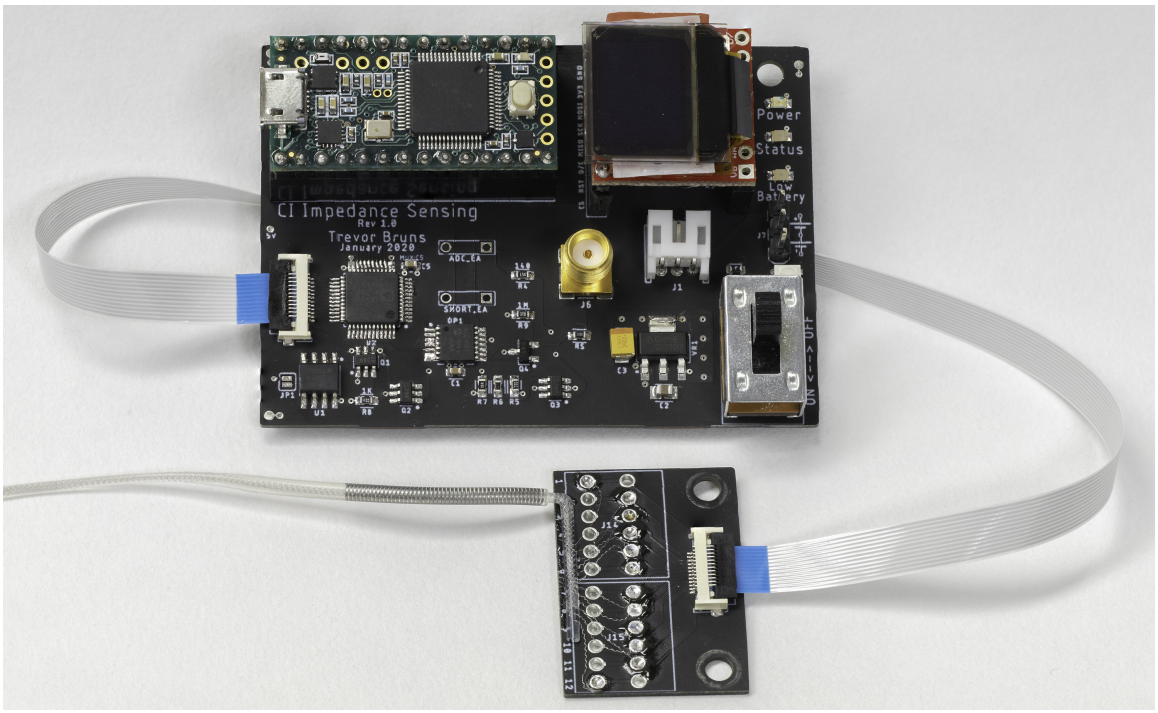

Figure 4.6: Custom circuit board for measuring bipolar impedance. A microcontroller is used to precisely control the desired biphasic current pulses and cycle through each pair of electrodes for testing. Its integrated 16-bit analog-to-digital converter measures the voltage across the two electrode array contacts. Onboard analysis is performed to compute the access resistance, R_a, and transmit it to a PC over a USB-serial connection.

during 20 consecutive pulses were recorded and individually averaged together (i.e. all first measurements averaged, all second measurements, ...). As described in Section 4.3.2, a curve is then fit to these values to estimate the true access resistance. The computed results are then sent over a USB-serial connection to a PC.

4.4.2 Model Validation

Experimental validation of the model described in Sec. 4.3.3 was performed using an anatomically accurate scala-tympani model [153, 132]. This phantom model was filled with a 0.9% saline solution as a surrogate for perilymph since it has very similar electrical properties. A FLEX28 electrode array (MED-EL, Innsbruck, Austria) was connected to the circuit in Fig. 4.6. The microcontroller was configured to use the first five (i.e. most apical)

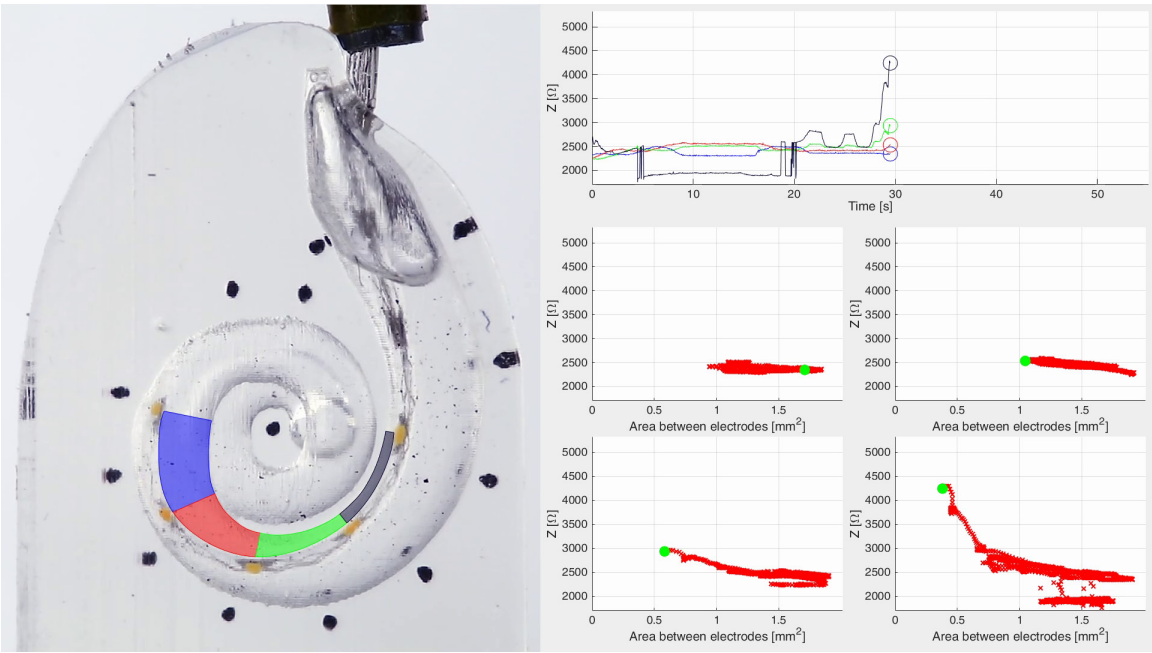

Figure 4.7: Example video frame from post-processed experimental data obtained during theoretical model validation trials. The five most apical electrodes were used to obtain four independent bipolar impedance measurements. The top plot shows these impedances over time. The scatter plots demonstrate the relationship between each channel's impedance and the area enclosed between its pair of contacts and the closest points along the modiolus (shaded regions).

electrodes, yielding four measurement channels. Electrodes 6–12 on the FLEX28 EA are dual electrodes, with a contact on both the inner and outer surface. As one side nears a wall, ordinarily increasing R_a, the other side is moving away from the opposite wall, all but cancelling out the desired effect. Therefore, they were not utilized in these experiments.

The EA was inserted using the the insertion tool introduced in Ch. 3. Simultaneously, video was recorded at 60 fps using a macro lens, and the four channels of bipolar impedance measurements were sent to the connected PC (also at a rate of 60 Hz). The electrode array was manually jogged towards and away from the modiolar wall several times to obtain a range of measurements. A total of three trials were performed (each lasting around 1–2 minutes) resulting in over 10,000 impedance measurements per channel, for a total of approximately 45,000 samples.

Video segmentation to determine the areas corresponding to each measurements was

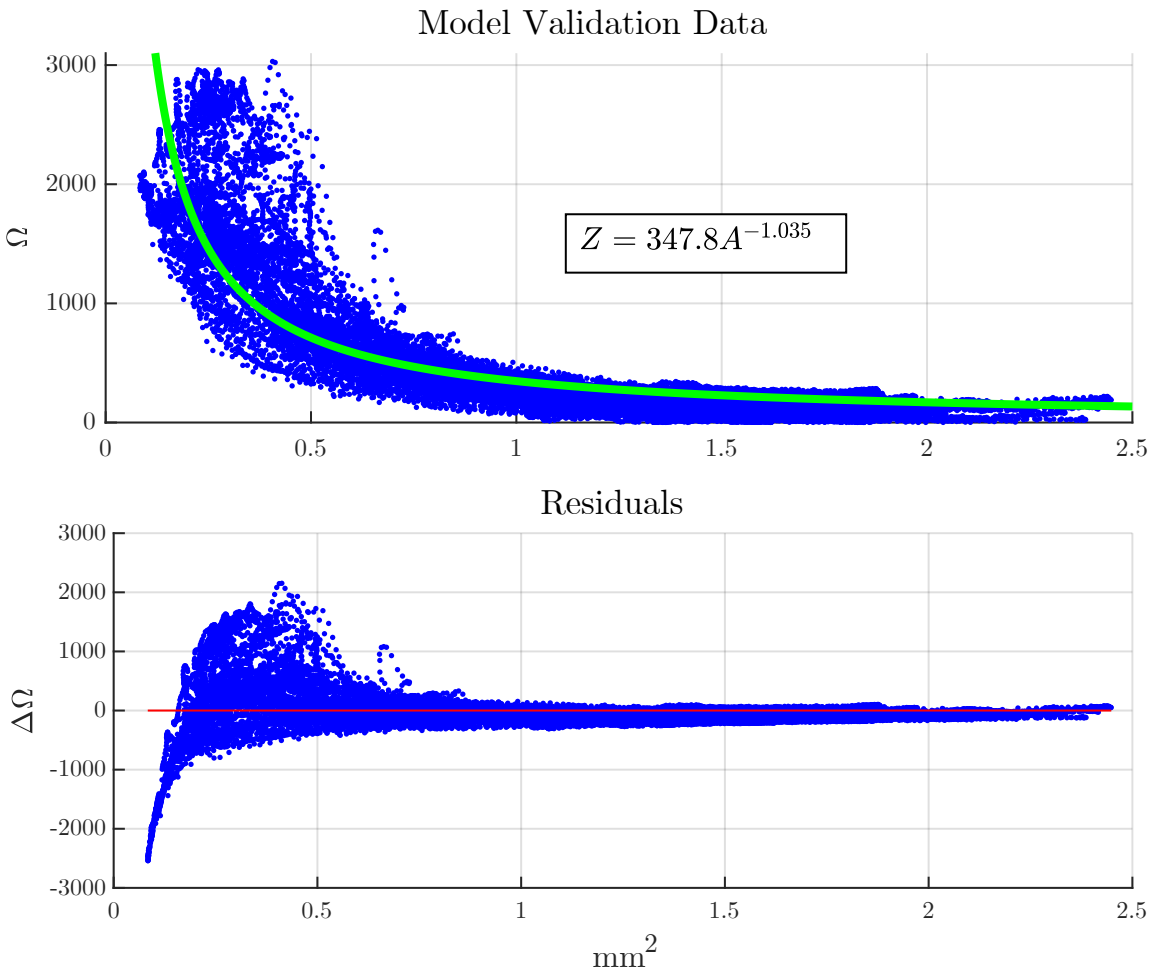

Figure 4.8: Impedance model validation data. In order to directly compare all impedance measurements, the each channel's baseline value (taken as the minimum impedance measurement recorded during each individual trial) was subtracted from the raw measurements. (Top) Bias-subtracted impedance as a function of EA-modiolar area. A power-law function was fit using a nonlinear least-squares algorithm. (Bottom) Plot of the corresponding residual values.

performed in two stages. First, Adobe After Effects (Adobe Inc., San Jose, CA) was used to track the electrode locations and place a small colored circle on top of each. Next, a colored mask was created for the modiolus and the EA. This 'pre-processed' video was then segmented in MATLAB (MathWorks, Natick, MA) to calculate the each channel's area for every frame. Finally, the impedance data was synced with the video frames for direct comparison with the area measurements. The resulting 'post-processed' video overlays colored regions for each channel area and includes scatter plots to show the relationship

between impedance and area. An example frame from one of the experimental trials is shown in Fig. 4.7.

The final results after analysis are shown in Fig. 4.8. Since every channel has its own bias level, these were first removed in order to plot all data together. The data agrees well with the model, and the power law distribution provides a good approximation of the overall trend. However, as the area approaches zero the residual errors increase significantly. This is due to both the highly nonlinear nature of the effect and the simplicity of this model; a multidimensional problem is being reduced to a single variable. This is best evidenced by the 'spreading' of the data with decreasing areas. If a single electrode in a pair is very close a wall, the overall impedance measured will be biased higher than expected when using this model alone. Thus, there is a fundamental limit to the accuracy achievable solely by a simple model fit.

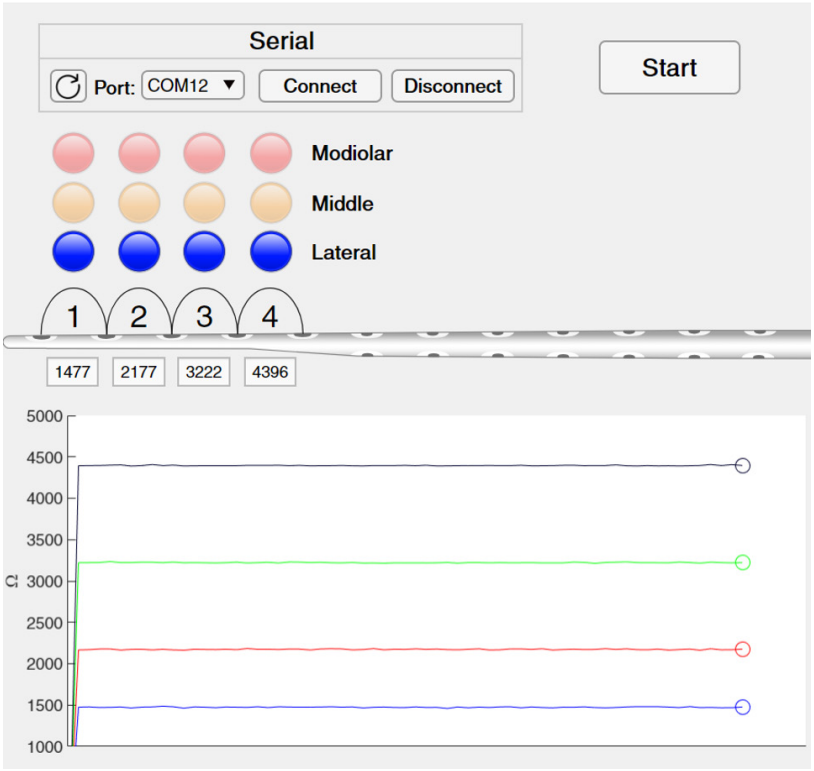

Figure 4.9: Real-time localization GUI. Colored indicator lights show the current predicted location of each EA channel, while the raw values are plotted below.

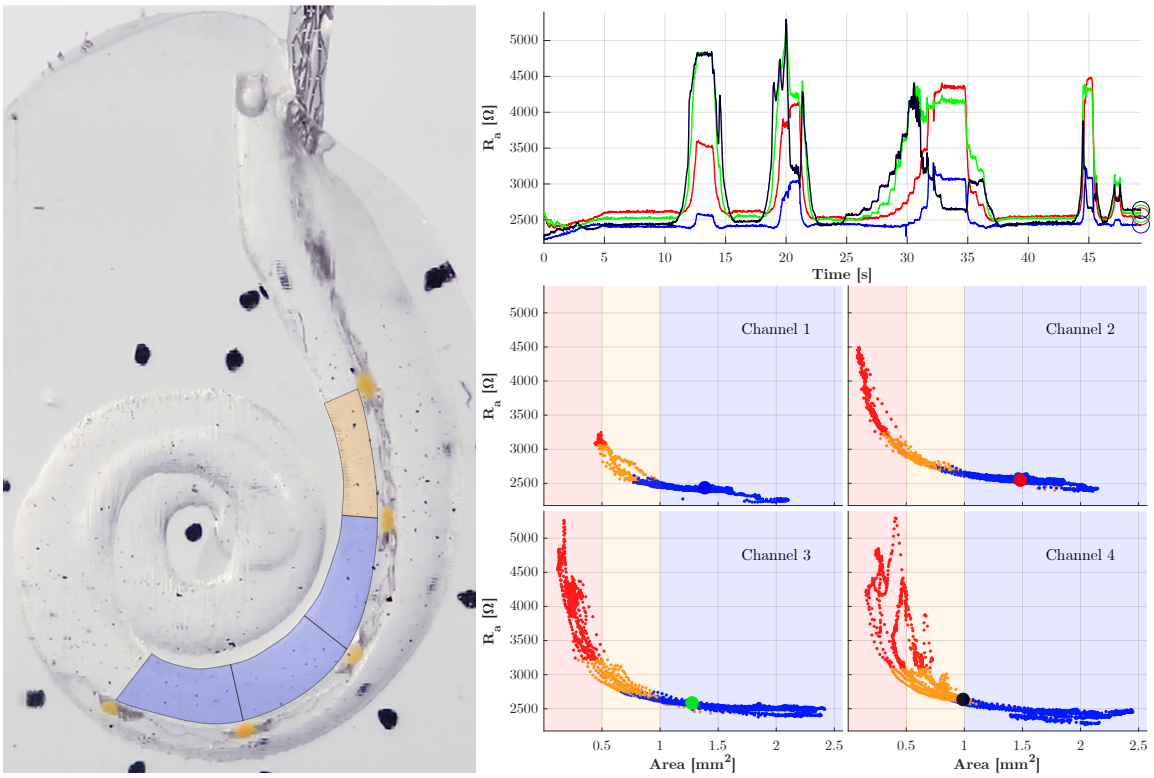

Figure 4.10: Example video frame obtained during the phantom trial used as the test data for evaluating the trained neural network's predictions. The five most apical electrodes were used to obtain four independent bipolar impedance measurements. Each is proportional to the area enclosed between its pair of contacts and the closest points along the modiolus. The predicted location is depicted by the color of the shaded areas.

4.4.3 Real-time Localization

In order to achieve dependable real-time localization of CIs during insertion, a more sophisticated model is necessary. It can be empirically observed that as a bipolar electrode pair move towards or away from a wall, the impedance values change smoothly. Thus, the 'history' of the impedance measurements might be as useful as the absolute value. There are many ways this type of heuristic could be implemented, but given the complexity of the system we are tying to model, a machine learning approach was chosen. In particular, a Long Short-Term Memory (LSTM) recurrent neural network was implemented using MATLAB's Deep Learning Toolbox.

The network was designed to take a sequence of values (e.g. impedances) as input

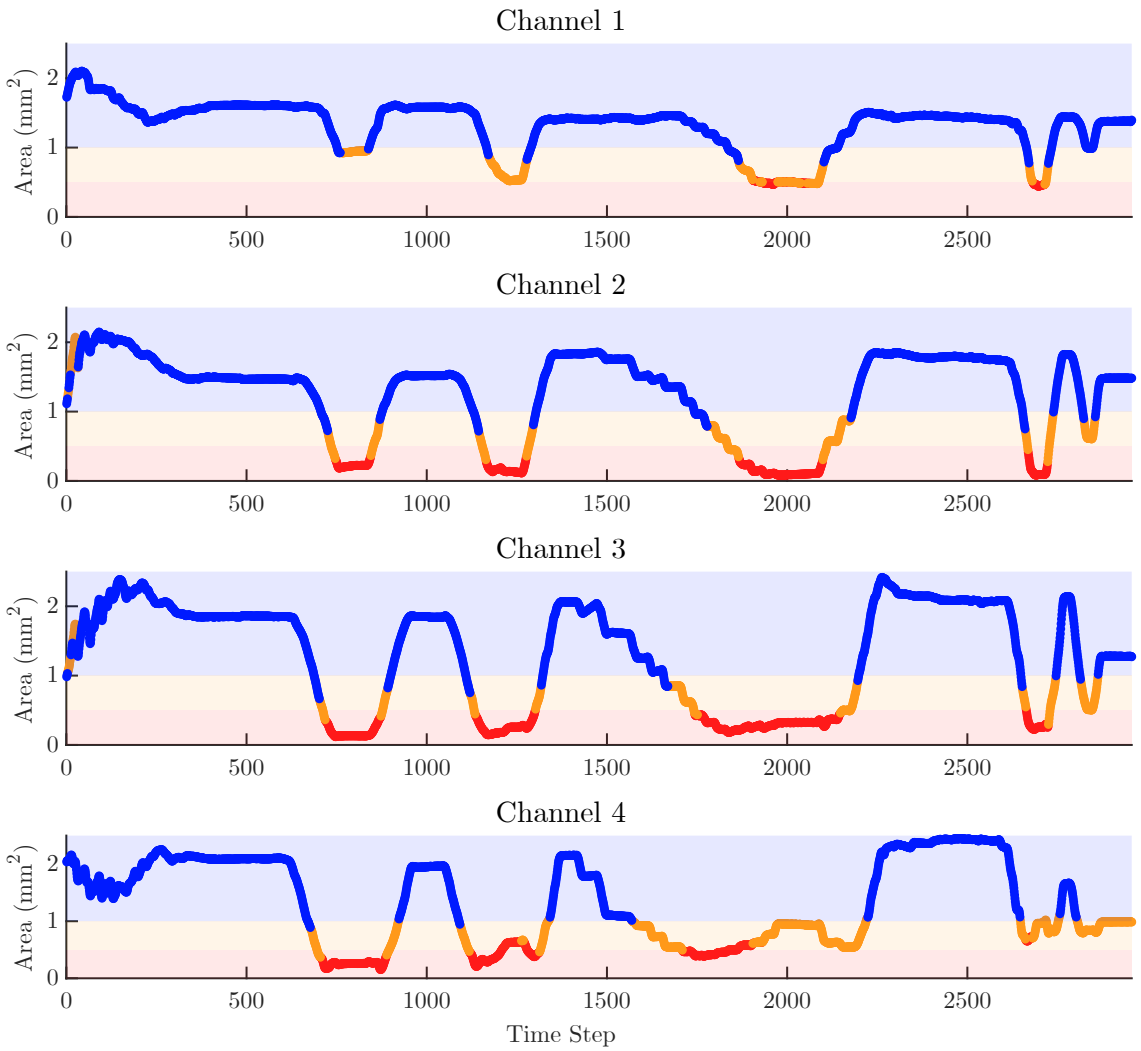

Figure 4.11: Comparison of predicted location to the measured area for the test trial. The red region corresponds to a 'modiolar' prediction (i.e. less the 0.5 mm^2 between that channels electrodes and the modiolar wall), orange signifies 'middle' (0.5 mm^2 to 1.0 mm^2), while blue designates a 'lateral' position (greater than 1.0 mm^2).

and produce a prediction of one of three classes. These classes represent three possible location regions: 'modiolar' (i.e. less the 0.5 mm^2 between that channel's electrodes and the modiolar wall), 'lateral' (i.e. greater than 1.0 mm^2), and a 'middle' between those (0.5 mm^2 to 1.0 mm^2).

The LSTM layer was given 120 hidden units and the the network was trained using two of the three sets of trial data previously acquired. The third trial was then run through the network to evaluate its accuracy. The results are shown in Fig. 4.10, which provides the

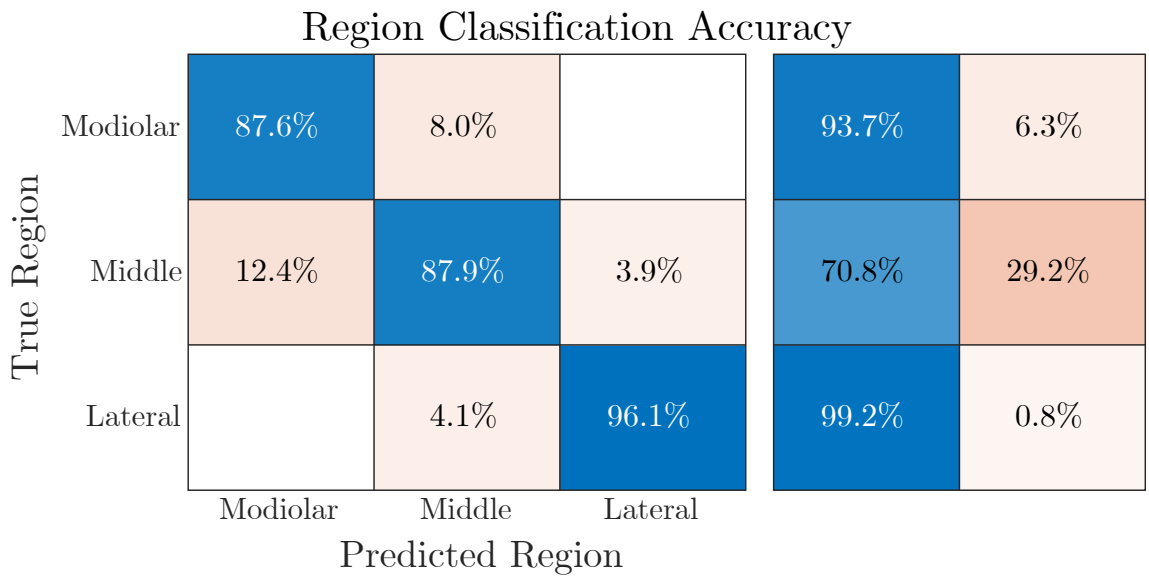

Figure 4.12: Confusion matrix of the trained neural network for predicting EA location. A row-normalized row summary displays the percentages of correctly and incorrectly classified observations for each true class. The combined overall prediction accuracy was over 93%

same data as Fig. 4.7 except that now the color of the shaded regions depicts the network's current predictions for each channel. A plot of all predictions during the course of the trial is shown in Fig. 4.11. The confusion matrix summary of the network's classification accuracy is shown in Fig. 4.12. The overall accuracy was over 93%. The most difficult region is the middle, but it still managed a precision of 87.9% for middle predictions. In addition, the trained network runs in real-time as new measurements are streamed in from the microcontroller.

4.5 Conclusion

In this chapter, prior impedance models were built upon to further explore the relationship between electrical impedance and the location of the electrode array within the cochlea. We performed the most extensive validation experiments to date and showed that the results agree well with simplified theoretical models. We then investigated how a recurrent neural network can be utilized to further improve localization accuracy. Finally, we

demonstrated for the first time a method for providing real-time location predictions during EA insertion.

Chapter 5

Future Work & Conclusions

5.1 Future Work: Concentric Tube Robot System for Transnasal Surgery

The robotic system presented in Chapter 2 builds upon prior concentric tube robot systems in ways that aim to bring it closer toward surgical use in the operating room. A sterile draping strategy was incorporated, which was dependent on the introduction of modular, interchangeable tool cartridges. Custom, modular motor control electronics improved safety and reliability. The tools exit through a tube collimator, enabling multiple tools to be deployed in close proximity for transnasal application. These are all important advancements on the path toward clinical translation, but future work remains. Thorough testing of the sterilization technique is needed to assess whether it can pass sterility requirements. A user study should also be performed to ensure it does not pose workflow issues to the OR staff. Additionally, more safety features are necessary for regulatory approval. Integration of sensing technologies such as magnetic tracking would improve both safety and operation. Another avenue for research is the exploration of other surgical applications. There are several procedures in the skull base, sinuses, and orbits that warrant further study.

5.2 Future Work: Magnetic Steering System for Cochlear-Implant Electrode Arrays

The magnetic steering system in Chapter 3 integrated several techniques related to CI surgery into a single system. Since this marks the first time that preoperative imaging, image analysis/segmentation, image guidance, magnetic steering, and a robotic insertion tool have been employed together, there are many future directions one could take. A comprehensive study could be performed comparing the various insertion strategies proposed in

the literature. In particular, the robotic insertion tool and magnetic steering provide a new degree of control. Dithering methods can be explored. For example, the electrode array could be dithered axially via the linear actuator during insertion, or dithered laterally via the Omnimanget. The speed of insertion can be also studied in relation to the forces experienced. The force measurements themselves could be used actively for closed-loop control. The entire system could even be applied to a completely new area outside of CI surgery.

5.3 Future Work: Real-time Localization of Cochlear-Implant Electrode Arrays

The use of electrical impedance as a sensing modality during cochlear implant surgery has many advantages. It does not require modification to existing clinical electrodes. It is capable of (and indeed actually best at) sensing submillimetric distances in real-time. There is no CT scan or additional radiation risk posed to the patient. The phantom experiments conducted demonstrate the robustness and potential of this method. Future directions might include implementing this method with a clinical CI system so it could be evaluated in live patients in the OR. This should be feasible since it does not require modification to the electrode array and was tested using clinically-relevant pulse parameters. A wider variety of electrode array models should be studied to determine how much variance exists between arrays of the same type and different types. This will dictate how much calibration and training data is necessary to obtain useful results. Finally, this sensing method could be utilized as feedback for the magnetic steering system in Chapter 3 to enable closed-loop control.

5.4 Conclusions

The transnasal robotic system presented in Chapter 2 brings concentric tube robots closer to the operating room. Sterility concerns were addressed by a sterile draping concept suitable for this new class of concentric tube robots. Modular, customized motor control electronics improve the safety, reliability, and flexibility of the system. A minimally-

invasive, multi-arm device with modular tools that can be quickly changed during a procedure opens the door to many new applications. This was exemplified by performing the first robotic removal of tumors in the orbit.

The magnetic steering system introduced in Chapter 3 provides much greater control of cochlear implant electrode arrays than was previously thought possible. These miniature implants have changed hundreds of thousands of lives, but positioning them carefully and accurately into the optimal location within the cochlea has remained a challenge. This robotic system integrates important advances in every aspect of the procedure. Preoperative imaging is utilized to determine the optimal trajectory specific to each patient. Image guidance ensures the tools are aligned accurately according to the surgical plan. A robotic insertion tool deploys the electrode array with precision. And now, for the first time, an electromagnet is used to enhance control of the array by bending the tip away from lateral wall. Taken together, this system has the potential to make a notable impact on cochlear implant surgery. Initial experiments in both phantom models and cadaveric cochleae demonstrated how insertion forces can be reduced by 50%.

Chapter 4 introduces a new method for detecting the intracochlear location of an electrode array in real-time through the use of bipolar electrical impedance measurements. A model was derived based on the electrochemical reactions that take place during electrical stimulation. Hardware and software was designed to replicate the biphasic current pulses used in clinical cochlear implants. The model was validated using anatomically accurate phantom models. Additionally, a recurrent neural network was implemented, which was capable of providing the first real-time localization estimates during insertion. These promising results represent the very beginnings of how this technology can be applied.

In summary, this dissertation provides several important advancements toward the goal of surgical robotic systems for controlling flexible devices. Traditional rigid-link mechanisms may be easier to model and manipulate, but their lack of inherent compliance and poor scalability means they are starting to be phased out of medical applications in favor

of continuum ones. This will only accelerate with the current trend toward minimally-invasive surgeries. Concentric tube robots, like the system in Chapter 2, have made great strides in the past decade and have demonstrated that they have the potential to supplant many of these older technologies. Likewise, as medical science continues to advance, we discover new ways in which implantable devices can augment, block, and even restore our senses. The efficacy of these small elastic implants is usually predicated on precise placement near delicate structures in hard-to-reach locations. Magnetic steering systems like the one in Chapter 3 and novel sensing modalities such as the electrical impedance method in Chapter 4 will one day make these operations routine.

BIBLIOGRAPHY

[1] Yik San Kwoh, Joahin Hou, Edmond A Jonckheere, and Samad Hayati. A robot with improved absolute positioning accuracy for ct guided stereotactic brain surgery. *IEEE Transactions on Biomedical Engineering*, 35(2):153–160, 1988.

[2] KH Fuchs. Minimally invasive surgery. *Endoscopy*, 34(02):154–159, 2002.

[3] Shigeo Hirose and Peter Cave. *Biologically inspired robots: snake-like locomotors and manipulators*. Oxford University Press, 1993.

[4] Jessica Burgner-Kahrs, D Caleb Rucker, and Howie Choset. Continuum robots for medical applications: A survey. *IEEE Transactions on Robotics*, 31(6):1261–1280, 2015.

[5] Hunter B Gilbert, D Caleb Rucker, and Robert J Webster III. Concentric tube robots: The state of the art and future directions. In *Robotics Research*, pages 253–269. Springer, 2016.

[6] Robert J Webster, Allison M Okamura, and Nah J Cowan. Toward active cannulas: Miniature snake-like surgical robots. In *Intelligent Robots and Systems, 2006 IEEE/RSJ International Conference on*, pages 2857–2863. IEEE, 2006.

[7] Junji Furusho, Tomoya Ono, Ryousuke Murai, Tetsuo Fujimoto, Yoshihide Chiba, and Hiroyuki Horio. Development of a curved multi-tube (cmt) catheter for percutaneous umbilical blood sampling and control methods of cmt catheters for solid organs. In *IEEE International Conference Mechatronics and Automation, 2005*, volume 1, pages 410–415. IEEE, 2005.

[8] Patrick Sears and Pierre E Dupont. A steerable needle technology using curved concentric tubes. In *IROS*, pages 2850–2856, 2006.

[9] Daniel C Rucker, B A Jones, and Robert J Webster III. A Geometrically Exact Model for Externally Loaded Concentric Tube Continuum Robots. *IEEE Transactions on Robotics*, 26(5):769–780, 2010.

[10] Pierre E Dupont, Jesse Lock, Brandon Itkowitz, and Evan Butler. Design and control of concentric-tube robots. *IEEE Transactions on Robotics*, 26(2):209–225, 2010.

[11] Evan J Butler, Robert Hammond-Oakley, Szymon Chawarski, Andrew H Gosline, Patrick Codd, Tomer Anor, Joseph R Madsen, Pierre E Dupont, and Jesse Lock. Robotic neuro-endoscope with concentric tube augmentation. In *International Conference on Intelligent Robots and Systems*, pages 2941–2946. IEEE, 2012.

[12] J Burgner, Philip J Swaney, R A Lathrop, Kyle D Weaver, and Robert J Webster III. Debulking From Within: A Robotic Steerable Cannula for Intracerebral Hemorrhage Evacuation. *IEEE Transactions on Biomedical Engineering*, 60(9):2567–2575, 2013.

[13] J Burgner, Daniel C Rucker, Hunter B Gilbert, Philip J Swaney, Paul T Russell III, Kyle D Weaver, and Robert J Webster III. A Telerobotic System for Transnasal Surgery. *IEEE/ASME Transactions on Mechatronics*, 19(3):996–1006, 2014.

[14] Jessica Burgner, Philip J Swaney, Trevor L Bruns, Marlena S Clark, D Caleb Rucker, E Clif Burdette, and Robert J Webster. An autoclavable steerable cannula manual deployment device: Design and accuracy analysis. *Journal of medical devices*, 6(4): 041007, 2012.

[15] Richard J Hendrick, C R Mitchell, S D Herrell, and Robert J Webster III. Hand-Held Transendoscopic Robotic Manipulators: A Transurethral Laser Prostate Surgery Case Study. *International Journal of Robotics Research*, 34(15):1559–1572, 2015.

[16] Philip J Swaney, Arthur W Mahoney, Bryan I Hartley, Andria A Remirez, Erik Lamers, Richard H Feins, Ron Alterovitz, and Robert J Webster III. Toward tran-

soral peripheral lung access: Combining continuum robots and steerable needles. *Journal of medical robotics research*, 2(01):1750001, 2017.

[17] Nikolay V Vasilyev, Pierre E Dupont, and Pedro J Del Nido. Robotics and imaging in congenital heart surgery. *Future cardiology*, 8(2):285–296, 2012.

[18] Yuhei Saito, Hiroshi Yasuhara, Satoshi Murakoshi, Takami Komatsu, Kazuhiko Fukatsu, and Yushi Uetera. Challenging residual contamination of instruments for robotic surgery in japan. *infection control & hospital epidemiology*, 38(2):143–146, 2017.

[19] Trevor Bruns, John Tucker, D Caleb Rucker, Philip Swaney, Emad Boctor, E Clif Burdette, Jessica Burgner, and Robert Webster. Design of an autoclavable active cannula deployment device. *Journal of Medical Devices*, 5(2):027538, 2011.

[20] Carmen M Graves, Alex Slocum, Rajiv Gupta, and Conor J Walsh. Towards a compact robotically steerable thermal ablation probe. In *2012 IEEE International Conference on Robotics and Automation*, pages 709–714. IEEE, 2012.

[21] Yifan Zhu, Philip J Swaney, Isuru S Godage, Ray A Lathrop, and Robert J Webster. A disposable robot for intracerebral hemorrhage removal. *Journal of Medical Devices*, 10(2):020952, 2016.

[22] Jessica Burgner, Philip J Swaney, Ray A Lathrop, Kyle D Weaver, and Robert J Webster. Debulking from within: a robotic steerable cannula for intracerebral hemorrhage evacuation. *IEEE transactions on biomedical engineering*, 60(9):2567–2575, 2013.

[23] Haibo Yu, Liao Wu, Keyu Wu, and Hongliang Ren. Development of a multi-channel concentric tube robotic system with active vision for transnasal nasopharyngeal carcinoma procedures. *IEEE Robotics and Automation Letters*, 1(2):1172–1178, 2016.

[24] Russell H Taylor and Dan Stoianovici. Medical robotics in computer-integrated surgery. *IEEE TRANSACTIONS ON ROBOTICS AND AUTOMATION*, 19(5):765, 2003.

[25] Richard J Hendrick. *System Design and Elastic Stability Modeling of Transendoscopic Continuum Robots*. PhD thesis, Vanderbilt University, 2017.

[26] P. J. Swaney, J. M. Croom, J. Burgner, H. B. Gilbert, D. C. Rucker, P. T. Russell III, K. D. Weaver, and R. J. Webster III. Design of a Quadramanual Robot for Single-Nostril Skull Base Surgery. In *Dynamic Systems and Control Conference*, pages 387–393. ASME, 2012.

[27] André Djourno and Charles Eyriès. Prothèse auditive par excitation électrique à distance du nerf sensoriel à l'aide d'un bobinage inclus à demeure. *La Presse Médicale*, 65:1417, 1957.

[28] RF Bilger, OF Black, EN Myers, et al. Evaluation of subjects presently fitted with implanted auditory prostheses. report on nih contract n01-ns-5-2331. *Eye and Ear Hospital, Pittsburgh*, 1976.

[29] Blake S Wilson and Michael F Dorman. Cochlear implants: current designs and future possibilities. *J. Rehabil. Res. Dev.*, 45(5):695–730, 2008.

[30] The Ear Foundation. *Cochlear Implant Information Sheet*, 2016. URL https://www.earfoundation.org.uk/hearing-technologies/cochlear-implants/cochlear-implant-information-sheet.

[31] Joe Saliba, Heather Bortfeld, Daniel J Levitin, and John S Oghalai. Functional near-infrared spectroscopy for neuroimaging in cochlear implant recipients. *Hearing research*, 338:64–75, 2016.

[32] Diane S Lazard, Hamish Innes-Brown, and Pascal Barone. Adaptation of the communicative brain to post-lingual deafness. evidence from functional imaging. *Hearing research*, 307:136–143, 2014.

[33] Richard T Miyamoto, Mary Joe Osberger, Susan L Todd, Amy M Robbins, Barbara S Stroer, Susan Zimmerman-Phillips, and Arlene E Carney. Variables affecting implant performance in children. *Laryngoscope*, 104(9):1120–1124, 1994.

[34] Qian-Jie Fu and Geraldine Nogaki. Noise susceptibility of cochlear implant users: the role of spectral resolution and smearing. *Journal of the Association for Research in Otolaryngology*, 6(1):19–27, 2005.

[35] Scott A Wade, James B Fallon, Andrew K Wise, Robert K Shepherd, Natalie L James, and Paul R Stoddart. Measurement of forces at the tip of a cochlear implant during insertion. *IEEE Transactions on Biomedical Engineering*, 61(4):1177–1186, 2014.

[36] Daniel Schuster, Louis B Kratchman, and Robert F Labadie. Characterization of intracochlear rupture forces in fresh human cadaveric cochleae. *Otology & neurotology: official publication of the American Otological Society, American Neurotology Society [and] European Academy of Otology and Neurotology*, 36(4):657, 2015.

[37] Louis B Kratchman, Daniel Schuster, Mary S Dietrich, and Robert F Labadie. Force perception thresholds in cochlear implantation surgery. *Audiology and Neurotology*, 21(4):244–249, 2016.

[38] Bernard Fraysse, Ángel Ramos Macías, Olivier Sterkers, Sandro Burdo, Richard Ramsden, Olivier Deguine, Thomas Klenzner, Thomas Lenarz, Manuel Manrique Rodriguez, Ernst Von Wallenberg, et al. Residual hearing conservation and electroacoustic stimulation with the nucleus 24 contour advance cochlear implant. *Otology & neurotology*, 27(5):624–633, 2006.

[39] Wolfgang K Gstoettner, Paul Van de Heyning, Alec Fitzgerald O'Connor, Constantino Morera, Manuel Sainz, Katrien Vermeire, Sonelle McDonald, Laura Cavallé, Silke Helbig, Juan Garcia Valdecasas, et al. Electric acoustic stimulation of the auditory system: results of a multi-centre investigation. *Acta oto-laryngologica*, 128 (9):968–975, 2008.

[40] Brendan P O'Connell, Jacob B Hunter, David S Haynes, Jourdan T Holder, Matt M Dedmon, Jack H Noble, Benoit M Dawant, and George B Wanna. Insertion depth impacts speech perception and hearing preservation for lateral wall electrodes. *The Laryngoscope*, 127(10):2352–2357, 2017.

[41] Jourdan T Holder, David M Kessler, Jack H Noble, René H Gifford, and Robert F Labadie. Prevalence of extracochlear electrodes: Computerized tomography scans, cochlear implant maps, and operative reports. *Otology & Neurotology*, 39(5):e325–e331, 2018.

[42] Srijata Chakravorti, Jack H Noble, René H Gifford, Benoit M Dawant, Brendan P O'Connell, Jianing Wang, and Robert F Labadie. Further evidence of the relationship between cochlear implant electrode positioning and hearing outcomes. *Otology & Neurotology*, 40(5):617–624, 2019.

[43] Jian Zhang, Kai Xu, Nabil Simaan, and Spiros Manolidis. A pilot study of robot-assisted cochlear implant surgery using steerable electrode arrays. In *International Conference on Medical Image Computing and Computer-Assisted Intervention*, pages 33–40. Springer, 2006.

[44] Jian Zhang, Wei Wei, Jienan Ding, J Thomas Roland Jr, Spiros Manolidis, and Nabil Simaan. Inroads toward robot-assisted cochlear implant surgery using steerable electrode arrays. *Otol. Neurotol.*, 31(8):1199–1206, 2010.

[45] Jason Pile and Nabil Simaan. Modeling, design, and evaluation of a parallel robot

for cochlear implant surgery. *IEEE/ASME Trans. Mechatronics*, 19(6):1746–1755, 2014.

[46] Daniel Schurzig, Robert F Labadie, Andreas Hussong, Thomas S Rau, and Robert J Webster III. Design of a tool integrating force sensing with automated insertion in cochlear implantation. *IEEE/ASME Trans. Mechatronics*, 17(2):381–389, 2012.

[47] Robert F Labadie, Ramya Balachandran, Jack H Noble, Grégoire S Blachon, Jason E Mitchell, Fitsum A Reda, Benoit M Dawant, and J Michael Fitzpatrick. Minimally invasive image-guided cochlear implantation surgery: First report of clinical implementation. *The Laryngoscope*, 124(8):1915–1922, 2014.

[48] Jian Zhang, Samrat Bhattacharyya, and Nabil Simaan. Model and parameter identification of friction during robotic insertion of cochlear-implant electrode arrays. In *Proc. IEEE Int. Conf. Robot. Autom.*, pages 3859–3864, 2009.

[49] Frank M Warren, Ramya Balachandran, J Michael Fitzpatrick, and Robert F Labadie. Percutaneous cochlear access using bone-mounted, customized drill guides: demonstration of concept in vitro. *Otology & Neurotology*, 28(3):325–329, 2007.

[50] H Eilers, S Baron, T Ortmaier, B Heimann, C Baier, Th S Rau, M Leinung, and O Majdani. Navigated, robot assisted drilling of a minimally invasive cochlear access. In *2009 IEEE International Conference on Mechatronics*, pages 1–6. IEEE, 2009.

[51] Andreas Hussong, Thomas S Rau, Tobias Ortmaier, Bodo Heimann, Thomas Lenarz, and Omid Majdani. An automated insertion tool for cochlear implants: another step towards atraumatic cochlear implant surgery. *Int. J. Comput. Assist. Radiol. Surg.*, 5 (2):163–171, 2010.

[52] Jian Zhang, J Thomas Roland, Spiros Manolidis, and Nabil Simaan. Optimal path planning for robotic insertion of steerable electrode arrays in cochlear implant surgery. *J. Med. Devices*, 3(1):011001, 2009.

[53] H Mayer Jr and US Naval Med Bull. Passage of miller-abbott tube through the pylorus with aid of electromagnet. *US Nav. M. Bull*, 43:463–466, 1944.

[54] John W Devine. Duodenal intubation. *Surgery*, 33(4):513–515, 1953.

[55] Hans Tillander. Magnetic guidance of a catheter with articulated steel tip. *Acta radiologica*, 35(1):62–64, 1951.

[56] James R Clark, Lisandro Leon, Frank M Warren, and Jake J Abbott. Investigation of magnetic guidance of cochlear implants. In *Intelligent Robots and Systems (IROS), 2011 IEEE/RSJ International Conference on*, pages 1321–1326. IEEE, 2011.

[57] Mariam Maghribi, Peter Krulevitch, James Davidson, and Julie Hamilton. Implantable devices using magnetic guidance, March 9 2006. US Patent App. 10/938,816.

[58] Lisandro Leon, Frank M Warren, and Jake J Abbott. An in-vitro insertion-force study of magnetically guided lateral-wall cochlear-implant electrode arrays. *Otol. Neurotol.*, 39(2):e63–e73, 2018.

[59] Jianbai Wang and Kensall D Wise. A thin-film cochlear electrode array with integrated position sensing. *Journal of Microelectromechanical Systems*, 18(2):385–395, 2009.

[60] J Wans, M Gulari, PT Bhatti, BY Arcand, K Beach, CR Friedrich, and KD Wise. A cochlear electrode array with built-in position sensing. In *18th IEEE International Conference on Micro Electro Mechanical Systems, 2005. MEMS 2005.*, pages 786–789. IEEE, 2005.

[61] Hirobumi Watanabe, J Velmurugan, Michael V Mirkin, Mario A Svirsky, Anil K Lalwani, and Rodolfo R Llinás. Scanning electrochemical microscopy as a novel proximity sensor for atraumatic cochlear implant insertion. *IEEE transactions on biomedical engineering*, 61(6):1822–1832, 2014.

[62] Jason Pile, George B Wanna, and Nabil Simaan. Force-based flexible path plans for robotic electrode insertion. In *Robotics and Automation (ICRA), 2014 IEEE International Conference on*, pages 297–303. IEEE, 2014.

[63] Jason Pile and Nabil Simaan. Characterization of friction and speed effects and methods for detection of cochlear implant electrode tip fold-over. In *Proc. IEEE Int. Conf. Robot. Autom.*, pages 4409–4414, 2013.

[64] Jason Pile, George B Wanna, and Nabil Simaan. Robot-assisted perception augmentation for online detection of insertion failure during cochlear implant surgery. *Robotica*, 35(7):1598–1615, 2017.

[65] Chin-Tuan Tan, Mario Svirsky, Abbas Anwar, Shaun Kumar, Bernie Caessens, Paul Carter, Claudiu Treaba, and J Thomas Roland. Real-time measurement of electrode impedance during intracochlear electrode insertion. *The Laryngoscope*, 123 (4):1028–1032, 2013.

[66] Jason Pile, Alex D Sweeney, Shaun Kumar, Nabil Simaan, and George B Wanna. Detection of modiolar proximity through bipolar impedance measurements. *The Laryngoscope*, 127(6):1413–1419, 2017.

[67] Christopher Kenneth Giardina, Elliot Samuel Krause, Kanthaiah Koka, and Douglas Carl Fitzpatrick. Impedance measures during in vitro cochlear implantation predict array positioning. *IEEE Transactions on Biomedical Engineering*, 65(2): 327–335, 2018.

[68] Jason Pile. *Wire-actuated Parallel Robots for Cochlear Implantation With In-Vivo Sensory Feedback*. PhD thesis, Vanderbilt University, 2015.

[69] Jessica Burgner, Philip J Swaney, D Caleb Rucker, Hunter B Gilbert, Scott T Nill, Paul T Russell, Kyle D Weaver, and Robert J Webster. A bimanual teleoperated system for endonasal skull base surgery. In *Intelligent Robots and Systems (IROS), 2011 IEEE/RSJ International Conference on*, pages 2517–2523. IEEE, 2011.

[70] James R Clark, Lisandro Leon, Frank M Warren, and Jake J Abbott. Magnetic guidance of cochlear implants: Proof-of-concept and initial feasibility study. *J. Med. Devices*, 6(3):035002, 2012.

[71] Jack H Noble, Benoit M Dawant, Frank M Warren, and Robert F Labadie. Automatic identification and 3-d rendering of temporal bone anatomy. *Otol. Neurotol.*, 30(4): 436, 2009.

[72] Jack H Noble, Frank M Warren, Robert F Labadie, Benoit Dawant, and J Michael Fitzpatrick. Determination of drill paths for percutaneous cochlear access accounting for target positioning error. In *Proc. SPIE Medical Imaging*, volume 6509, page 650925, 2007.

[73] Arnau Garriga-Casanovas and Ferdinando Rodriguez y Baena. Complete follow-the-leader kinematics using concentric tube robots. *The International Journal of Robotics Research*, 37(1):197–222, 2018.

[74] J Wurm, T Dannenmann, C Bohr, H Iro, and K Bumm. Increased safety in robotic paranasal sinus and skull base surgery with redundant navigation and automated registration. *The International Journal of Medical Robotics and Computer Assisted Surgery*, 1(3):42–48, 2005.

[75] Tian Xia, Clint Baird, George Jallo, Kathryn Hayes, Nobuyuki Nakajima, Nobuhiko Hata, and Peter Kazanzides. An integrated system for planning, navigation and

robotic assistance for skull base surgery. *The International Journal of Medical Robotics and Computer Assisted Surgery*, 4(4):321–330, 2008.

[76] Ch Nimsky, J Rachinger, H Iro, and R Fahlbusch. Adaptation of a hexapod-based robotic system for extended endoscope-assisted transsphenoidal skull base surgery. *Minimally Invasive Neurosurgery*, 47(01):41–46, 2004.

[77] KWG Eichhorn and F Bootz. Clinical requirements and possible applications of robot assisted endoscopy in skull base and sinus surgery. In *Intraoperative Imaging*, pages 237–240. Springer, 2011.

[78] Tipakorn Greigarn, Nate Lombard Poirot, Xinyang Xu, and M Cenk Çavuşoğlu. Jacobian-based task-space motion planning for MRI-actuated continuum robots. *Robotics and Automation Letters*, 4(1):145–152, 2019.

[79] Y Kim, SS Cheng, M Diakite, RP Gullapalli, JM Simard, and JP Desai. Toward the development of a flexible mesoscale MRI-compatible neurosurgical continuum robot. *IEEE Transactions on Robotics*, 33(6):1386–1397, 2017.

[80] Hyun-Soo Yoon, Se Min Oh, Jin Hyeok Jeong, Seung Hwan Lee, Kyung Tae, Kyoung-Chul Koh, and Byung-Ju Yi. Active bending endoscope robot system for navigation through sinus area. In *International Conference on Intelligent Robots and Systems*, pages 967–972. IEEE, 2011.

[81] Yi Sun and Hongliang Ren. Soft transnasal endoscopic robot for patient-administered nasopharynx inspection. *ASME Journal of Medical Devices*, 9(2): 020930, 2015.

[82] Andrea Bajo, Latif M Dharamsi, James L Netterville, C Gaelyn Garrett, and Nabil Simaan. Robotic-assisted micro-surgery of the throat: The trans-nasal approach. In *International Conference on Robotics and Automation*, pages 232–238. IEEE, 2013.

[83] Hyun-Soo Yoon, Jin Hyeok Jeong, and Byung-Ju Yi. Image-guided dual master–slave robotic system for maxillary sinus surgery. *IEEE Transactions on Robotics*, 34 (4):1098–1111, 2018.

[84] Philip J. Swaney, Arthur W. Mahoney, Bryan I. Hartley, Andria A. Remirez, Erik P. Lamers, Richard H. Feins, Ron Alterovitz, and Robert J. Webster III. Toward Transoral Peripheral Lung Access: Combining Continuum Robots and Steerable Needles. *Journal of Medical Robotics Research*, 2(1):1750001, 2017.

[85] Christos Bergeles, Andrew H Gosline, Nikolay V Vasilyev, Patrick J Codd, J Pedro, and Pierre E Dupont. Concentric tube robot design and optimization based on task and anatomical constraints. *IEEE Transactions on Robotics*, 31(1):67–84, 2015.

[86] Philip J Swaney, Hunter B Gilbert, Robert J Webster III, Paul T Russell III, and Kyle D Weaver. Endonasal Skull Base Tumor Removal Using Concentric Tube Continuum Robots: A Phantom Study. *Journal of Neurological Surgery Part B: Skull Base*, 76(2):145–149, 2015.

[87] Liao Wu, Shuang Song, Keyu Wu, Chwee Ming Lim, and Hongliang Ren. Development of a compact continuum tubular robotic system for nasopharyngeal biopsy. *Medical & biological engineering & computing*, 55(3):403–417, 2017.

[88] Ashley A Campbell, Seanna R Grob, and Michael K Yoon. Novel surgical approaches to the orbit. *Middle East African Journal of Ophthalmology*, 22(4):435, 2015.

[89] Aldo Stamm and João Flávio Nogueira. Orbital cavernous hemangioma: transnasal endoscopic management. *Otolaryngology-Head and Neck Surgery*, 141(6):794–795, 2009.

[90] Luca Muscatello, Veronica Seccia, Michele Caniglia, Stefano Sellari-Franceschini,

and Riccardo Lenzi. Transnasal endoscopic surgery for selected orbital cavernous hemangiomas: our preliminary experience. *Head & Neck*, 35(7):E218–E220, 2013.

[91] Nipun Chhabra, Arthur W Wu, Aaron Fay, and Ralph Metson. Endoscopic resection of orbital hemangiomas. In *International Forum of Allergy & Rhinology*, volume 4, pages 251–255, 2014.

[92] Tina D Tailor, Divakar Gupta, Roberta W Dalley, C Dirk Keene, and Yoshimi Anzai. Orbital neoplasms in adults: clinical, radiologic, and pathologic review. *Radiographics*, 33(6):1739–1758, 2013.

[93] Luigi Calandriello, Gabriela Grimaldi, Gianluigi Petrone, Mario Rigante, Sergio Petroni, Monica Riso, and Gustavo Savino. Cavernous venous malformation (cavernous hemangioma) of the orbit: Current concepts and a review of the literature. *Survey of Ophthalmology*, 62(4):393–403, 2017.

[94] Chi-Hsin Hsu and Wen-Ming Hsu. Cavernous hemangioma of the orbit: 42 patients. *Journal of Experimental & Clinical Medicine*, 3(6):278–282, 2011.

[95] Morgan Quigley, Ken Conley, Brian Gerkey, Josh Faust, Tully Foote, Jeremy Leibs, Rob Wheeler, and Andrew Y Ng. Ros: an open-source robot operating system. In *ICRA workshop on open source software*, number 3.2, page 5. Kobe, Japan, 2009.

[96] Jianzhong Shang, Christopher J Payne, James Clark, David P Noonan, Ka-Wai Kwok, Ara Darzi, and Guang-Zhong Yang. Design of a multitasking robotic platform with flexible arms and articulated head for minimally invasive surgery. In *International Conference on Intelligent Robots and Systems*, pages 1988–1993. IEEE, 2012.

[97] Nabil Simaan, Russell Taylor, and Paul Flint. High dexterity snake-like robotic slaves for minimally invasive telesurgery of the upper airway. In *International Con-*

ference on Medical Image Computing and Computer-Assisted Intervention, pages 17–24. Springer, 2004.

[98] A Bhandari, A Hemal, M Menon, et al. Instrumentation, sterilization, and preparation of robot. *Indian Journal of Urology*, 21(2):83, 2005.

[99] Fang-Yu Lin, Christos Bergeles, and Guang-Zhong Yang. Biometry-based concentric tubes robot for vitreoretinal surgery. In *International Conference on Engineering in Medicine and Biology Society*, pages 5280–5284. IEEE, 2015.

[100] Philip J Swaney, Ray Lathrop, Jessica Burgner, Kyle Weaver, Hunter B Gilbert, Robert J Webster, and David B Comber. System, method, and apparatus for configuration, design, and operation of an active cannula robot, August 13 2015. US Patent App. 14/177,864.

[101] Hunter B Gilbert, R. J. Hendrick, and R. J. Webster III. Elastic Stability of Concentric Tube Robots: A Stability Measure and Design Test. *IEEE Transactions on Robotics*, 32(1):20–35, 2016.

[102] Junhyoung Ha, Frank C Park, and Pierre E Dupont. Elastic stability of concentric tube robots subject to external loads. *Transactions on Biomedical Engineering*, 63 (6):1116–1128, 2016.

[103] Hao Su, Weijian Shang, Gregory Cole, Gang Li, Kevin Harrington, Alexander Camilo, Junichi Tokuda, Clare M Tempany, Nobuhiko Hata, and Gregory S Fischer. Piezoelectrically actuated robotic system for mri-guided prostate percutaneous therapy. *IEEE/ASME Transactions on Mechatronics*, 20(4):1920–1932, 2015.

[104] Jessica Burgner, Hunter B Gilbert, and Robert J Webster. On the computational design of concentric tube robots: Incorporating volume-based objectives. In *International Conference on Robotics and Automation*, pages 1193–1198. IEEE, 2013.

[105] Junhyoung Ha, Frank C Park, and Pierre E Dupont. Achieving elastic stability of concentric tube robots through optimization of tube precurvature. In *International Conference on Robotics and Automation*, pages 864–870. IEEE, 2014.

[106] Richard J Hendrick, Hunter B Gilbert, and Robert J Webster. Designing snap-free concentric tube robots: A local bifurcation approach. In *International Conference on Robotics and Automation*, pages 2256–2263. IEEE, 2015.

[107] Charles Wampler. Manipulator inverse kinematic solutions based on vector formulations and damped least-squares methods. *IEEE Transactions on Systems, Man and Cybernetics*, 16(1):93,101, 1986. ISSN 0018-9472.

[108] Tan Fung Chan and Rajiv V Dubey. A weighted least-norm solution based scheme for avoiding joint limits for redundant joint manipulators. *IEEE Transactions on Robotics and Automation*, 11(2):286–292, 1995.

[109] Richard J. Hendrick. *System Design and Elastic Stability Modeling of Transendoscopic Continuum Robots*. Ph.d. dissertation, Vanderbilt University, Nashville, TN, 2017.

[110] Patrick L. Anderson, Richard J. Hendrick, Margaret F. Rox, and Robert J. Webster III. Exceeding traditional curvature limits of concentric tube robots through redundancy resolution. *International Journal of Robotics Research (Accepted)*, 2019.

[111] Konrad Leibrandt, Christos Bergeles, and Guang-Zhong Yang. Implicit active constraints for concentric tube robots based on analysis of the safe and dexterous workspace. In *International Conference on Intelligent Robots and Systems*, pages 193–200. IEEE, 2017.

[112] Christos Bergeles and Pierre E Dupont. Planning stable paths for concentric tube robots. In *Inetrnational Conference on Intelligent Robots and Systems*, pages 3077–3082. IEEE, 2013.

[113] Hunter B. Gilbert. *Concentric Tube Robots: Design, Deployment, and Stability*. Ph.d. dissertation, Vanderbilt University, Nashville, TN, 2016.

[114] Andriy Fedorov, Reinhard Beichel, Jayashree Kalpathy-Cramer, Julien Finet, Jean-Christophe Fillion-Robin, Sonia Pujol, Christian Bauer, Dominique Jennings, Fiona Fennessy, Milan Sonka, et al. 3d slicer as an image computing platform for the quantitative imaging network. *Magnetic Resonance Imaging*, 30(9):1323–1341, 2012.

[115] Paolo Cignoni, Marco Callieri, Massimiliano Corsini, Matteo Dellepiane, Fabio Ganovelli, and Guido Ranzuglia. Meshlab: an open-source mesh processing tool. In *Eurographics Italian Chapter Conference*, pages 129–136, 2008.

[116] Inessa Bekerman, Paul Gottlieb, and Michael Vaiman. Variations in eyeball diameters of the healthy adults. *Journal of Ophthalmology*, 2014(2):5, 2014. ISSN 2090-004X.

[117] Trevor L Bruns, Katherine E Riojas, Dominick S Ropella, Matt S Cavilla, Andrew J Petruska, Michael H Freeman, Robert F Labadie, Jake J Abbott, and Robert J Webster III. Magnetically steered robotic insertion of cochlear-implant electrode arrays: System integration and first-in-cadaver results. *IEEE Robotics and Automation Letters*, 5(2):2240–2247, 2020.

[118] Rashid Yasin, Matthew Dedmon, Neal Dillon, and Nabil Simaan. Investigating variability in cochlear implant electrode array alignment and the potential of visualization guidance. *Int. J. Med. Robot.*, page e2009, 2019.

[119] Stephen J Rebscher, Alexander Hetherington, Ben Bonham, Peter Wardrop, David Whinney, and Patricia A Leake. Considerations for the design of future cochlear implant electrode arrays: Electrode array stiffness, size and depth of insertion. *J. Rehabil. Res. Dev.*, 45(5):731, 2008.

[120] Arunkumar N Badi, Thomas R Kertesz, Richard K Gurgel, Clough Shelton, and Richard A Normann. Development of a novel eighth-nerve intraneural auditory neuroprosthesis. *Laryngoscope*, 113(5):833–842, 2003.

[121] Adrian Dalbert, Alexander Huber, Naemi Baumann, Dorothe Veraguth, Christof Roosli, and Flurin Pfiffner. Hearing preservation after cochlear implantation may improve long-term word perception in the electric-only condition. *Otol. Neurotol.*, 37(9):1314–1319, 2016.

[122] Pavel Mistrík, Claude Jolly, Daniel Sieber, and Ingeborg Hochmair. Challenging aspects of contemporary cochlear implant electrode array design. *World Journal of Otorhinolaryngology-Head and Neck Surgery*, 2018.

[123] Peter Wardrop, David Whinney, Stephen J Rebscher, J Thomas Roland Jr, William Luxford, and Patricia A Leake. A temporal bone study of insertion trauma and intracochlear position of cochlear implant electrodes. i: Comparison of nucleus banded and nucleus contour™ electrodes. *Hearing research*, 203(1-2):54–67, 2005.

[124] Mehmet A Somdas, Peter MMC Li, Darren M Whiten, Donald K Eddington, and Joseph B Nadol Jr. Quantitative evaluation of new bone and fibrous tissue in the cochlea following cochlear implantation in the human. *Audiology and Neurotology*, 12(5):277–284, 2007.

[125] Kyeung A Ryu, Ah-Ra Lyu, Heesung Park, Jin Woong Choi, Gang Min Hur, and Yong-Ho Park. Intracochlear bleeding enhances cochlear fibrosis and ossification: an animal study. *PloS one*, 10(8):e0136617, 2015.

[126] Omid Majdani, Daniel Schurzig, Andreas Hussong, Thomas Rau, Justin Wittkopf, Thomas Lenarz, and Robert F Labadie. Force measurement of insertion of cochlear implant electrode arrays in vitro: comparison of surgeon to automated insertion tool. *Acta oto-laryngologica*, 130(1):31–36, 2010.

[127] Marco Caversaccio, Kate Gavaghan, Wilhelm Wimmer, Tom Williamson, Juan Anso, Georgios Mantokoudis, Nicolas Gerber, Christoph Rathgeb, Arne Feldmann, Franca Wagner, et al. Robotic cochlear implantation: surgical procedure and first clinical experience. *Acta oto-laryngologica*, 137(4):447–454, 2017.

[128] Louis B Kratchman, Daniel Schurzig, Theodore R McRackan, Ramya Balachandran, Jack H Noble, Robert J Webster III, and Robert F Labadie. A manually operated, advance off-stylet insertion tool for minimally invasive cochlear implantation surgery. *IEEE Trans. Biomed. Eng.*, 59(10):2792–2800, 2012.

[129] Mathieu Miroir, Yann Nguyen, Guillaume Kazmitcheff, Evelyne Ferrary, Olivier Sterkers, and Alexis Bozorg Grayeli. Friction force measurement during cochlear implant insertion: application to a force-controlled insertion tool design. *Otol. Neurotol.*, 33(6):1092–1100, 2012.

[130] Paul Wilkening, Wade Chien, Berk Gonenc, John Niparko, Jin U Kang, Iulian Iordachita, and Russell H Taylor. Evaluation of virtual fixtures for robot-assisted cochlear implant insertion. In *5th IEEE RAS/EMBS International Conference on Biomedical Robotics and Biomechatronics*, pages 332–338. IEEE, 2014.

[131] Brendan P O'Connell, Jacob B Hunter, David S Haynes, Jourdan T Holder, Matt M Dedmon, Jack H Noble, Benoit M Dawant, and George B Wanna. Insertion depth impacts speech perception and hearing preservation for lateral wall electrodes. *Laryngoscope*, 127(10):2352–2357, 2017.

[132] Lisandro Leon, Matt S Cavilla, Michael B Doran, Frank M Warren, and Jake J Abbott. Scala-tympani phantom with cochleostomy and round-window openings for cochlear-implant insertion experiments. *J. Med. Devices*, 8(4):041010, 2014.

[133] Louis B Kratchman, Trevor L Bruns, Jake J Abbott, and Robert J Webster III. Guid-

ing elastic rods with a robot-manipulated magnet for medical applications. *IEEE Trans. Robot.*, 33(1):227–233, 2017.

[134] Lisandro Leon, Frank M Warren, and Jake J Abbott. Optimizing the magnetic dipole-field source for magnetically guided cochlear-implant electrode-array insertions. *J. Med. Robot. Res.*, 3(1):1850004, 2018.

[135] Trevor L Bruns and Robert J Webster III. An image guidance system for positioning robotic cochlear implant insertion tools. In *Proc. SPIE Medical Imaging*, volume 10135, pages 199–204, 2017.

[136] Andrew J Petruska and Jake J Abbott. Omnimagnet: An omnidirectional electromagnet for controlled dipole-field generation. *IEEE Trans. Magn.*, 50(7):1–10, 2014.

[137] Tamas Ungi, Andras Lasso, and Gabor Fichtinger. Open-source platforms for navigated image-guided interventions. *Medical Image Analysis*, 100(33):181–186, 2016.

[138] Levin Sliker, Gastone Ciuti, Mark Rentschler, and Arianna Menciassi. Magnetically driven medical devices: a review. *Expert review of medical devices*, 12(6):737–752, 2015.

[139] J. J. Abbott, E. Diller, and A. J. Petruska. Magnetic methods in robotics. *Annu. Rev. Cont. Robot. Autom.*, 3:2.1–2.34, 2020.

[140] V Hartwig, G Giovannetti, N Vanello, M Lombardi, L Landini, and S Simi. Biological effects and safety in magnetic resonance imaging: A review. *Int. J. Environ. Res. Public Health*, 6(6):1778–1798, 2009.

[141] International Commission on Non-Ionizing Radiation Protection. Guidelines on limits of exposure to static magnetic fields. *Health Phys.*, 96(4):504–514, 2009.

[142] D. J. Schaefer, J. D. Bourland, and J. A. Nyenhuis. Review of patient safety in time-varying gradient fields. *J. Magn. Reson. Imaging*, 12(1):12–20, 2000.

[143] Anandhan Dhanasingh and Claude Jolly. An overview of cochlear implant electrode array designs. *Hearing Research*, 356:93–103, 2017.

[144] Jack H Noble, Robert F Labadie, Omid Majdani, and Benoit M Dawant. Automatic segmentation of intracochlear anatomy in conventional CT. *IEEE Trans. Biomed. Eng.*, 58(9):2625–2632, 2011.

[145] Jack H Noble, Omid Majdani, Robert F Labadie, Benoit Dawant, and J Michael Fitzpatrick. Automatic determination of optimal linear drilling trajectories for cochlear access accounting for drill-positioning error. *Int. J. Med. Robot.*, 6(3):281–290, 2010.

[146] A. J. Petruska, J. Edelmann, and B. J. Nelson. Model-based calibration for magnetic manipulation. *IEEE Trans. Magn.*, 53(7):4900206, Jan 2017. doi: 10.1109/TMAG.2017.2653080.

[147] René H Gifford, Jon K Shallop, and Anna Mary Peterson. Speech recognition materials and ceiling effects: Considerations for cochlear implant programs. *Audiology and Neurotology*, 13(3):193–205, 2008.

[148] John C Middlebrooks and Russell L Snyder. Auditory prosthesis with a penetrating nerve array. *Journal for the Association for Research in Otolaryngology*, 8(2):258–279, 2007.

[149] Joseph P Roche and Marlan R Hansen. On the horizon: cochlear implant technology. *Otolaryngologic Clinics of North America*, 48(6):1097–1116, 2015.

[150] Charles G Wright and Peter S Roland. *Cochlear Anatomy Via Microdissection with Clinical Implications: An Atlas*. Springer, 2018.

[151] John Edward Brough Randles. Kinetics of rapid electrode reactions. *Discussions of the faraday society*, 1:11–19, 1947.

[152] Robert K Shepherd. Chronic electrical stimulation of the auditory nerve using non-charge-balanced stimuli. *Acta oto-laryngologica*, 119(6):674–684, 1999.

[153] James R Clark, Frank M Warren, and Jake J Abbott. A scalable model for human scala-tympani phantoms. *J. Med. Devices*, 5(1):014501, 2011.